Registration and Deformable Model-Based Neck Muscles Segmentation and 3D Reconstruction

Author:
Suman, Abdulla Al

Publication Date:
2017

DOI:
https://doi.org/10.26190/unsworks/3293

Registration and Deformable Model-Based Neck Muscles Segmentation and 3D Reconstruction

Abdulla Al Suman

A thesis submitted in fulfilment of the requirements

for the degree of

Masters by Research

School of Engineering and Information Technology

The University of New South Wales

Australia

August 2016

Copyright Statement

Abdulla Al Suman

UNSW, Australia

Authenticity Statement

'I certify that the Library deposit digital copy is a direct equivalent of the final officially approved version of my thesis. No emendation of content has occurred and if there are any minor variations in formatting, they are the result of the conversion to digital format.'

Abdulla Al Suman

UNSW, Australia

Originality Statement

'I hereby declare that this submission is my own work and to the best of my knowledge it contains no materials previously published or written by another person, or substantial proportions of material which have been accepted for the award of any other degree or diploma at UNSW or any other educational institution, except where due acknowledgement is made in the thesis. Any contribution made to the research by others, with whom I have worked at UNSW or elsewhere, is explicitly acknowledged in the thesis. I also declare that the intellectual content of this thesis is the product of my own work, except to the extent that assistance from others in the project's design and conception or in style, presentation and linguistic expression is acknowledged.'

Abdulla Al Suman
UNSW, Australia

Dedicated to my parents, My wife- Mst. Momota Yeasmin and my son-

Mohammad Shareek Afraz ...

Acknowledgments

I could not have completed this dissertation without the bountiful Sympathy and Blessings from Almighty Allah, the most Gracious and Benevolent in the universe.

I would like to express my cordial thanks and profound respect to my supervisor, Associate Professor Dr. Mark R. Pickering, for his excellent technical guidance, support, ideas, encouragement, patience and insightful discussions throughout my research study. In spite of his busy timetable, he always managed to schedule weekly meetings and others when needed. Again, I thank him for his uncomplaining polishing and proofreading of all my paper work. I am also extremely grateful to my co-supervisor, Professor Dr. John Fredrick Arnold, for his support and encouragement during my candidature. It would not have been possible to complete this work without their sustained assistance.

I am very pleased to thank Denise Russell for her worthy proofreading and suggestions on this thesis, and Alexandra Louise Webb, Diana M. Perriman and Dr John Au for providing me with clinical data and atlases.

I would like to express my sincere gratitude to Dr. Md. Jahangir Alam for his direction and support which have been invaluable on both personal and academic levels. Also, I wish to extend my warmest thanks and appreciation to my friends and colleagues, Dr. Md. Asikuzzaman, Dr. Habibullah, Atiqul Islam, Dr. Muhammad Shahin Uddin, Dr. Mst. Nargis Aktar, Dr. Sanjoy Kumar Paul, Dr. Mohammad Omar Khyam, Md. Forhad Zaman and Md. Abdul Kader for their encouragement and inspiration.

I also greatly appreciate the financial support and scope necessary to carry out my research work provided by The University of New South Wales (UNSW), and all UNSW staff members for their cordial assistance throughout my research journey.

Finally, I am deeply grateful to my parents for all they have given me and my wife, MSt Momota Yeasmin, my son, Mohammad Shareek Afraz, brother, sister, parents-in-law, grandparent and other close relatives for their constant love, encouragement, prayers and guidance.

Abstract

Whiplash is a very common ailment encountered in clinical practice that is usually a result of vehicle accidents but also domestic activities and sports injuries. It is normally caused when neck organs (specifically muscles) are impaired. Whiplash-associated disorders include acute headaches, neck pain, stiffness, arm dislocation, abnormal sensations, and auditory and optic problems, the persistence of which may be chronic or acute. Insurance companies compensate almost fifty percent of claims lodged due to whiplash injury through compulsory third party motor insurance. The morphological structures of neck muscles undergo hypertrophy or atrophy following damage caused to them by accidents. Before any medical treatment is applied, any such change needs to be known which requires 3D visualization of the neck muscles through a proper segmentation of them because the neck contains many other sensitive organs, such as nerves, blood vessels, the spinal cord and trachea.

The segmentation of neck muscles in medical images is a more challenging task than those of other muscles and organs due to their similar densities and compactness, low resolutions and contrast in medical images, anatomical variabilities among individuals, noise, inhomogeneity of medical images and false boundaries created by intra-muscular fat. Traditional segmentation algorithms, such as those used in thresholding and clustering-based methods, are not applicable in this project and also not suitable for medical images. Although there are some techniques available in clinical research for segmenting muscles, such as thigh, tongue, leg, hip and pectoral ones, to the best of author's knowledge, there are no methods available for segmenting neck muscles due to the challenges described above.

In the first part of this dissertation, an atlas-based method for segmenting MR images, which uses linear and non-linear registration frameworks, is proposed, with output from the registration process further refined by a novel parametric deformable model. The proposed method is tested on real clinical data of both healthy and non-healthy individuals. During the last few decades, registration- and deformable model-based segmentation methods have been very popular for medical image segmentation due to their incorporation of prior information. While registration-based segmentation techniques can preserve topologies of objects in an image, accuracy of atlas-based segmentation depends mainly on an effective registration process. In this study, the registration framework is designed in a novel way in which images are initially registered by a distinct 3D affine transformation and then aligned by a local elastic geometrical transformation based on discrete cosines and registered firstly slice-wise and then block-wise. The numbers of motion parameters are changed in three different steps per frame. This proposed registration framework can handle anatomical variabilities and pathologies by confining its parameters in local regions. Also, as warping of the framework relies on number of motion parameters, similarities between two images, gradients of floating image and coordinate mesh grid values, it can easily manage pathological and anatomical variabilities using a hierarchical parameter scheme.

The labels transferred from atlas can be improved by deformable model-based segmentation. Although geometric deformable models have been widely used in many biomedical applications over recent years, they cannot work in the context of neck muscles segmentation due to noise, background clutter and similar objects touching each other. Another important drawback of geometric deformable models is that they are many times slower than parametric deformable ones. Therefore, the segmentation results produced by the registration process are ameliorated using a multiple-object parametric deformable model which is discussed in detail in the second part of this thesis. This algorithm uses a novel Gaussian potential energy distribution which can adapt to topological changes and does not require re-parameterization. Also, it incorporates a new overlap removal technique which ensures that there are no overlaps or gaps inside an object. Furthermore, stopping criteria of vertices are designed so that difference between boundaries of the deformable model and actual object is minimal.

The multiple-object parametric deformable model is also applied in a template contours propagation-based segmentation technique, as discussed in the third part of this dissertation. This method is semi-automatic, whereby a manual delineation of middle image in a MRI data set is required. It can handle anatomical variabilities more easily than atlas-based segmentation because it can segment any individual's data irrespective of his/her age, weight and height with low computational complexity and it does not depend on other data as it operates semi-automatically. In it, initial model contour resides close to the object's boundary, with degree of closeness dependent on slice thicknesses and gaps between the slices.

Contents

List of Figures

List of Tables

List of Abbreviations

Abbreviations	Description
2D	2-dimensional
3D	3-dimensional
ASM	active shape model
CMI	Conditional Mutual Information
CSA	Cross Sectional Area
CGPED	Conditional gaussian potential energy distribution
CP	Contour propagation
DSC	Dice Similarity Coefficient
eSSD	Entropy sum-of-Squared Difference
GUI	Graphical User Interface
GDM	Geometric deformable model
MRI	Magnetic Resonance Imaging
MOPD	Multiple Object Parametric Deformable
MI	Mutual Information
NMI	Normalized Mutual Information
PVI	Partial Volume Interpolation
PCA	Principal component analysis
PDM	Parametric deformable model
ROI	Region of Interest
SCV	Sum of Conditional Variance
WADs	Whiplash Associated Disorders

Chapter 1

Introduction

The term 'whiplash' covers a range of injuries to the neck most commonly caused by sudden acceleration and deceleration associated with rear-end motor vehicle accidents. It not only affects motor insurance companies but also has some socioeconomic impacts on governments or other industries which are required to provide payments to sufferers, such as for long-term sick leave, early disability and disability support pensions. More than 430,000 people claimed compensation for whiplash injuries in the United Kingdom in 2007 [11]. Another study by the state insurance regulatory authority in NSW, Australia, revealed that, since 2007, 46 percent of compulsory third-party health insurance claims in that state were for whiplash-associated disorders (WADs) [12]. Therefore, the diagnosis and treatment of WADs which cause the neck muscles to atrophy or hypertrophy and change their morphologies [13, 14], are important issues in clinical practice.

Although segmenting neck muscles in medical images would help physicians to understand their sizes and shapes, none of the current segmentation algorithms can achieve this due to challenges associated with anatomical variability, compactness, low resolution and contrast, intra-muscular fat and background clutter of these muscles in medical images. Therefore, this thesis focusses on designing and implementing algorithms for segmenting neck muscles from MR images which overcome these challenges. The remainder of this chapter is organized as follows: Section 1.1 provides the reasons for neck muscles segmentation; 1.2 application of segmentation; 1.3 challenges and motivation of the work; 1.4 contributions of this study; 1.5 thesis outline; and 1.6 publication and award list.

1.1 Necessity for Neck Muscles Segmentation

Whiplash is caused mainly by rear-end motor collisions but may occur as a result of any accident involving similar motions, such as domestic activities, sports (skiing, headbanging, bungee jumping, etc.), riding at an amusement park and other modes of transportation [15]. Symptoms of WADs include neck pain, headaches, stiffness, sensory disturbance to the legs and arms, aching in the back and shoulder, and auditory and visual problems [16]. A patient suffering from WADs either recovers within two to three months or experiences symptoms for a long time, perhaps chronically. The socioeconomic implications of WADs are notable because, each year, approximately one million people suffer whiplash injuries due to vehicle accidents [17]. Freeman *et al.* [18] estimated that approximately 6.2 percent of the US population have a whiplash syndrome. In their study, Foreman and Croft [19] found that the indirect costs to industry based on the degrees of severity of WADs are $\$66,626$ per year, with the total cost per year increasing by 317 percent from 1998 to $40.5 billion in 2008. They also found that, for sufferers, the symptoms persist in only 1 in 5 after 1 year, 11.5 percent return to work after 1 year and 35.4 percent regain a similar performance to that prior to receiving a WAD after 20 years. Bylund and Björnstig [20] analysed the long-term consequences of whiplash injuries in terms of the need for long-term sick leave, medical care and early disability pensions, and loss of income tax in an urban area in Sweden which led to increasing costs for industries and the communities. Therefore, insurance companies, employers, governments, health professionals and communities need to think about obtaining remedies for WADs as soon as possible so that these costs can be reduced.

For patients with WADs, the morphologies of their neck muscles are disturbed due to fat infiltrating into the muscles [14] while their cervical muscles also experience pseudo-hypertrophy and atrophy [13]. Elliott *et al.* [13] obtained larger relative cross-sectional areas for multifidus, semispinalis capitis, splenius capitis, deep cervical flexors and sternocleidomastoid cervical muscles, and smaller ones for semispinalis cervicus and semispinalis capitis muscles from a WADs group than a healthy control group of individuals. Bismil and Bismil [21] stated in their study that the trapezius muscle may be damaged during a whiplash event through muscle contraction. Therefore, to apply proper medical treatments for WADs, physicians need to know the amount of disturbance and its exact position in the cervical region which contains many other sensitive organs, such as blood vessels, nerves, the trachea and spinal cord. To analyse their shapes and sizes, neck muscles need to be segmented from a volume image. MRI and CT provide volumetric images of an object in terms of a sequence of 2D images which need to be segmented to form a 3D view in order to analyse the shapes, sizes and 3D perspectives of the muscles by rotating, zooming and panning. Generally, in clinical practice, the task of segmentation is performed manually which is tedious and time-consuming, suffers from intra- and inter-operator variabilities and is not suitable for large-scale data analyses [22]. Therefore, to reduce the labor required and enhance analysis efficiency, an automatic repetitive segmentation algorithm is essential.

1.2 Application of Segmentation

Image segmentation is regarded as one of the fundamental steps in many important applications, such as motion tracking, scene reconstruction, aerial imaging, content-based image retrieval [5], clinical diagnosis and pattern recognition. Segmentation assists some core clinical tasks, such as quantification, locating pathologies, undertaking computer-integrated surgery, measuring tissue volumes [23], inspecting and visualizing anatomical structures, surgical planning and simulation, radiotherapy planning, intra-operative navigation and tracking the progress of a disease. In surgery and radiotherapy, precise interventions are required to reduce the risk of collateral damage of healthy tissues and organs. In particular, 3D visualizations of the detailed shapes and orientations of structures can assist a surgeon to apply a proper approach for the targeted structure. For example, a radiologist should be vigilant about healthy tissues while applying a necrotic dose of radiation on a tumor.

1.3 Challenges and Motivation for Neck Muscles Segmentation

Medical image segmentation is generally a challenging task due to the anatomical variability, low resolution and contrast, noise, inhomogeneity and organ diffusion in an image. Therefore, traditional segmentation algorithms, such as thresholding and clustering, which have some shortcomings, as discussed in detail in Chapter 2, are more useful as steps in conjunction with other techniques rather than as a complete segmentation processes. Segmenting neck muscles in medical images is very difficult due to the compactness of the muscles, *intra*-muscular fat, background clutter with similar intensity, sliding due to respiratory motions and similar composition of these muscles. These scenarios are shown in Figure 1.1. The size of neck muscles varies according to patient's weight, height, gender and age shown in Figure 1.2, which makes difficult to choose an atlas from an atlas

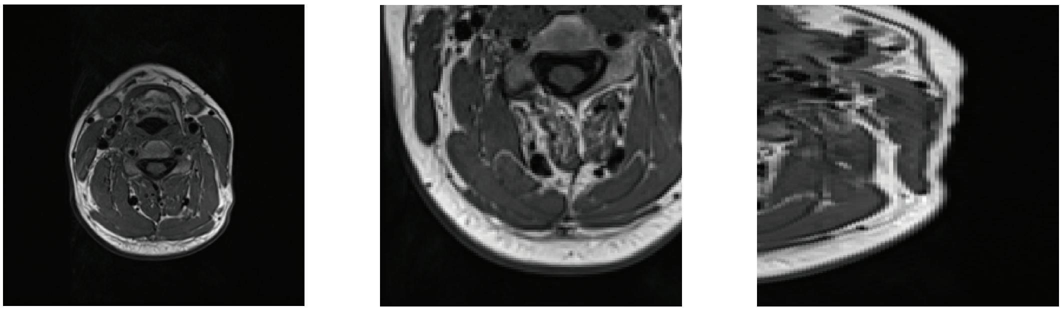

(a) (b) (c)

Figure 1.1: Challenges of neck muscle segmentation: (a) low-resolution contrast and high compactness; (b) intra-fat; and (c) background clutter.

database for a specific patient's image in registration-based segmentation method. In addition, the neck muscles' anatomy is very complicated due to a large number of small and big muscles of similar composition sharing a compact space. These anatomical complexities as well as some imaging artefacts such as low contrast, partial volume effect, inhomogeneity and noise make the muscles boundary obscure shown in Figure 1.1 (a). Moreover, sometimes *intra*-muscular fat falls an expert clinician in confounding for considering as *inter*-muscular fat, which is shown in Figure 1.1 (b). Also, other organs close to muscles generate similar intensities in images which make a segmentation algorithm difficult to segment the muscles shown in Figure 1.1 (b). Existing medical image segmentation algorithms are not directly applicable to segment neck muscles, which are needed to be refined to be better handle the challenges found in neck muscles segmentation.

None of the existing segmentation algorithms is general as each is designed for a unique application. In recent decades, registration and deformable model-based segmentation techniques have been widely used in clinical research to segment various medical images for different applications. Although registration-based methods are successful for brain organ segmentation, they are still not adopted in clinical practice due to their lack of a robust registration algorithm. Also, brain structures are more stable than neck ones due to their having no sliding effect for

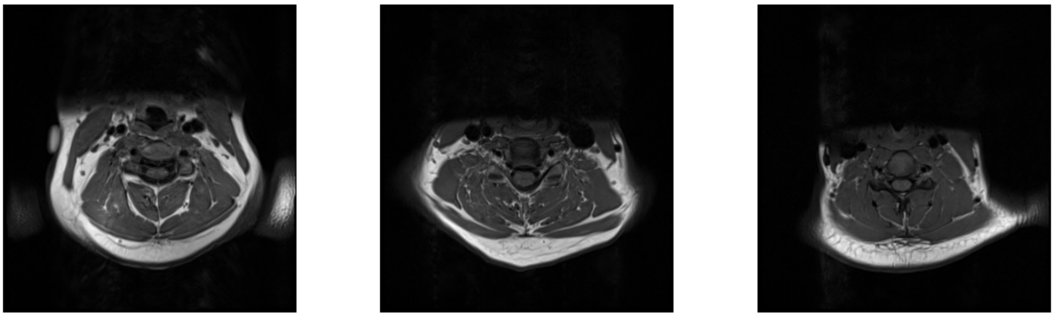

(a) (b) (c)

Figure 1.2: Images from same neck level illustrating anatomical variability (a) Male patient with weight 121 kg, height 1.78 m and age 30 years; (b) Male patient with weight 105 kg, height 1.78 m and age 30 years; and (c) Female patient with weight 74 kg, height 1.58 m and age 22 years.

respiratory motions which causes organ diffusion in images for which a registration algorithm could achieve good alignment. Furthermore, researchers have recently been trying to increase the accuracy of segmentation using multi-atlas techniques but not a robust registration which is the core step in the technique. A multi-atlas technique using an existing registration method can increase accuracy to some degree but, if a robust registration algorithm is designed and used in a multi-atlas framework, much better accuracy could be achieved. Therefore, in this study, a robust generalized deformable registration framework is designed and applied for neck muscles segmentation which, to the best of the author's knowledge, is the first work on neck muscles that can handle anatomical variabilities and the sliding effect. Although, in recent years, rigid and anatomical registrations using statistical shape models and region growing-based methods have been proposed for thigh and calf muscles segmentation [22, 24], they are not fully registration-based. Details of the literature on registration-based methods are provided in Chapter 2.

The results produced by the registration process are further enhanced through a deformable model-based technique. Currently, geometric deformable models

(GDMs) are the most popular although they can correctly handle topology changes for only two or multi-phase images with good contrast but not for multi-phase compact ones with similar intensities. They also have other limitations, such as providing spurious connected components in noisy images and images with compact organs and cannot completely separate compact objects with similar intensities. These shortcomings mean that GDMs are incapable of being applied for neck muscles segmentations because similar conditions exist in these muscles due to their compactness, sliding effect and background clutter. Therefore, in this study, a new parametric deformable model (PDM)-based framework using a novel Gaussian potential energy distribution, which does not experience any of the overlapping and gap problems seen in classical PDMs, is proposed. This PDM mitigates the well-known problems of re-parameterization and topology changes of a traditional PDM through its novel energy distribution which is explained in detail in Chapter 4.

1.4 Contributions of This Research

The major purpose of this research is to design an automatic neck muscles segmentation algorithm with low complexity and good accuracy which can handle anatomical variabilities and assist physicians to analyse the sizes and shapes of neck muscles for diagnosing WADs. Its key contributions are summarized as follows.

- In the first part of this research, a novel registration framework using affine and elastic motion models is developed. The affine registration introduces a new technique of three-level Gaussian filtering of the reference and floating image volumes before registration to improve the optimization process. The elastic registration uses discrete cosines as basis functions and is performed slice-wise in three different steps with different numbers of motion parameters and another block-wise step. Then, the contours obtained from this framework are refined using a multiple-object PDM and reconstructed for 3D visualization using a Matlab graphical user interface. This registration framework can handle anatomical variabilities and pathologies by confining its parameters in local regions, with the proposed method achieving good segmentation accuracy for real clinical data, as validated by three medical experts.

- In the second part of this study, a new multiple-object PDM using a novel conditional Gaussian potential energy distribution generated based on the major axis of an object is developed. Also, new overlap removal and sampling techniques that provide overlap-free segmentation results are incorporated. This scheme overcomes the problems of traditional PDMs through its energy distribution while GDMs cannot work in the context of neck muscles segmentation due to noise, background clutter and similar objects touching each other.

- In the last part of this thesis, a contour propagation-based segmentation process using a high inter-slice gap and thickness, which is dependent mainly on the new multiple-object PDM, is introduced. It is semi-automatic, requiring manual interaction only on the middle slice of a MRI volume. It can handle anatomical variabilities more easily because it can segment any data, irrespective of an individuals age, height and weight, with low computational complexity and does not depend on other data.

1.5 Organization of Thesis

The remainder of this dissertation is organized as follows.

Chapter 2 discusses the relevant literature on medical image segmentation methods, and their operating principles and pros and cons. Finally, guidelines for neck muscles segmentation based on this information are presented.

Chapter 3 presents the design of the registration framework and segmentation process using the framework for neck muscles. It also provides a short description of the PDM for improving the registration results for clinical MRI data.

Chapter 4 provides details of the design of the multiple-object PDM for segmentation and experimental results obtained from it for neck muscles. Also, an overlap removal technique and resampling are presented.

Chapter 5 introduces a contour propagation-based segmentation method dependent mainly on the multiple-object PDM which has good potential for medical image segmentation.

Chapter 6 provides a summary of this dissertation and future directions for improving this research.

1.6 List of Publications and Award

The results obtained from this study have been partially published and some are in the process of publication in the journal articles and conference papers listed below.

Journal Articles

- **Abdulla Al Suman**, Mst. Nargis Aktar, Md. Asikuzzaman, Alexandra Louise Webb, Diana M. Perriman and Mark Richard Pickering,"Segmentation and Reconstruction of Cervical Muscles using Knowledge-based Grouping Adaptation and New Step-wise Registration with Discrete Cosines," *Computer Methods in Biomechanics and Biomedical Engineering: Imaging & visualization.* Accepted.
- **Abdulla Al Suman**, Mst. Nargis Aktar, Md. Asikuzzaman, Alexandra Louise Webb, Diana M. Perriman and Mark Richard Pickering,"A Novel Potential Energy function based Multiple Object Deformable Model with Coupling Adaptation and Overlap Removal Technique in Neck Muscles Segmentation," *Computer Methods and Programs in Biomedicine.* Submitted.

Conference Papers

- **Abdulla Al Suman**, Mst. Nargis Aktar, Md. Asikuzzaman, Alexandra Louise Webb, Diana M. Perriman and Mark Richard Pickering, "Atlas-Based Segmentation of Neck Muscles from MRI for The Characterisation of Whiplash Associated Disorder," *8th International Conference on Digital Image Processing*,20–23 May. 2016, Chengdu, China.
- **Abdulla Al Suman**,Alexandra Louise Webb, Diana M. Perriman and Mark Richard Pickering, "Template Contour Propagation based Neck Muscles Segmentation," *IEEE International Symposium on Biomedical Imaging*,18-21 April, 2017, Melbourne, Australia. Submitted.

Award

- **Selected as one of the most excellent papers**, "Atlas-Based Segmentation of Neck Muscles from MRI for The Characterisation of Whiplash Associated Disorder," *8th International Conference on Digital Image Processing*, 20–23 May. 2016, Chengdu, China.

Chapter 2

Related Works on Medical Image Segmentation

Medical image segmentation plays a significant role in many practical applications related to clinical diagnosis. A large number of segmentation processes can be found in the literature but not all of them can be applied in medical image segmentation. This chapter provides a comprehensive investigation of methods for medical image segmentation classified based on their main operating principles which, together with their application areas, and pros and cons of each class are discussed in detail. Finally, the motivation for designing our neck muscles segmentation algorithm is presented. The remainder of this chapter is organized as follows: Section 2.1 presents a brief introduction about segmentation algorithms; 2.2 different type of segmentation algorithms in details; 2.3 a general discussion and guidelines for neck muscles segmentation.

2.1 Introduction

In many computer vision applications, such as motion tracking, scene reconstruction, image retrieval, and aerial and medical imaging, the key stage is image segmentation. Therefore, a large number of automatic image segmentation algorithms has been proposed in image processing research but some are not applicable for medical image segmentation, in particular, edge detection-based segmentation, because, in medical images, organs or structures often touch each other due to their partial volume effects (PVEs) and complex anatomies. Medical image segmentation is used in the localization of pathologies, computer-aided surgery, volume quantification, monitoring the post-operative progression of a disease and therapy planning. Although modern imaging modalities provide high-resolution images, it is still very difficult to segment medical images due to their noise, poor image contrast, PVEs, intensity inhomogeneities, different structures with similar intensities and artefacts.

Traditionally, a medical image has been delineated manually by an anatomical expert using prior anatomical knowledge to segment anatomical organs. However, manual segmentation is slow, painful, not reproducible, error prone, expensive and subject to intra- and inter-operator variabilities. Therefore, it is unsuitable for an application in which many images need to be segmented in a short time. Therefore, automatic segmentation is highly desirable in the medical science arena for providing fast, reproducible segmentation at a low cost with large scalability. Since a clinician uses prior anatomical knowledge for manual segmentation, automatic segmentation methods should incorporate this knowledge in their implementation processes to achieve similar accuracy. The procedures for incorporating prior knowledge, which are different in different types of automatic segmentation methods, can include shape information, region intensity and edge terms; for example, in atlas-based automatic segmentation methods, prior shape information is obtained through a registration process. Prior information used in conjunction with traditional automatic segmentation techniques works as an automatic medical image segmentation algorithm.

Automatic medical image segmentation is sometimes defined in terms of imaging modalities according to which the imaging features of an organ vary; in particular, a MR image provides finer details of soft tissues than other imaging modalities. Although some methods combine multiple techniques in a single algorithm, which makes it difficult to classify them as belonging to a single genre, they are categorized based on their main ideas.

The MR modality is used extensively in clinical practice for the visualization of soft tissues due to its high spatial resolution and good contrast which also allows multi-views (axial, coronal and sagittal) of a patient as well as multi-weighted (T1 and T2) images by changing the echo and repetition times, with its imaging contrast dependent on the density of the object considered. However, as many neck muscles with similar tissue densities occupy a compact space and almost touch each other, their MR images contain PVEs and similar intensities. Therefore, the task of neck muscles segmentation is very challenging and, to the best of our knowledge, no method for it has been developed. In this chapter, rather than proposing a new algorithm for neck muscles segmentation, we conduct a detailed study of medical image segmentation methods and a feasibility analysis regarding applying any of them for neck muscles segmentation.

2.2 Segmentation Classification

Some classes of medical image segmentation algorithms are presented in the following subsections, with their main ideas, pros and cons and generic applications discussed. While each method has its own requirements and background, this study covers only main algorithms not all the approaches in the literature.

2.2.1 Threshold-based Algorithms

One of the easiest segmentation methods is a threshold-based one for volumes and scalar images [25, 26]. In it, objects are segmented based on their intensity thresholds or any other threshold derived from the original image, such as the gradient magnitude. Each pixel (or voxel) in an image (or volume image) is compared with the thresholds to assign it to a class. These algorithms are normally applicable for objects in images with distinguishable features on which the number of thresholds depends. These thresholds are selected either manually, which requires prior knowledge of the image and objects, or automatically which exploits the image's information [27]; for instance, Otsu [28] used an image histogram for threshold selection. However, threshold-based algorithms suffer from the effects of noise, thresholds and intensity inhomogeneity on the segmented output, and their neglect of the spatial intensity correlation [26].

The performance for segmenting a corrupted image can be enhanced using adaptive thresholding techniques in which local imaging properties are used to define the thresholds. Kittler *et al.* [29] used gradient magnitude statistics for adaptive threshold selection and Kom *et al.* [30] adaptive thresholding for the detection of masses from mammograms. Some other medical image segmentation methods also applied adaptive thresholding [31–34].

Thresholding algorithms are further classified based on the image information used for their selection, such as region-based, edge-based and hybrid. However, although edge detection-based algorithms are used as a pre-processing step in many other techniques, they are not considered for medical image segmentation. The other two approaches are described below.

2.2.1.1 Region-based Algorithms

Algorithms based on regions use some criteria (the intensity distribution, connectivity, edges) to extract a region of interest (ROI) from a 2D or volume image in which these criteria are normally homogeneous. Region-based algorithms are further classified as seeded and unseeded region-growing.

In seeded region-growing algorithms, an initial seed point is required to extract a ROI which is gradually enlarged by merging adjacent pixels, the intensity values of which fall within specified thresholds until all the surrounding pixels' intensities are outside these thresholds [35–39]. Region-growing algorithms are sometimes used in conjunction with another technique; for instance, Nyúl *et al.* [40] segmented the spinal canal and cord from 3D CT images using a region-growing technique with a slice-to-slice process. Also, Rai and Nair [41] considered gradient-seeded region-growing for CT angiographic images. The dependence of the initial seed can be waived by incorporating prior information in these algorithms [42]; for example, Udupa and Samarasekera [43] applied fuzzy sets theory in their algorithms. These algorithms are sensitive to the initial seed points, noise and leakage due to PVEs.

An unseeded region-growing algorithm does not require seed points as it splits or merges regions based on predefined criteria [44] but is computationally expensive due to the pyramidal grid structure it requires.

2.2.1.2 Hybrid Algorithms

Information brought from various image cues and other techniques are incorporated in hybrid algorithms, such as watershed-based segmentation methods [45–49] in which objects are considered to be enclosed by watershed lines identified as the pixels with a local maximum gradient magnitude. Although these algorithms may yield good output due to their combination of miscellaneous information, they still suffer from an over-segmentation problem if the relevant image contains noise. Other techniques combined with watershed methods are marker imposition [45], the k-means clustering algorithm for handling over-segmentation [47], morphological operators [48] and probabilistic atlases [49].

2.2.2 Clustering-based Algorithms

In clustering-based algorithms, which are very popular in medical image segmentation, objects are considered separate classes or clusters with distinct features. The most important task of these algorithms is to identify the quantifiable distinct features of structures, which is practically very difficult for medical images, and they are generally categorized as supervised and unsupervised.

2.2.2.1 Supervised Clustering Methods

These methods use the pattern recognition concept for segmentation as human organs are reflected as patterns in medical images in which the class labels and features of a training set are stored and unlabeled points assigned a class label based on observations of the stored and unlabeled features. These algorithms normally vary based on the feature space selected from the training set, with the most common a maximum likelihood (ML) algorithm, k-nearest neighbor (kNN) classifier, support vector machine (SVM), supervised artificial neural network (ANN), active appearance model (AAM) and active shape model (ASM).

In kNN methods, a label is assigned to each pixel or voxel in the training data set according to its features while the majority voting rule is applied during the label realization of an unlabeled pixel or voxel using its K-nearest training pixel or voxel [50]. ML algorithms use parameterized probability distributions of the pixel intensities and statistical structures for segmentation [51]. In the training phase, a structures number of parameters is stored and its likelihood function maximized to determine its parameters during label realization.

Supervised ANN algorithms train an ANN using a known classification to generate a weighting code word for each output node that corresponds to different structures [52, 53], with that for an unknown image optimized to obtain a label for each class. In SVM methods, several candidate landmarks in an input image are detected in the vicinity of a landmark in the template image using region and edge-based techniques, which are subsequently reduced by template landmark deformation using a SVM regression technique iterated until the final output is obtained [54].

In AAM algorithms, the training phase incorporates information of the shape and texture variations of an object while the model's parameters are optimized to obtain the minimum difference between the input image's data and that of the model [55–57]. An ASM algorithm (an alternative to an AAM one) considers the principal component vectors as the shape model of a landmark point and the normalized first derivative of the landmarks running perpendicularly outside it as the grey-level appearance model [58, 59], with the Mahalanobis distance of the derivative regarded as the cost function.

2.2.2.2 Unsupervised Clustering Methods

Although training is not required in these algorithms, self-training is undertaken in the input image by identifying the features of each class. C-means methods, the iterative self-organizing data analysis technique algorithm (ISODATA), fuzzy C-means (FCM) techniques and unsupervised neural networks are the most common algorithms in this genre.

C-means methods are also known as K-means algorithms in which the number of objects is regarded as C or K respectively. Each pixel is allocated to a class based on its minimum distance from the initial centroid which is iteratively updated. When all the pixels are assigned to a class, the process is repeated with new centroids and new constraints until there are no more changes in the centroids. FCM algorithms have better accuracy for complex imaging conditions and wider applicability, particularly for MR brain images [60, 61], although they are slower than K-means algorithms. They operate similarly to C-means methods except that they use weights to calculate the centroids and point distances while iteratively changing the weights [62, 63]. Adding spatial impact [62, 64–67] or kernel techniques [68, 69] to FCM improves its performance. ISODATA algorithms are also operationally similar to C-means methods, with the number of classes selected by a splitting and merging technique, and are used mainly in transmission image segmentation and nuclear medicine [70–72].

Instead of using a training set, unsupervised neural networks exploit the unsupervised learning obtained from an input image in which learning rules are used to train the weights; for example, the Hopfield neural network exploits winner-takes-all as the learning rule [73, 74]. Further studies of unsupervised neural networks can be found in [75].

2.2.3 Deformable Model-based Algorithms

Medical image segmentation is a challenging task as organs are variable and compact, and have similar intensities and variations in terms of image quality due to noise, sampling artifacts, PVE and inhomogeneity [76]. Therefore, classical algorithms (such as thresholding and clustering ones) either find it difficult or fail to segment medical images which also require manual interactions. To tackle these issues, deformable models play an important role in segmentation for many complex medical applications. They are based on curve evolution techniques in which an object's boundary is considered the final state of an evolving curve. They incorporate physics, geometry and approximation theory in their algorithms in which image data and prior information about the shapes, sizes, locations and orientations of anatomical structures are easily exploited to overcome the drawbacks of traditional segmentation techniques. As these models are continuous and connected, they compensate for gaps, noise and other irregularities of a structure [77], and can yield sub-pixel accuracy as well as handle anatomical variabilities. In the literature, deformable models are also known as snakes, balloons, active contours and surfaces.

Initial studies of deformable models were published in the late 1980s [76, 78–80] and then other applications of deformable contour models appeared in the early 1990s [81–87]. However, the seminal work by Kass *et al.* [79] entitled "Snakes: Active Contours" inspired their popularity for image segmentation which can be further classified as parametric and geometric based on their contour representations and tracking processes.

2.2.3.1 Parametric Deformable Models

In these models, which are explicitly represented, the tracking is performed through sample contours or surface points [27, 76] whereby direct interactions can be achieved with fast real-time implementation. Their evolutions are carried out by energy functional or dynamic forces, with an energy functional one comprising internal and external energy that exploits priori anatomical information. The internal energy is ascertained from the geometrical properties of the model which regulate its tension or smoothness while the external energy is determined from image cues which entice the model towards the objects boundary. The minimum of the total energy, which is achieved when the model is at the objects boundary position, provides internal and external forces, with the external ones causing variations among algorithms.

As early deformable methods [79, 80] were sensitive to the model's initial position, the initial contour had to be placed near the object's boundary to obtain good results. Later, researchers attempted to avoid dependency on the initial position [82, 85, 88–93]; for instance, Cohen [82] used pressure or a balloon force with a Gaussian potential force to inflate or deflate their model when the potential force was infirm. Cohen and Cohen [85] exploited a distance map to define the potential energy in order to extend the attraction range which encountered the difficulty of boundary concavities. To solve this concavity problem, Xu and Prince [89, 91] used a gradient vector flow field which assigned a vector diffusion equation to the edge of an object. McInerney and Terzopoulos [88] applied a constraining force that exploited user-defined control points. A dynamic distance force using a signed distance from the model to object's boundary to attract the model from a fairly long distance was proposed in [92, 93]. A numerical comparison of the improvements in these algorithms can be found in [90].

Statistical shape models are also used in parametric deformable models [6, 57, 58, 94–97], where evolution of the contour's vertices is constrained by the range of the statistical shape's parameters. While a statistical shape model is not a segmentation process, it is used as a guide in various segmentation methods.

Although parametric deformable models are extensively used in many applications, they have some drawbacks. They need re-parameterization when the boundaries of a model and object vary greatly in shape, size and position which is computationally expensive in 3D and moderate in 2D. They also suffer from the difficulties of topological adaptation and self-intersection.

2.2.3.2 Geometric Deformable Models

Geometric deformable models (GDMs) [98–101] are significant frameworks for image segmentation as they enable the easy incorporation of an object's boundary and region information, and an image's appearance, topology and shape, geometric relationship with neighbouring objects and motion pattern in an image sequence [102]. The incorporation of this knowledge makes these algorithms robust against noise, missing boundaries and other medical imaging artefacts. These methods are implemented using level set (LS) and curve evolution theory in which models are implicitly expressed without parameterization and, with a zero LS evolved over time, is regarded as an embedded model (curves or surfaces). GDMs can automatically handle topological changes as they are implicitly represented and their evolutions are free of parameterization.

GDMS can be implemented as energy minimization or for the design of a model's driving forces for which they typically exploit edge information [98, 100, 103–107]; for example, the geodesic active contour [98, 103–106] method applied image gradient information to search for the best minimal smooth contour. These methods are sensitive to false edges, noise due to their dependency on local gradient information and leaking through weak boundaries. To overcome the limitations of edge-based methods, region-based GDMs, which parameterize the image regions as image features (e.g. textures, means, variances), have been proposed [99, 108–114]. Also, non-parametric regions [115] and shape optimization-based methods were recently proposed and Mesejo *et al.* [23] developed a GDM by combining edge- and region-based information that used deformable registration with prior shape information.

A topology-preserving GDM (TGDM) that monitored changes in the the sign of the LS function which can generate geometrical inconsistencies, was first proposed by Han *et al.* [116]. Segonne *et al.* [117, 118] developed a genus-preserving GDM (GGDM) for preventing geometrical inconsistencies by applying a 'multi-simple point' criterion. A topological constraint is enforced in a discrete way in both TGDM and GGDM. Shi and Karl [119] proposed a continuous TGDM using a differentiable minimum shape distance (DMSD), and Alexandrov and Santosa [120] a TGDM based on shape optimization. Sundaramoorthi and Yezzi [121] exploited a partial differential equation (PDE)-based geometric flow in their TGDM algorithm.

Leventon *et al.* [122] published the first method for incorporating the prior shape in a GDM using a principal component analysis (PCA) of shape embedding from a training set and evolving both local and global embedded shapes using curvature and image gradient information. Many other methods incorporating prior information in a GDM, including a review paper [123], have been published recently [124–129]. Most of these methods assumed linear shape variations which has two drawbacks. Firstly, the training set cannot always maintain a Gaussian distribution and, secondly, its signed distance function is non-linear. Cremers *et al.* [130, 131] and Rousson [132] proposed LS kernel density estimation-based methods incorporating prior information. Also, Cremers and Funka-Lea [133] used object dynamics for shape modeling in GDM-based segmentation. Kohlberger *et al.* [134] employed a 4D PCA in a training set to segment its whole volume by considering time as the fourth dimension.

GDMs are normally computationally expensive due to their high-dimensional LS functions and large grid sizes. However, this complexity can be reduced by using narrowband methods with re-initialization techniques [135, 136] if the grid size is small. Weickert *et al.* [137] proposed a fast GDM using additive operator splitting (AOS) which may encounter splitting artifacts owing to reduced rotational invariances when using large time steps. To address this problem, Kenigsberg *et al.* [138] and Papandreou and Maragos *et al.* [139] used multi-grid techniques in GDMs which allowed larger time steps and sped up their algorithms. Shi and Karl [140] proposed a fast GDM based on insertion and deletion operations without solving a PDE but its accuracy was not reliable. Krissian and Westin [141] developed a fast GDM with good accuracy using a re-initialization technique. Li *et al.* [142, 143] proposed a distance-regularized GDM without re-initialization which enhanced its overall efficiency. Another algorithm proposed using distance regularization with an advanced optimization and splitting strategy [144] was more efficient.

Although most GDMs deal with a single object on a single background, in the literature, there are some research studies using them with multiple objects with different characteristics and employing N LS functions for N objects [145–148]. Tsai *et al.* [149] implemented a GDM using N LS functions for N joint-shape neighbouring objects. These methods had higher computational complexity if the number of objects increased [145–148, 150–153]. Vese and Chan [150] addressed this problem using a multi-phase LS (MPLS) algorithm which needed $logN$ LS functions for topologies, including triple junctions for N phases. This framework was later extended to other multiple-object segmentation methods [115, 130, 154, 155]. Recently, Bogovic *et al.* [5] proposed a multi-object GDM (MGDM) using fixed small numbers of label and distance functions instead of LS ones which obtained good results in terms of speed, memory requirement and topology control but was not suitable for practical applications due to its segmentation output being region- rather than object-wise.

GDMs have been widely used in recent medical image segmentation and 3D reconstruction. However, they have some disadvantages. They cannot provide good results for noisy images or similar objects in a compact space as they produce spurious connected components. Also, they face difficulty in simultaneous multiple-object segmentation and, in particular, cannot provide complete parcellation among objects. Another of their significant limitations is their high computational complexity due to their high model resolutions being limited by grid resolutions. Furthermore, their optimization cannot obtain the global minimum which results in incorrect object boundaries.

2.2.4 Registration-based Algorithms

Registration (atlas)-based segmentation is a powerful tool for biomedical applications which has been extensively used during the last two decades. It can distinguish the structure of interest from other structures with similar features due to its utilization of full anatomical priori information. In it, the target image is registered with an atlas intensity image, where the atlas is considered a combination of intensity images and manually delineated ones (atlas labels) [156].

Then, the resulting transformation is used to map the atlas labels onto the target image to automatically segment this image. Therefore, the accuracy of this method depends mainly on the registration process, that is, a segmentation problem becomes a registration one. In the context of volumetric segmentation, the registration is performed in two steps: global (rigid and affine) which provides the initial alignment; and local (non-rigid, cosine-based functions, B-spline curves or LS PDEs) which produces a high-level detailed alignment. Most previously published atlas-based works were on the segmentation of brain organs. Atlas-based segmentations are normally further classified based on their atlas selection, such as optimal, statistical and multi-atlas.

In optimal atlas-based segmentation, an optimal atlas is selected before registration for a target image from a set of atlases using demographic data, including age, weight, height and gender, and the measure of similarity between the target and atlas images [157–168]. Although an optimal atlas reduces the diversity between atlas and target images, some anatomical diversity remains.

In statistical atlas-based segmentation, as an atlas that closely resembles many target images is selected [169], the optimal atlas selection operation does not need to be performed for each target image separately, with the statistical atlas needing to deform less than the optimal one for a group of target images. A statistical atlas is generated by registering all individual atlases in a common coordinate space and using intensity normalization and a pixel- or voxel-wise averaging operation to produce probabilistic maps which is computationally very expensive and may create a fuzzy atlas. These atlases can be categorized in groups based on age, sex, weight, height and right-/left-handedness, with the statistical Bayesian framework's concept used to integrate the pixel or voxel probabilities in these methods [170–178]. Variational frameworks are also used in these approaches [179] and, sometimes, other techniques that combine other image features with atlas probabilities [180, 181].

In multi-atlas segmentation (MAS), multiple atlases from a group of atlases, which are close to the target image demographically and in terms of a similarity measurement, are selected. Then, multiple segmentations are generated for the target image and fused to obtain final segmentation estimates [182]. These methods are currently well known and successful in many biomedical applications [183]. Their processes reduce segmentation errors compared with the previous two methods and better capture anatomical variabilities but incur greater computational complexity. However, advances in computer hardware have expedited improvements in MAS algorithms [184, 185] which were evolved based on atlas selection, the number of atlases and label fusion, with an extensive review of them presented in [183]. Fusion can be achieved by either majority voting (global strategy) or weighted voting (local strategy) [186–188], where the latter performs better than the former. Another fusion strategy is the simultaneous truth and performance level estimation (STAPLE) [189, 190] which is popular in multi-atlas-based segmentation methods.

Although registration-based algorithms play an important role in medical image segmentation, they cannot handle anatomical variabilities as they do not have a suitable registration framework for achieving good alignment between two images demographically close to each other. While there is a registration framework for the human brain, it is ineffective for other human body parts, such as the neck, abdomen and thighs in which respiratory motions cause sliding between the organs' walls.

2.3 Discussion and Guidelines for Segmentation of Neck Muscles

There is no optimal generalized segmentation algorithm as each specific application requires a certain type of method due to its inherent goals and constraints. Medical image segmentation is a really challenging task compared with conventional image segmentation due to the low resolution, noise, intensity inhomogeneity, low contrast, compactness of similar structures and similar background intensities of images near the ROI. As these difficulties limit the application of classical segmentation techniques, such as thresholding and clustering, as a total segmentation process, these techniques are used for pre and post-processing in conjunction with others. Thresholding methods normally produce leaking, spurious connections, discontinuous or wrongly connected boundaries and merging in medical image segmentation which require moderate amounts of manual interaction. Similarly, clustering techniques suffer from over-segmentation, are sensitive to the selection of the initial group and thresholds, have incomplete boundaries and leaking which require distinct features to be found and manual interaction to obtain complete segmentation. Gathering training data, which is laborious and very time consuming, is another important shortcoming of these methods.

To address this issue, incorporating prior information in segmentation algorithms, which can be achieved through deformable models and registration-based segmentation techniques, plays a significant role in medical image segmentation. GDMs are popular in deformable-based methods and multi-atlas techniques in registration-based ones. However, GDMs are not compatible in the context of neck muscles which have inherent anatomical complexities, as discussed in the following chapters. Also, they normally provide spurious connected components in noisy images and those with compact organs, and cannot completely separate objects which are compact and similar in intensity. Although parametric models involve re-parameterization and are incapable of handling topology adaptation problems, they can produce good results for neck muscles segmentations using a complicated process. On the other hand, registration-based algorithms are good prospects for segmenting neck muscles. Although multi-atlas based segmentations have been successful for some human organs segmentations, they have not yet been widely accepted for clinical applications due to their shortcomings of computational complexity and their registration processes being ineffective for other body parts because of respiratory motions that cause sliding in organs walls. Therefore, an effective registration framework could play an important role in neck muscles segmentation.

Chapter 3

Registration and Deformable Model-based Neck Muscles Segmentation and Reconstruction

---

This chapter presents a novel and complete algorithm for the automatic delineation and 3D visualization data of some of the specific neck muscles responsible for injurious neck pain. It uses linear and non-linear registration frameworks to amend inequalities between the training and testing tomographic data. It can handle posture variabilities among patients using an alignment plan and also exploits a cognition-based grouping adjustment to enhance segmentation accuracy. The remainder of this chapter is organized as follows: Section 3.1 presents a relevant literature review of muscles segmentation methods and the motives for designing a registration and deformable model-based neck muscles segmentation approach; 3.2 details of the proposed segmentation methodology; 3.3 the experimental arrangement and system performance analysis; 3.4 system's pros and cons; and 3.5 conclusion.

3.1 Introduction

The planning of treatment for the neck region relies on having exact diagrams of anatomical structures, as this area contains many sensitive organs, such as nerves, blood vessels, the spinal cord, spinal canal and trachea. Therefore, precise accuracy is required for treatment intervention. However, delineation is the pre-requisite for diagrammatically representing anatomical structures. Also, for minimally invasive treatment, the surgeon and therapist need to know the exact positions of both affected and normal organs. Previous segmentation techniques for the neck region focused mainly on the vertebrae [191, 192], inter-vertebral discs [6], trachea [193], spinal cord [40, 194], endorrhachis and nerve roots [195] but not the neck muscles. Segmenting neck muscles is difficult compared with segmenting other anatomical neck organs which have better contrast and spatial sparseness in medical imaging data. In this chapter, the proposed new method is used to segment the sternocleidomastoid, obliquus capitus inferior, semispinalis capitis and splenius capitis cervical neck muscles.

Compared with segmenting bones and other anatomical organs from medical images, segmenting muscles is a challenging task due to their identical textures, intensities, contrast and compactness in the human body. In some areas, the muscles are so close that the current resolution of imaging devices cannot separate neighbouring ones in the medical images produced. Moreover, medical images can be distorted due to imaging noise and inhomogeneity. Also, in a clinical image, the *intra*-muscular fat's gradient can be greater than the *inter*-muscular border's gradient which creates false muscle boundaries so that even expert clinicians may face confusion during manual segmentation of muscles. Additionally, the anatomy of neck muscles is more complex than those of the thigh, leg and hip muscles because neck muscles are both smaller and more compact (Fig. 3.1) while some other organs have almost similar intensities. It can be seen in Fig. 3.1 that the inter-muscular boundaries of the thigh, hip and leg are more perspicuous than those of the neck and their muscle sizes are comparatively wider.

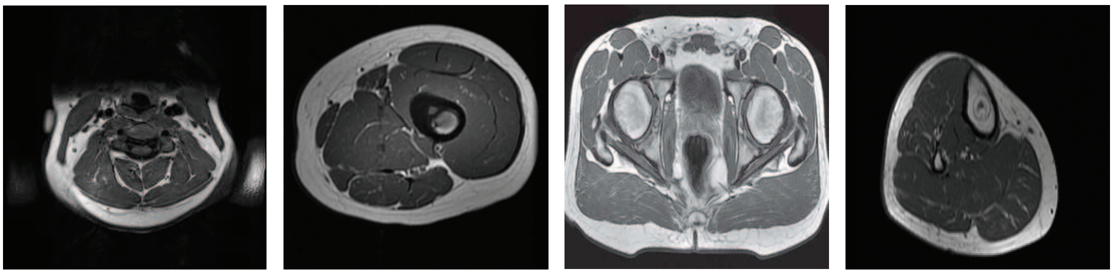

(a) (b) (c) (d)

Figure 3.1: Comparison of anatomical complexity of different human body muscles: (a) neck; (b) thigh [1]; (c) hip [2]; and (d) leg [3].

Some research conducted on the segmentation of thigh, leg, hip, tongue and pectoral muscles is reported in the literature [4, 8, 22, 24, 196–205]. Andrews *et al.* [22] demonstrated a thigh muscle segmentation method using a generalized log-ratio (GRL) representation of thigh muscles with anatomical registration and a random forest (RF) classifier for inter-muscular boundary detection, with a convex energy functional for global minimization. However, their GRL transformation could not incorporate all the prior anatomical information nor did the RF recognize certain boundary pairs. Baudin *et al.* proposed a procedure for automatically detecting voxels inside thigh muscles using a rigid registration and pre-segmented atlas which obtained good results using these voxels as seeds for subsequent segmentation [24] but their seed placement technique was not reliable. Ahmad *et al.* in [8] propounded an automatic thigh muscle segmentation process using an active snake contour curve deformation with training segmentation as the structural regularization which required a manual interaction in the mid-scan of the data set. This method segmented quadriceps muscles, femur cortical layer and bone marrow together not separately.

Essafi *et al.* in [197] employed a wavelet-based enciphering of the topology of calf muscles which also exploited provincial properties for the searching process but depended on landmarks and could face difficulty in detecting false boundaries.

Wang *et al.* in [199] combined corrective learning with an auto-context learning method in a multi-atlas fusion label process for canine leg muscle segmentation. Ray *et al.* in [198] segmented multiple muscles through 3D to 2D mapping and a prior training data set.

Pectoral muscle segmentation from breast MRI and mammography was considered in [201–204]. Ganesan *et al.* in [201] provided a survey of pectoral muscle segmentation research papers. In [204], an adaptive algorithm for automatically segmenting pectoral muscles by straight-line estimations from mediolateral oblique-view mammograms and iterative cliff detection was proposed. A multi-atlas and probabilistic model-based pectoral muscle segmentation from MRI was considered in [203] but this method could not compensate for individual variabilities. Mustra and Grgic proposed a breast tissue segmentation method by estimating the breasts skin line and segmenting the pectoral muscle from the segmented breast tissue through polynomial estimations and contrast enhancements from mammograms [202].

Ibragimov *et al.* [200] established a method for segmenting tongue muscles from super-resolution MR images using a game-theoretic framework and landmark. However, they segmented only two muscles from healthy subjects and did not consider any pathological images.

Jurcak *et al.* [205] studied segmenting the quadratus lumborum hip muscle from MR images by exploiting probabilistic atlases in a non-rigid registration framework with a geodesic active contour conformation.

In conclusion, almost all previous muscle segmentation methods utilized anatomical information by either explicitly or implicitly encoding a fundamental step in their automatic segmentation algorithms. Atlas-based segmentation methods, which use explicit anatomical knowledge in terms of manual segmentation, are promising as they can simultaneously segment several structures while preserving anatomical topology and have recently been used extensively for the segmentation of anatomical structures. Although there are many recent and potential research studies of atlas-based segmentation [156, 168, 183–185, 206], its accuracy depends mainly on image registration. The proposed method consists of a novel deformable registration for atlas-based segmentation which uses discrete cosines as the basis function and a new adaptation technique that employs topological knowledge during grouping. It can both preserve topology and cope with shape variabilities among different patients as well as supporting manual analysis using 3D reconstruction after automatic segmentation.

In this study, the following method is established for the automatic segmentation of neck muscles.

- An affine registration technique is proposed which uses three-level Gaussian filtering of reference and floating image volumes before registration, with the sum-of-conditional variance with partial volume interpolation (SCVPVI) as the similarity measure for the Gauss-Newton gradient descent optimization technique. This registration eradicates the global mismatch between the reference and sensed volumes through translating, rotating, scaling and shearing the sensed volume.

- A novel discrete cosines-based elastic registration is introduced in slice- and block-wise ways which is able to remove discrepancies in the higher-order shape moments between the two volumes as its warping depends on the similarity measure between the two images, the coordinate mesh grid values and gradients of the floating image.

- In addition, a label transfer process is developed for the affine, and slice- and block-wise elastic registrations.

- Finally, the transferred labels are refined using a new knowledge-based grouping adaptation technique to improve segmentation accuracy. It uses three forces to move the vertices of a muscle contour and employs a technique for removing overlaps among adjacent muscles. A new stopping criterion is also introduced in terms of the image features of the contour vertices.

3.2 Segmentation Method

In the proposed approach, a schematic registration framework is used to align the template and target image volumes in order to segment the latter. The main purpose of this registration is to relate the corresponding points in these volumes so that landmark labels can be mapped from the former into/onto the latter, i.e, to obtain a transformation ($\mathbf{T} : (x', y', z') \mapsto (x, y, z)$). However, as the type of mismatch between two different patients anatomical structures varies according to their different shapes, respiratory and cardiac motions and gestures, it cannot be corrected using only an affine transformation. Therefore, a hierarchical registration framework is used which exploits both global and local transformations as

$$\mathbf{T}(x, y, z) = \mathbf{T}_{global}(x, y, z) + \mathbf{T}_{local}(x, y, z). \tag{3.1}$$

In the following subsections, these registration algorithms are presented using $I(x, y, z)$ and $I'(x', y', z')$ as the reference and moving images respectively.

The methodology is as follows. Subsection 3.2.1 describes the SCVPVI-based affine registration and similarity measure method while 3.2.2 discusses the discrete cosines-based elastic registration process. Subsection 3.2.3 presents the optimization technique for the affine and elastic registrations and subsection 3.2.4 describes the process for transforming the label from the training to novel volume. The knowledge-based grouping adaptation technique is discussed in subsection 3.2.5 and, finally, subsection 3.2.6 explains the atlas selection manoeuvre for segmentation.

3.2.1 Sum-of-conditional Variance with Partial Volume Interpolation (SCVPVI)-based Global Affine Registration

The affine transformation performs the overall motion between the moving and reference image volumes using 12 degrees of freedom to correct the scaling, rotation, translation and shearing between them. Three-level low-pass Gaussian filtering is applied on both the moving and target volumes before registration to aid optimal convergence. As this action smooths sharp changes in both the image volumes, a smooth gradient is obtained across the whole volume which is useful in the gradient-based optimization technique. During the registration, the most blurred of the three images is used first followed by the remaining ones in descending order. The experimental data set contains 15 image volumes with different image contrast properties because, despite using the same MRI scanner, almost all different volumes experience different echo and repetition times. Although these differences reduce registration accuracy, they can be removed by re-normalization [171]. The geometrical transformation function for the affine registration is given by

$$\begin{aligned} x' &= e_0 + e_1 x + e_2 y + e_3 z \\ y' &= f_0 + f_1 y + f_2 z + f_3 x \\ z' &= g_0 + g_1 z + g_2 x + g_3 y. \end{aligned} \tag{3.2}$$

where e_0, e_1, e_2, e_3, f_0, f_1, f_2, f_3, g_0, g_1, g_2 and g_3 are spatial parameters.

The matrix form of the affine transformation model can be written as

$$\begin{bmatrix} x' \\ y' \\ z' \\ 1 \end{bmatrix} = \begin{bmatrix} e1 & e2 & e3 & e0 \\ f3 & f1 & f2 & f0 \\ g2 & g3 & g1 & g0 \\ 0 & 0 & 0 & 1 \end{bmatrix} \begin{bmatrix} x \\ y \\ z \\ 1 \end{bmatrix} \tag{3.3}$$

One of the key foundations of an image registration process is the similarity measurements of the image volumes for which many techniques have been used in the literature, such as mutual information (MI), normalized mutual information (NMI), conditional mutual information (CMI) and entropy sum-of-squared difference (eSSD), with some recent research papers using the SCV as the similarity metric [207–211]. In the SCV similarity measure, the voxel values of the reference and moving images can be identified as I_i and I'_i respectively for $i = 1, \cdots, M$ voxels in the image volumes, with the subscript i denoting these values at coordinates (x_i, y_i, z_i) and (x'_i, y'_i, z'_i) in I and I' respectively.

Then, the SCV between I and I' is given by

$$\mathrm{SCV}(\mathbf{m}) = \sum_j E\left(\left[I'_i - E\big(I'_i | I_i \in \Delta_j\big) \right]^2 \middle| I_i \in \Delta_j \right) \tag{3.4}$$

where E is the expectation operator, Δ_j a set of histogram bins that span the range of values of I and $\mathbf{m}$ the vector of the affine transformation parameters.

The conditional mean in equation (3.4) is derived from the joint histogram of I and I'. Equation (3.4) can be rewritten as

$$\mathrm{SCV}(\mathbf{m}) = \sum_{j=1}^{M} \left(I'_i - \hat{I}_i \right)^2 \tag{3.5}$$

where

$$\hat{I}_i = E(I'_i | I_i \in \Delta_b) \tag{3.6}$$

and Δ_b is recognized as the histogram bin comprising I.

As the structure of (3.5) is identical to the sum-of-squared difference (SSD), Gauss-Newton optimization can be used in conjunction with the SCV.

However, an estimate of the reference image volume is required during the SCV calculation which takes the conditional expectation using the joint histogram from the quantized reference and moving image volumes. To overcome the problem that this process ignores a huge amount of information from the reference volume, PVI is used in connection with the SCV, as discussed in [208].

3.2.2 Discrete Cosines-based Elastic Registration

The affine mapping, which can correct only a coarse mismatch but not a small local discrepancy, provides substantial initialization for the registering of a local discernible mismatch. It also yields registered volumes where the corresponding slices of those volumes contain the same anatomical information with differences only in local details. However, this discrepancy cannot be removed using a global elastic registration due to the undesired stretching and shrinking caused by possible overfitting of the image landmarks. Moreover, the global SCV optimization using elastic registration is more difficult than for local SCV. Therefore, local elastic registration is required to neutralize local discrepancies. In the context of neck muscle segmentation, large anatomical variabilities can arise according to a patient's weight, height, age and gender. Therefore, as it is difficult to correct any discrepancy using a single local elastic motion model with a parameterized transformation, in this work, four local motion models are exploited in separate steps.

Commowick *et al.* [212] proposed a local affine registration that exploited separate optimizations for different regions which could affect registration accuracy owing to the impairment of global intensity cohesion among local regions. Zhuang *et al.* [213] also developed a local affine registration method using a global optimization system for all local regions which could involve high computational complexity. However, a local registration method enhances efficacy and computational performance by the driving force of mapping the parameters' confinement into local regions. For this reason, a new topology preserving locally diffeomorphic mapping is proposed in a slice-by-slice way in 3 steps with different parameters and higher degrees of freedom. Then, a block-wise registration using the same mapping is employed to further align the image volumes. As the slice-wise local elastic motion model restrains its driving energy in a more sophisticated fashion than a 3D local elastic motion model, it promotes efficiency. It can also retain the global intensity linkage owing to using the same basis function in every slice. The developed amalgamated local transformation which challenges shape variabilities is

$$\mathbf{T}_{local}(x, y, z) = \mathbf{T}_{slicewise}(x, y, z) + \mathbf{T}_{blockwise}(x, y, z). \tag{3.7}$$

In its first step, this elastic registration framework takes input from the global affine registration using 8 motion parameters which then provides initialization for 18 motion parameters in its second step and, similarly, 32 in its third. Finally, a local block-wise registration, for which each MRI slice is divided into four blocks, is performed by taking its input from the slice-wise registration's output in the last step. This hierarchical initialization process helps to obtain fine alignment between the reference and moving image volumes. Although block-wise registration slightly harms a global intensity linkage, it yields good local detail corrections for anatomical structures. However, any intensity linkage breakdown does not create any problems during a label transfer for segmenting muscles.

In this study, an elastic motion model is selected based on discrete cosines which was previously successfully used in video coding [214]. Its main aim is to deform a structure by changing the mesh of the floating image depending on the error between two images, the basis function and the gradient of the floating image. To describe this model, consider $I(x, y)$ and $I'(x', y')$ as the reference and floating images respectively and the image domain as $\Psi = \{(x, y)|0 \leq x \leq M - 1\}, 0 \leq y \leq N - 1\}$. Let Θ denote a $g_x \times g_y$ mesh grid with homogeneous spacing (τ). Then, the coordinates of the two images are involved in a typical elastic image registration as

$$\begin{aligned} x'_i &= x_i + \sum_{k=1}^{P/2} m_k \varphi_k(x_i, y_i) \\ y'_i &= y_i + \sum_{k=P/2+1}^{P} m_k \varphi_k(x_i, y_i) \end{aligned} \tag{3.8}$$

where m_k are the motion parameters, φ_k the basis functions for the complex mapping and P the number of motion parameters. Many other basis functions, such as wavelets, radial basis functions, harmonic functions, polynomials and B-splines, have been used in the past [215].

A set of discrete cosines is used as the basis functions to obtain elastic or non-rigid motions between two neck volumes. Discrete cosines can achieve dense parameterizations which are essential for non-translational motions and can also convey smooth discrepancies using a minimum number of coefficients. Another motivation for using discrete cosines is their widespread popularity and hardware achievements in various image and video processing applications. The basis functions of the geometrical transformation are given by

$$\begin{aligned}\varphi_k(x_i, y_i) &= \varphi_{k+P/2}(x_i, y_i) \\ &= \cos\left(\frac{(2x_i+1)\pi u}{2M}\right)\cos\left(\frac{(2y_i+1)\pi v}{2N}\right)\end{aligned} \tag{3.9}$$

where $k = su + v + 1,\ u, v = 0, 1, 2, \cdots, s-1,\ s = \sqrt{\frac{P}{2}}$, and M and N are the horizontal and vertical dimensions of the images to be registered respectively; for instance, the motion fields corresponding to each basis function for such a coordinate transformation are displayed in Fig 3.2, where $P = 8, s = 2$ and $M = N = 4$.

3.2.3 Gauss-Newton Optimization

The purpose of this optimization is to calculate the motion parameters which minimize the SCV similarity measure and are used during the inverse transformation for segmentation. Gradient-based optimization algorithms are popular in image processing and computer vision applications for optimizing motion parameters during the image registration process. Usually, the SSD between the reference and floating images is minimized in gradient-based optimization techniques and

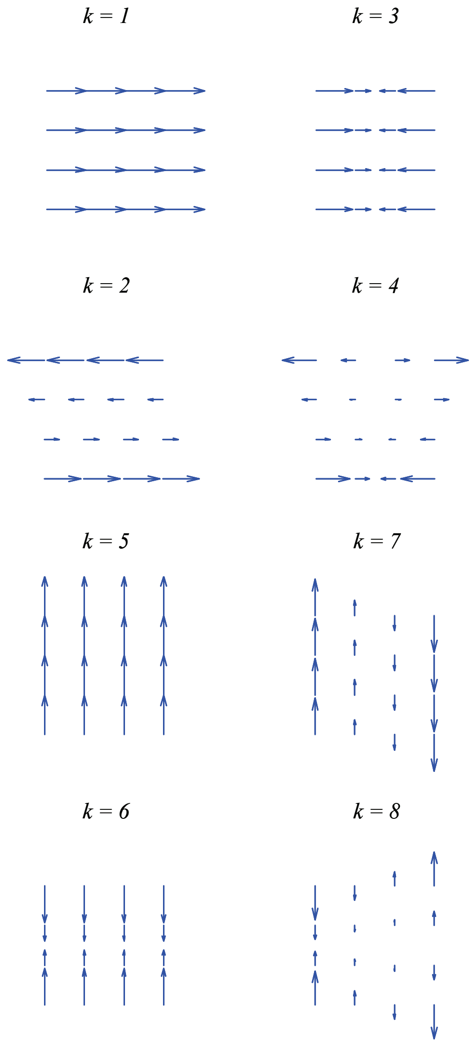

Figure 3.2: Motion fields corresponding to each basis function of elastic warping function when $P = 8$, $s = 2$ and $M = N = 4$.

that between $I(x, y)$ and $I'(x', y')$ can be expressed as

$$E = \sum_{i=1}^{T} [I'(x', y') - I(x, y)]^2 = \sum_{i=1}^{T} e_i^2 \tag{3.10}$$

where T is the total number of pixels in an image and e_i the intensity difference between I_i and I'_i. The floating image is iteratively warped using interpolation to minimize the SSD between the two images based on the current discrepancy condition. The Lucas-Kanade algorithm is generally used to optimize the SSD in an image registration technique and is also known as the Gauss-Newton gradient descent non-linear optimization algorithm [216]. It is used in our work for the affine, and slice- and block-wise registrations, with a first-order Taylor series approximation used to linearize the non-linear equation in (3.10). Then, after updating the motion parameters by an increment ($\triangle m$), this equation becomes

$$\begin{aligned} E' &= \sum_{i=1}^{T} \left[\left(I' + \frac{\partial I'}{\partial m} \triangle m \right) - I \right]^2 \\ &= \sum_{i=1}^{T} \left[\frac{\partial I'}{\partial m} \triangle m + e_i \right]^2 \end{aligned} \tag{3.11}$$

For clarity and ease of notation, the images functional dependency is ignored on the coordinate. The partial derivative of E' with respect to the parameter increment for minimizing the SCV is

$$\frac{\partial E'}{\partial \triangle m} = 2 \sum_{i=1}^{T} \frac{\partial I'}{\partial m} \left[\frac{\partial I'}{\partial m} \triangle m + e_i \right] \tag{3.12}$$

After equating zero for error minimization, this equation becomes

$$\sum_{i=1}^{T} \left[\frac{\partial I'}{\partial m} \right]^2 \triangle m = - \sum_{i=1}^{T} \frac{\partial I'}{\partial m} + e_i. \tag{3.13}$$

Writing this equation in matrix notation gives

$$\mathbf{H} \triangle m = \mathbf{b} \tag{3.14}$$

where $\mathbf{H}$ represents the Hessian matrix and $\mathbf{b}$ the steepest descent parameter updates which are calculated as $\mathbf{H}_{k,l} = \sum_{i=1}^{T} \frac{\partial I'}{\partial m_k} \frac{\partial I'}{\partial m_l}$ and $\mathbf{b}_k = - \sum_{i=1}^{T} \frac{\partial I'}{\partial m_k} e_i$.

The $\frac{\partial I'}{\partial m_k}$ can be determined using matrix multiplication and the chain rule as

$$\begin{aligned} \frac{\partial I'}{\partial m_{k=1:P/2}} &= \frac{\partial I'}{\partial x'}\frac{\partial x'}{\partial m_k} \\ \frac{\partial I'}{\partial m_{k=P/2+1:P}} &= \frac{\partial I'}{\partial y'}\frac{\partial y'}{\partial m_k} \end{aligned} \tag{3.15}$$

where $\partial I'/\partial x'$ and $\partial I'/\partial y'$ are the horizontal and vertical gradients of the floating image respectively, and $\partial x'/\partial m_k$ and $\partial y'/\partial m_k$ are equal to the basis functions of the transformation in elastic registration, i.e., $\frac{\partial x'}{\partial m_k} = \varphi_k(x_i, y_i)$ and $\frac{\partial y'}{\partial m_k} = \varphi_k(x_i, y_i)$ respectively. In the affine registration, the terms $\partial x'/\partial m_k$, $\partial y'/\partial m_k$ and $\partial z'/\partial m_k$ are equal to coordinate mesh grids. The motion parameters of the transformation function are updated iteratively as

$$\begin{aligned} m^{t+1} &= m^t + \triangle m \\ &= m^t + \mathbf{H}^{-1}\mathbf{b} \end{aligned} \tag{3.16}$$

where t represents an iteration superscript. The updated motion parameters are used to recalculate the floating image, $\mathbf{H}$ and $\mathbf{b}$ in every iteration. The increment in the motion parameter is calculated in each iteration by warping the floating image until a minimum E is found that satisfies a stopping criterion.

3.2.4 Label Transfer

Original MRI volumes are used in the registration process while saving the muscles' contour vertices of the floating image volume in a structure. Once the motion parameters are known from the registration process, these vertices are easily transferred by an inverse transformation from the floating image volume to an image volume to be segmented for affine and slice-wise elastic registrations since a parameterized geometrical transformation function is used. For the block-wise registration, a new technique is proposed for transferring the muscles' contours in which each contour vertex is transferred using the motion parameter set of a block containing it. This means that if a contour vertex belongs to the first block, the set of registered motion parameters of this block are used to transfer from the floating to reference image.

3.2.5 Knowledge-based Grouping Adaptation

The initial segmentation results produced by the registration and label mapping processes are refined using a deformable contour model to improve the accuracy of auto-segmentation, with the mapped labels acting as the initial contours. However, as the deformable contour models available in the literature can only yield good deformations if there is no other nearest edge in the proximity of the structure to be segmented, they cannot be used to segment neck muscles which occupy spaces in such a way that they stay very close to each other. In this work, a new deformable model is proposed based on simultaneous segmentations of a group of muscles in close proximity to each other using their anatomical spacing information and an overlap removal technique. In this technique, the initial overlap among adjacent transferred labels is removed in the first iteration and the dynamic contours cannot penetrate the regions of the nearest muscles in the remaining iteration. As a result, the opportunity for the vertices of a contour to be affixed to nearby object edges is reduced. Therefore, this technique can segment muscles in very close proximity to each other, as in the anatomy of the neck.

In the grouping adaptation, the vertices of a contour are re-sampled using 1D spline interpolation which increases the model's resolution and thereby enhances segmentation accuracy. One internal and two external driving forces are calculated for each vertex of a contour in the deformation process, with each internal

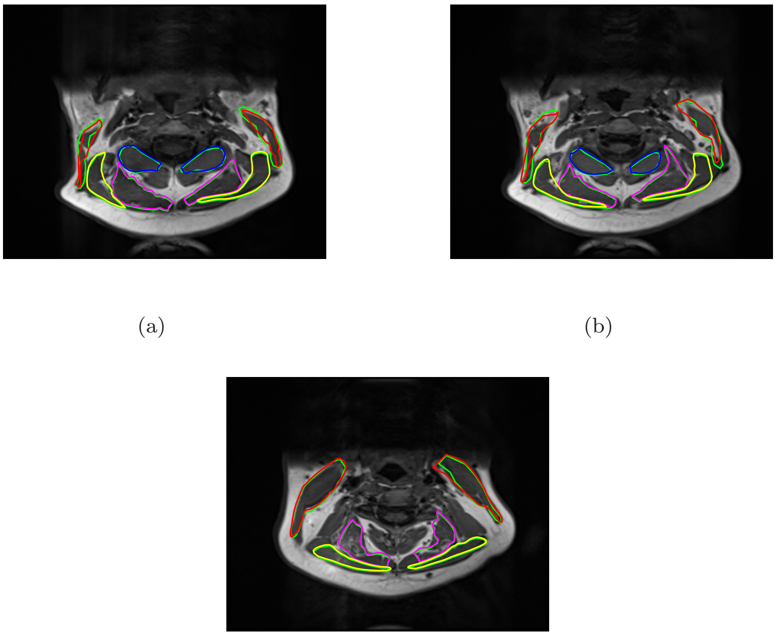

(a) (b)

(c)

Figure 3.3: Axial cross-sectional slices from one patient representing knowledge-based grouping adaptation of bilateral sternocleidomastoid (red), obliquus capitus inferior (blue), semispinalis capitis (cyan) and splenius capitis (yellow) muscles labels, with green curves transferred labels, after refinement.

force derived from the local curvatures of the contour model which minimize the local contour curvature and smooths the model. The external forces, the Gaussian potential and dynamic distance forces drag the contour model towards the object boundary and are calculated over the image domain. The detailed process of the proposed knowledge-based grouping adaptation is discussed on chapter 4. Figure. 3.3 shows the adaptation results for one patient generated by two groups which create the muscles on the left or right side because those muscles are closer to each other.

3.2.6 Atlas Selection

In a registration-based segmentation method, the atlas selection for a novel image is an important issue for obtaining good segmentation results. In this method, demographics data and the SCV similarity measure are used for optimal atlas selection. The anatomy of neck muscles depends on a patient's age, weight, height and gender. In this work, an atlas is chosen initially for a novel image based on demographics data and the final selection is made using the SCV similarity measure, as described in subsection 3.2.1. As the main factors for anatomical variations among patients are weight, height and gender, a high priority is placed on weight and height and age is considered a flexible criterion for atlas selection. In this way, a ranking list is obtained for specific novel images and the highest ranked atlas is chosen.

3.3 Experimental Results and Analysis

3.3.1 Experimental Setup

3.3.1.1 Patients Statistics

Clinical neck MR image volumes of 15 patients with ages ranging from 19 to 35 years were used in the experiment captured by the Canberra Imaging Group at Calvary John James Hospital, Deakin, Canberra, Australia. The data set contains 10 female and 5 male patients, 8 of whom suffer from moderate to acute WAD and the other 7 are healthy controls. Their weights range from 43 to 121 kilograms and their heights from 1.5 to 2.18 meters. The detail demographics data of the patients' is presented in Table 3.1. The ethics was approved for this research from

Table 3.1: Demographics data for patients'.

Patient index	age(year)	Weight(Kg)	Height(m)	Gender	Disease state
Patient-1	30	121	1.78	Male	Whiplash
Patient-2	30	105	1.78	Male	Healthy control
Patient-3	22	74	1.58	Female	Whiplash
Patient-4	32	59	1.64	Female	Healthy control
Patient-5	22	97	1.71	Female	Whiplash
Patient-6	34	70	1.75	Female	Whiplash
Patient-7	25	84	1.8	Male	Healthy control
Patient-8	22	70	1.75	Male	Whiplash
Patient-9	19	59	1.65	Female	Healthy control
Patient-10	35	90	1.63	Female	Healthy control
Patient-11	26	102	2.18	Male	Whiplash
Patient-12	27	61	1.62	Female	Healthy control
Patient-13	34	56	1.58	Female	Whiplash
Patient-14	27	57	1.65	Female	Healthy control
Patient-15	32	43	1.5	Female	Whiplash

both human research ethics committee of ACT government health directorate and Australian National University (ANU).

3.3.1.2 Imaging Parameters

A 3-Tesla Skyra MRI scanner (Siemens, Erlangen, Germany) was used to capture axial 4 mm thick slices with 4 mm spaces between them from the cervical spine of each patient. Each image was a T1-weighted magnetic resonance image with a 256×256 image dimension, 0.8594×0.8594 pixel spacing and SE MR protocol. Each MRI volume contained 45 slices without fat suppression and with intensity inhomogeneity artefact. The scanner used a repetition time of approximately 735 ms to 1140 ms, an echo time of around 15 ms, a flip angle of 70 degrees, an imaging frequency of 123.2567 Hz and a field of view of $100mm^2$. This data set was very challenging in terms of muscle segmentation because of the large anatomical shape variations among patients due to their weight differences, the inhomogeneity and low contrast in each image, the similar intensities and textures of muscles, and the presence of intra and inter-muscular fat.

3.3.1.3 Atlas Generation

A medical intern of Australian National University in Canberra hospital with sound anatomical knowledge performed a manual delineation of the 50 bilateral neck muscles in the image volumes using a Matlab graphical user interface (GUI) to obtain the ground truth and atlas volume against which the auto-segmentation results were validated. A Senior Lecturer of ANU College of Medicine, Biology and Environment and a Clinical Research Coordinator of Canberra Hospital as well as Senior Lecturer of ANU Medical School later validated and edited those atlas volumes, which were used for evaluation. In this work, segmentation was performed for the left and right sternocleidomastoid muscles, left and right obliquus capitus inferior, left and right semispinalis capitis, and left and right splenius capitis muscles automatically because their cross-sectional areas (CSAs) normally change due to a WAD [13].

3.3.1.4 Parameter Selection

In the affine registration stage, the kernel size of the Gaussian filter was 13 and the sigmas for the three levels were 0.1, 1 and 2. The kernel size determines the rate of smoothing on the image and sigma controls detail selection of the image. The SCV technique employed 256 quantization levels with 40 iterations and the partial volume interpolation technique. The quantization level in registration process maintains computational time and detail for measuring similarity whereas computational time and detail is proportional to quantization levels. In the slice-wise elastic registration, the kernel sizes were 30, 15 and 10 for the three-level

Gaussian filtering and the corresponding standard deviations 2.02, 1.5 and 0.08 respectively. The joint histogram utilized 64 quantization levels with the linear interpolation technique. The slice-wise elastic registration used 80, 80 and 60 iterations for the three steps respectively and the block-wise elastic registration 10, 5 and 3 kernel sizes for three-level filtering with 0.9, 0.4 and 0.02 standard deviations respectively, 20 iterations with spline interpolation and 64 quantization levels. The knowledge-based grouping adaptation employed 3, 1, 0.3 and 0.1 standard deviations respectively in the four steps of the Gaussian filter for calculating the potential energy distribution used in calculations of both the external and dynamic distance forces. The initial threshold for the left and right sternocleidomastoid muscles was 1200 because, as the proximity of these muscles is very obvious, their edges give a higher gradient in the Gaussian potential energy function. Conversely, the thresholds for both the left and right obliquus capitus inferior, semispinalis capitis and splenius capitis muscles were relatively low due to their close proximity to other muscles and background organs having similar image intensities. The closeness of these muscles, which had thresholds of 2, 5 and 2 respectively in the initial deformation process, can be seen in Fig. 3.3. The parameters of this method are presented in Table 3.2.

3.3.2 Performance Analysis

The proposed method was tested on 15 MRI volumes using the leave-one-out technique. Each novel volume considered 14 MRI volumes as training candidate from which an optimal one was selected using demographics data and the SCV method discussed in subsection 3.2.6.

The automatic segmentation results obtained for eight neck muscles from one of the MRI volumes using a single optimal atlas are shown in Fig. 3.4 in which it

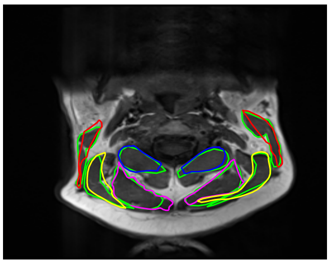

(a)

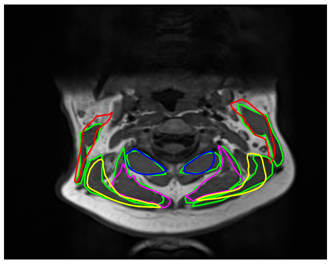

(b)

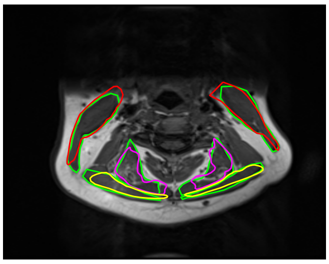

(c)

Figure 3.4: Axial cross-sectional slices from one patient depicting auto-segmentations of bilateral sternocleidomastoid (red), obliquus capitus inferior (blue), semispinalis capitis (magenta) and splenius capitis (yellow) muscles, with green curves indicating ground truth.

Table 3.2: Parameters Table

Process	Kernel Size	Sigma	Iterations	Level of Filtering	Quantization Levels
Affine Registration	13 13 13	0.1 1 2	40	3	256
Slice-wise Elastic Registration	30 15 10	2.02 1.5 0.08	80 80 60	3	64
Block wise Elastic Registration	10 5 3	0.9 0.4 0.02	20	3	64
Knowledge-based Adaptation	40 40 40 40	3 1 0.3 0.1	10 10 10 10	4	-

can be seen that they matched those for manual segmentation fairly well which was also verified by the three medical experts. Moreover, Fig. 3.5 presents the

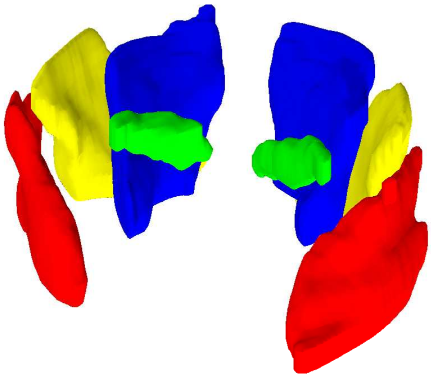

Figure 3.5: Depictions of volumetric auto-segmentations of patients bilateral sternocleidomastoid (red), obliquus capitus inferior (green), semispinalis capitis (blue) and splenius capitis (yellow) muscle volumes from C1 to C7 intervertebral levels.

automatic volumetric segmentation results generated using our developed GUI. Each 3D image can be rotated three dimensionally using zoom in, zoom out and panning tools to obtain a detailed shape and spatial relation analysis so that a physician can understand the reasons for a WAD. The automatic and manual segmentations were compared in a slice-wise manner for the C1 to C7 intervertebral levels considered as the region of interest (ROI) for a WAD [13] to calculate the mean DSC for each muscle in each patient, which are shown in Table 3.3. The average DSC values for 15 patients with standard deviations for the eight muscles are presented in Table 3.4. It is noted that the splenius capitis muscle had a relatively low mean DSC due to other high-gradient magnitudes existing near it. As this table also gives a 0.85 overall mean DSC for eight muscles with a 0.02 standard deviation, the proposed method provided consistent and quite accurate segmentations.

To the best of the author's knowledge, there is no other work on neck muscle segmentation in the literature. Therefore, it is difficult to directly compare the proposed and other methods since the anatomy of the neck is different from those of other parts of the human body, as shown in Fig. 3.1. Although there are some

Table 3.3: Mean DSC values over C1 to C7 intervertebral levels of different individuals for left sternocleidomastoid (Left Stern.), right sternocleidomastoid (Right Stern.), left obliquus capitus inferior (Left Obli. Capi. Infe.), Right obliquus capitus inferior (Right Obli. Capi. Infe.), Left semispinalis capitis (Left Semi. Capi.), Right semispinalis capitis (Right Semi. Capi.), Left splenius capitis (Left Sple. Capi.), Right splenius capitis (Right Sple. Capi.).

Patient index	Left Stern.	Right Stern.	Left Obli. Capi. Infe.	Right Obli. Capi. Infe.	Left Semi. Capi.	Right Semi. Capi.	Left Sple. Capi.	Right Sple. Capi.
Patient-1	0.84	0.85	0.86	0.83	0.84	0.86	0.84	0.85
Patient-2	0.87	0.86	0.88	0.84	0.88	0.89	0.79	0.86
Patient-3	0.91	0.87	0.93	0.82	0.85	0.87	0.8	0.87
Patient-4	0.83	0.85	0.92	0.87	0.86	0.85	0.85	0.83
Patient-5	0.86	0.85	0.92	0.84	0.92	0.9	0.81	0.82
Patient-6	0.84	0.85	0.87	0.86	0.82	0.86	0.82	0.8
Patient-7	0.87	0.86	0.86	0.85	0.81	0.91	0.86	0.87
Patient-8	0.79	0.82	0.92	0.89	0.84	0.87	0.78	0.81
Patient-9	0.89	0.88	0.84	0.84	0.86	0.85	0.79	0.82
Patient-10	0.83	0.84	0.94	0.83	0.87	0.84	0.83	0.83
Patient-11	0.82	0.83	0.85	0.83	0.85	0.92	0.84	0.84
Patient-12	0.83	0.82	0.85	0.86	0.83	0.86	0.8	0.85
Patient-13	0.85	0.84	0.88	0.84	0.91	0.88	0.85	0.86
Patient-14	0.86	0.85	0.89	0.86	0.84	0.89	0.82	0.84
Patient-15	0.84	0.84	0.87	0.88	0.85	0.9	0.8	0.88

Table 3.4: Mean DSC values for eight neck muscles of 15 subjects for C1 to C7 intervertebral levels (see text for details).

Muscle Name	DSC
Left sternocleidomastoid	0.85 ± 0.0284
Right sternocleidomastoid	0.85 ± 0.0141
Left obliquus capitus inferior	0.89 ± 0.051
Right obliquus capitus inferior	0.85 ± 0.0141
Left semispinalis capitis	0.86 ± 0.03
Right semispinalis capitis	0.88 ± 0.0245
Left splenius capitis	0.82 ± 0.0224
Right splenius capitis	0.84 ± 0.0173
Overall mean	0.85 ± 0.022

studies in the literature of segmenting muscles other than neck muscles, they used images with different properties and modalities. Table 3.5 shows a comparison of

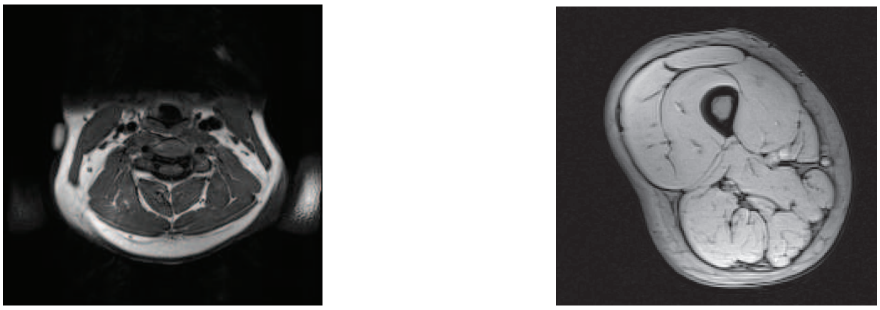

(a) (b)

Figure 3.6: Comparison of: (a) data used by proposed method; and (b) data used by Baudin *et al.* [4].

the proposed method's result and those from other recently proposed muscle segmentation methods. Although it is difficult to draw any conclusions based on the information in this table since the data sets used were totally different in respect of the muscle positions in the body, imaging parameters and numbers of patients and modalities, it can be seen that proposed method performed excellently in terms of a muscle segmentation paradigm. Although Baudin *et al.* [4] obtained slightly higher DSC values than proposed method for thigh muscle segmentation, they exploited a 3-point Dixon MRI sequence with the motivation of clarifying inter-muscular boundaries whereas data used by the proposed method suffered from intensity inhomogeneity as well as false boundary problems (Fig. 3.6). Andrews *et al.* [22] and Ibragimov *et al.* [200] also obtained good DSCs in thigh and tongue muscle segmentations but the former method was weak in terms of capturing pose variabilities and the latter used super-resolution MR images to implement its process.

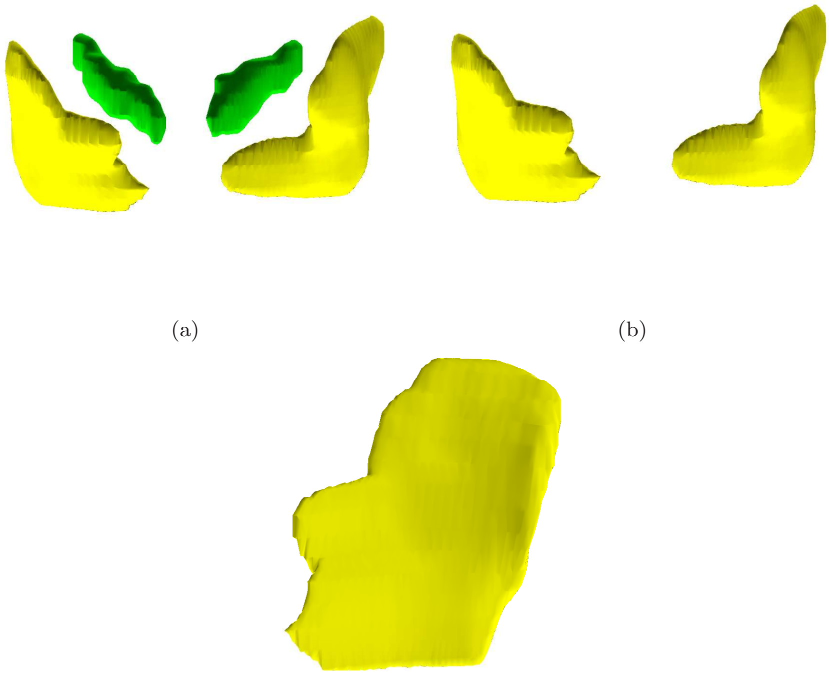

(a) (b)

(c)

Figure 3.7: Illustration of adroitness of the GUI, whereby each muscle observed separately using zoom in, zoom out, 3D rotation and panning tools for 3D views of: (a) obliquus capitus inferior and splenius capitis muscles; (b) splenius capitis muscles; and (c) one splenius capitis muscle.

3.4 Discussion

3.4.1 Shape Analysis

As a shape analysis of segmented structures is a significant part of disease diagnosis in clinical practice, the GUI developed in this work for this purpose is another substantial contribution. As, by using its zoom in, zoom out, 3D rotation and panning tools, a physician can observe the segmented muscles individually in 3D, in a group or all together. He/she can precisely locate abnormalities of the muscles affected by a WAD by careful observing of the segmented muscles in 3D. The Figure. 3.7 shows the above notion of the GUI.

Table 3.5: Comparison of mean DSC values of proposed and other methods for muscle segmentation.

Method	Muscle Name	DSC	No. of Patients
Proposed method	Neck	0.85 ± 0.02	7 healthy, 8 unhealthy
Andrews *et al.* [22]	Thigh	0.81 ± 0.074	30 healthy, 10 unhealthy
Ibragimov *et al.* [200]	Tongue	0.81	10 healthy
Gubern *et al.* [203]	Pectoral	0.74	27
Essafi *et al.* [197]	Calf	0.55	20 healthy, 5 unhealthy
Wang *et al.* [199]	Canine leg	0.78	45
Baudin *et al.* [4]	Thigh	0.86 ± 0.07	14 healthy

The cervical muscles of WAD patients undergo atrophy and hypertrophy with differential changes in the C1 to C7 intervertebral levels [13]. Thus, by observing the muscles shapes using the GUI, MRI volumes from WAD patients and healthy individuals can be differentiated by medical experts to determine the levels of compositional change in muscles. Of the 7 healthy and 8 unhealthy MRI volumes that formed our data set, the medical experts who provided us with the training volumes identified 6 healthy and 5 unhealthy ones. Although this is statistically insignificant due to the small data set, it can provide an almost exact patient classification.

3.4.2 Adroitness of Segmentation

As previously stated, the composition of neck muscles undergoes atrophy and hypertrophy due to WAD [13], with the reason for hypertrophy possibly being fat infiltrating into the muscles which is considered a pathological component of WAD and the most substantial issue for medical intervention. The proposed method can segment normal neck muscles as well as those with morphological changes because it uses a discrete cosines-based elastic registration, the deformation of which depends on the coordinate mesh grid, gradients and similarity measure. It can also handle pose variability among patients because of its use of affine and elastic registrations which can correct rotation and shearing mismatches between a reference and floating image volumes.

3.4.3 System Abridgement

The main motivation for this work was to achieve automatic segmentation with high accuracy and produce the consistent segmentation output required to deal with many patient analyses. Although high segmentation accuracy is a significant factor for proper medical intervention, the proposed method is compromised in respect of computational time. Although it could operate fully automatically without any human support, it took approximately 42 ± 3 minutes per volume using a HP z230 tower workstation with an Intel(R) Core(TM) i7-4770 CPU, 3.40 GHz processor and 4 GB of RAM running the Windows 7 SP1 operating system, and un-optimized MATLAB code. In contrast, Baudin *et al.* [4] took 13 ± 1.2 minutes per volume, Ibragimov *et al.* [200] an average of 6.6 minutes using C++ with code parallelization on a personal computer with an Intel Core i7 CPU, 2.8 GHz processor and 8 GB of memory, Andrews *et al.* [22] 50 ± 4.3 minutes using 2 Quad Core Intel Xeon 2.33 GHz CPUs and Zhuang *et al.* [213] 2-4 hours per volume. However, a direct comparison of these computational times is not reasonable due to the different programming languages and machine configurations used.

3.5 Conclusion

This chapter presents the first work on neck muscle segmentation in which neck muscles were automatically segmented using affine- and discrete cosine-based elastic registration as well as knowledge-based grouping adaptation techniques. The affine registration employed a new similarity measure-based Gauss-Newton optimization technique which exploited the SCVPVI as the similarity measure. The elastic registration engaged discrete cosines as the basis function which was used in a novel framework that could neutralize higher-order shape mismatches. Furthermore, the new knowledge-based grouping adaptation technique could work in a region with muscles in close proximity which is very difficult using any deformable model. In addition, a clinically friendly GUI is developed which could be easily used by physicians to conduct manual delineation as well as segmented volumes analysis for disease diagnoses.

Chapter 4

Multiple-object Parametric Deformable Model for Segmentation of Neck Muscles using Prior Information

This chapter discusses improvements in the segmentation results produced by the image registration process. It presents a novel parametric deformable model-based segmentation method for multiple objects in a very compact space as is very common in the anatomy of neck muscles. The algorithm can work properly in noisy images and undesired objects with similar intensity as it resides close to the desired object where level set-based geometric deformable models cannot work. A novel Gaussian potential energy distribution using the principal component analysis technique is used in the proposed scheme. This work also incorporates new stopping criteria for the vertices and a new technique for removing overlaps among the nearest contours. In addition, the deformation of the model considers the coupling effects among the contours of a group. The remainder of this chapter is arranged as follows: Section 4.1 presents a relevant literature review of multiple-object deformation models which provides inspiration for planning our multiple-object parametric deformable (MOPD) model; 4.2 the proposed methodology; 4.3 the experimental results and analysis; 4.4 a general discussion; and 4.5 conclusion.

4.1 Introduction

Medical image segmentation has become an inevitable task for systems designed to diagnose many human afflictions. As human organs remain as a group in a compact space in different parts of the human body, the task of multiple-object segmentation has significant importance for medical image analysis. However, this is quite difficult compared with single-object segmentation because there are some complications involved in segmenting an object. Firstly, its boundary becomes heterogeneous if it remains with other objects in a compact space [5]. Secondly, its boundary becomes obscure due to the partial volume effect which occurs in the low-resolution medical images normally obtained from medical imaging devices compared with those from a typical camera. As a result, when multiple objects meet, it is difficult to detect their boundaries. Finally, automatic segmentation results produce overlaps among the closest objects and gaps between two close-fitting ones because the gradient force of an object or boundary edge drags the adjacent object's evolutionary vertices.

Moreover, another complication of multiple-object segmentation is that it depends on the compositions of the objects. In particular, those of brain organs are such that, when scanning is performed using a medical scanning device, the resultant images have no boundary diffusion or clear boundary separation among the organs. In other words, the compositions of brain organs are different from each other whereas those of muscles are similar to each other. Therefore, imaging devices provide images of muscle regions that have poor image contrast and boundary diffusion. As a consequence, it becomes difficult to detect the boundaries of neighboring muscles, as shown in Figure 4.1. It can be seen that the cerebellar lobes, lobules and corpus medullare are clearly separate from each other whereas

(a) (b)

Figure 4.1: Comparison of anatomical complexities of: (a) neck; and (b) brain cerebellum [5].

the muscles boundaries are not.

Furthermore, as the anatomy of neck muscles is more complex than that of other muscles in the human body due to these muscles' compactness, high numbers and small sizes, segmenting multiple neck muscles is a very challenging task. Anatomical pictures of thigh, leg, hip and neck muscles are shown in Figure 3.1.

Deformable models are used extensively in medical image segmentation. The two types in the literature depend on whether contours are represented explicitly or implicitly, with the former called a parametric deformable model and the latter a geometric one. Geometric models are implemented using the curve evolution theory and level-set method. In the literature, several level-set frameworks for multiple-object segmentation have been proposed [5, 23, 99, 116, 145, 146, 148–153, 217–222]. Geometric deformable models have some advantages over parametric ones. Firstly, level-set-based methods have the flexibility to handle topological changes whereas parametric methods do not unless a complicated process is employed. Secondly, if some close parametric contours deform independently, overlaps are created among the contours but can be avoided if a proper stopping criterion and small deformation step are used in the algorithm. However, although several disjoint objects can be presented by one level-set function, such methods can still produce overlaps due to interactions of some definite objects. Finally, objects which are absent in the initial frame can be automatically detected in an image sequence using level-set methods.

In application situations, level-set-based methods also have some disadvantages compared with parametric ones. Firstly, as they yield spurious connected components in gloomy and noise-affected images [116], they cannot work in a neck muscle paradigm because neck muscles are structurally similar to each other and almost touching. Also, intra-fat and background clutter have similar intensities and textures to muscles in neck magnetic resonance (MR) images and the boundaries of neck muscles are not clear due to the low resolution of MR imaging (MRI) and noise. These scenarios are shown in Figure 1.1.

Another important limitation of a level-set method is its suboptimal segmentation of objects with distinct features due to its inability to tune [99, 116, 218, 219] whereas objects with distinct features and similar disjoint objects can be tuned separately in a parametric deformable model. However, this problem can be overcome by using multiple level-set functions [145, 146, 150, 219, 221] although, as zero level sets intersect each other when multiple ones evolve differently, such a level set yields overlaps during separate adaptations. Vese *et al.* in [150] proposed a multi-phase level-set framework employing the Mumford and Shah model for image segmentation which exploited $log_2(N)$ level-set functions for N phases which provided good parcellation of objects. Nevertheless, the topological constraints among objects in a phase cannot be achieved because each phase contains objects with similar image characteristics.

Furthermore, other multiple level-set methods [145, 146, 219] engaged N level-set functions for N classes of objects by enacting extra constraints to confirm the partition of attributes which could address the obstacles of touching non-occluding objects with similar image characteristics or not similar characteristics. Recently, Bogovic *et al.* [5] propounded a multiple-object geometric deformable model using fixed level-set functions with existing speeds which obtained good results in respect of no overlaps or gaps but their method is not suitable for practical application due to its segmentation output being region-wise with the objects not separated. They also used approximate object boundaries with approximate signed distance functions which are very different from real objects' boundaries. However, the computational complexity of multiple level-set methods is greater than that of parametric techniques as they are required to update the level-set functions in every iteration over the whole image domain whereas parametric methods update only the positions of the vertices of a contour. Although some proposed level-set methods reduce computational complexity by using a narrow band and fast marching [222, 223] or additive operator splitting [224], they are normally many times slower than parametric methods.

Finally, parametric methods support more amenable user interactions than geometric ones as the latter are required to extract the contour from a level-set function. Therefore, a parametric method is a more justifiable approach for images with noise, background clutter and/or similar touching objects when many images need to be processed in a moderate amount of time. Zimmer and Olivo-Marin ([225]) proposed a coupled parametric active contours method by combining the properties of level-set schemes with the parametric process. However, it cannot exactly determine the interfaces between objects and, sometimes, one contour fails while another encloses both objects. Therefore, a MOPD model is proposed for segmenting neck muscles in this chapter.

In this chapter, a MOPD model is presented for a real-time application with a novel Gaussian potential force which uses the major axis of an object to generate a conditional potential force. The proposed method incorporates an overlap removal technique and coupling in the contours' deformations, which prevents any overlap occurring, using a small deformation step and stopping criterion. Also, an intelligent stopping criterion and resampling technique are incorporated for smooth deformation when the discrepancy between a deformable contour and object boundary is very small. Furthermore, this method can segment any number of objects without causing any major complexity in the algorithm. Moreover, it can preserve the anatomy's topology using the conditional Gaussian potential force and prior anatomical knowledge.

The MOPD model can resolve the traditional parametric limitation of topological adaptation through its conditional Gaussian potential energy distribution function. If splitting or merging occurs in an object, the potential energy is generated in such a way that the initial model is dragged to the desired object boundary without any re-parameterization. The proposed method is also used in a situation in which there is little difference between an object and the model; for example, exploited in an affine and elastic motion model-based registration framework in which the model's boundaries are close to those of the objects boundaries and applied on data of almost consistent neck muscles.

4.2 Proposed Method

A parametric deformable model is used for neck muscle segmentation in this proposed method. The initial contour model is represented explicitly and, in particular, consists of a number of vertices connected by straight lines called edges.

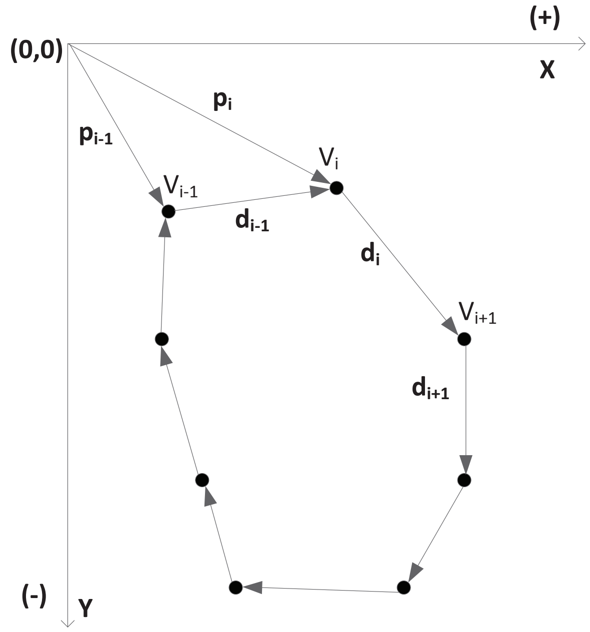

Figure 4.2: Parametric deformable model.

Figure 4.2 shows the basic construction of the model, where the vertices are represented as V_i and the edge between V_i and $V_i + 1$ as $\mathbf{d_i}$. The model is considered as closed and it is assumed that the position of a vertex is a vector ($\mathbf{p_i}$) and the coordinate system is Cartesian. The values of the Y axes of the vertices are multiplied by a negative sign with 0.5 subtracted from X and Y values to revert to a Cartesian system from an intrinsically coordinate one. The deformation of the model is achieved by employing three forces acting on each of its vertices, with their derivations discussed in the next subsection.

4.2.1 Calculations of Forces

One internal and two external driving forces are calculated for each vertex of a contour in the deformation process, with each internal force derived from the local curvatures of the contour model which minimize the local contour curvature and smooth the model. The external forces, the Gaussian potential and dynamic distance, drag the contour model towards the object boundary and are calculated over the image domain.

4.2.1.1 Internal Forces

The internal forces are calculated from the local contour curvatures at each vertex, with the motive of keeping the regularity of the model by reducing its overall local curvature. As the local curvature at a vertex is defined as the difference between the directions of the two edges connected at that vertex [226], that at vertex V_i ($\mathbf{c_i}$) can be written as

$$\mathbf{c_i} = \hat{\mathbf{d_i}} - \widehat{\mathbf{d_{i-1}}} \tag{4.1}$$

where $\hat{\mathbf{d_i}}$ is the unit vector of edge $\mathbf{d_i}$.

This local curvature has a certain length which depends on only the angle between the two edges and a direction. In order to avoid the problems of the contour shrinking and vertices clustering, the local tangential and radial directions are used at each vertex to calculate the internal and external forces. The local tangential unit vector ($\hat{\mathbf{t_i}}$) at vertex V_i is defined as [226]

$$\hat{\mathbf{t_i}} = \frac{\hat{\mathbf{d_i}} + \widehat{\mathbf{d_{i+1}}}}{\|\hat{\mathbf{d_i}} + \widehat{\mathbf{d_{i+1}}}\|}. \tag{4.2}$$

The local radial unit vector ($\hat{\mathbf{r_i}}$) at vertex V_i is formed by rotating $\hat{\mathbf{t_i}}$ 90 degrees counter-clockwise as

$$\hat{\mathbf{r_i}} = \begin{bmatrix} 0 & 1 \\ -1 & 0 \end{bmatrix} \hat{\mathbf{t_i}}. \tag{4.3}$$

The local curvature vector points along the local radial unit direction in either the same or opposite direction and its length can be negative or positive, as expressed by

$$\mathbf{c_i} = (\mathbf{c_i}.\hat{\mathbf{r}}_\mathbf{i})\hat{\mathbf{r}}_\mathbf{i} \tag{4.4}$$

where $\mathbf{c_i}.\hat{\mathbf{r}}_\mathbf{i}$ represents a dot product.

The internal forces should be derived from the local curvature vectors so that shrinking of the contour does not occur. Therefore, the following two criteria must be satisfied: firstly, that the internal force ($\mathbf{f_{in,i}}$) at vertex V_i acts along the local curvature direction which is derived by modifying the length of the local curvature vector ($\mathbf{c_i}$); and, secondly, the local curvature must be minimized in such a way that the constant curvature of the contour is unaffected by setting the lengths of the internal force vectors to zero for those portions of the contour. These two conditions can be met if the lengths ($f_{in,i}$) of the internal force vectors are derived as

$$f_{in,i} = (\mathbf{c_i}.\hat{\mathbf{r}}_\mathbf{i}) \otimes k_i \tag{4.5}$$

where k_i is a discrete filter and $\otimes$ a discrete convolution.

The first condition can be fulfilled as

$$\mathbf{f_{in,i}} = f_{in,i}\hat{\mathbf{r}}_\mathbf{i}. \tag{4.6}$$

The second condition can be satisfied by selecting a proper asymmetric discrete filter. The discrete filter was used in the experiment

$$k_i = \{0, 0, 0, 0, 0, 0, -0.5, 1, -0.5, 0, 0, 0, 0, 0, 0\} \tag{4.7}$$

where the value 1 corresponds to vertex V_i.

4.2.1.2 Application Specific Gaussian Potential Forces

The external potential energy distribution plays a significant role in providing driving forces for contour deformation, with the desired deformation of a model depending mainly on it being appropriate. Traditional gradient-based energy distribution cannot provide the forces required for good deformation because it has two limitations in terms of the edge energy. Firstly, it uses one directional horizontal and vertical gradient over the whole image. As a result, the gradient values of an object's boundaries are different on opposite sides that is, on the left and right sides, and on the top and bottom. Secondly, when multiple objects remain close to each other, the vertices are attracted by the nearest object's boundary gradient, affixed by its boundaries and overlapping. Regardless of considering the gradient magnitude as an energy distribution, as the second limitation still exists, a type of energy distribution is required where the gradients are calculated from the centre point of an object to all directions so that the gradients of the nearest object's boundaries become opposite to those of the objects considered for segmentation.

In this neck muscle segmentation project, a novel conditional Gaussian potential energy distribution (CGPED) is developed using the major axis and centroid of an object so that the aforementioned problems of a traditional gradient magnitude energy distribution can be overcome. The CGPED provides the force desired for good segmentation of a single object as well as multiple objects which remain close to each other. It prevents a contour being attracted to another object's boundary and always drags it towards the object considered for segmentation. Therefore, this technique can avoid the overlap problem as well as preserve the object's topology. An energy distribution is generated separately for each muscle using a multi-scale standard deviation of the Gaussian function to enhance the range of attraction.

In the CGPED process, an interim Gaussian gradient function used for a whole image, which is subsequently manipulated to obtain our desired CGPED, is given by

$$P(x, y) = \nabla(G_\sigma(x, y) * I(x, y)) \tag{4.8}$$

where $G_\sigma(x, y)$ is a 2D Gaussian function with a standard deviation (σ), ∇ the gradient operator and $*$ the 2D image convolution operator.

To enhance the range of attraction, the changing schedule of the standard deviation of the Gaussian filter takes the form

$$\sigma' = \sigma/3 \tag{4.9}$$

where σ' is the new standard deviation of the current iteration.

The final CGPED derivation from the interim function depends on the object's centroid, angle of its major axis and equation of a straight line passing through a point, which is considered to be the centroid of the object, and is

$$y = mx + c \tag{4.10}$$

where m is the slope and c the intercept of the line.

The intercept of the line is calculated from the centroid and angle of the major axis of the object, with the final CGPED is calculated as

$$CP(x,y) = \begin{cases} \text{if } 15 \leq \theta < 90 \begin{cases} dx & \text{if } r_i > y \\ -dx & \text{if } r_i < y \end{cases} \\ \text{if } -90 < \theta \leq -15 \begin{cases} -dx & \text{if } r_i > y \\ dx & \text{if } r_i < y \end{cases} \\ \text{if } -15 < \theta < 15 \begin{cases} dy & \text{if } r_i > y \\ -dy & \text{if } r_i < y \end{cases} \\ \begin{bmatrix} A & B \end{bmatrix} + \begin{bmatrix} C \\ D \end{bmatrix} & \text{if } \theta = 90 \parallel -90 \end{cases} \tag{4.11}$$

where $CP(x, y)$ is the desired CGPED, θ the angle of the major axis of the object considered for segmentation, ri the row index, dx and dy the horizontal and vertical gradient fields of the interim distribution $P(x, y)$, $A = -1 * dx(:, 1 : CNT(1))$, $B = dx(:, CNT(1) + 1 : M)$, $C = -1 * dy(1 : CNT(2), :)$, $D = dy(CNT(2) + 1 : N, :)$ respectively, M and N the horizontal and vertical dimensions of the image respectively, and CNT the centroid of the object.

In equation 4.11, only the horizontal gradient field is considered in the first and second cases for the desired energy distribution so that the gradient values at the boundary of the object are homogeneous. On the other hand, if both the horizontal and vertical gradient fields are used for objects orientated as in those

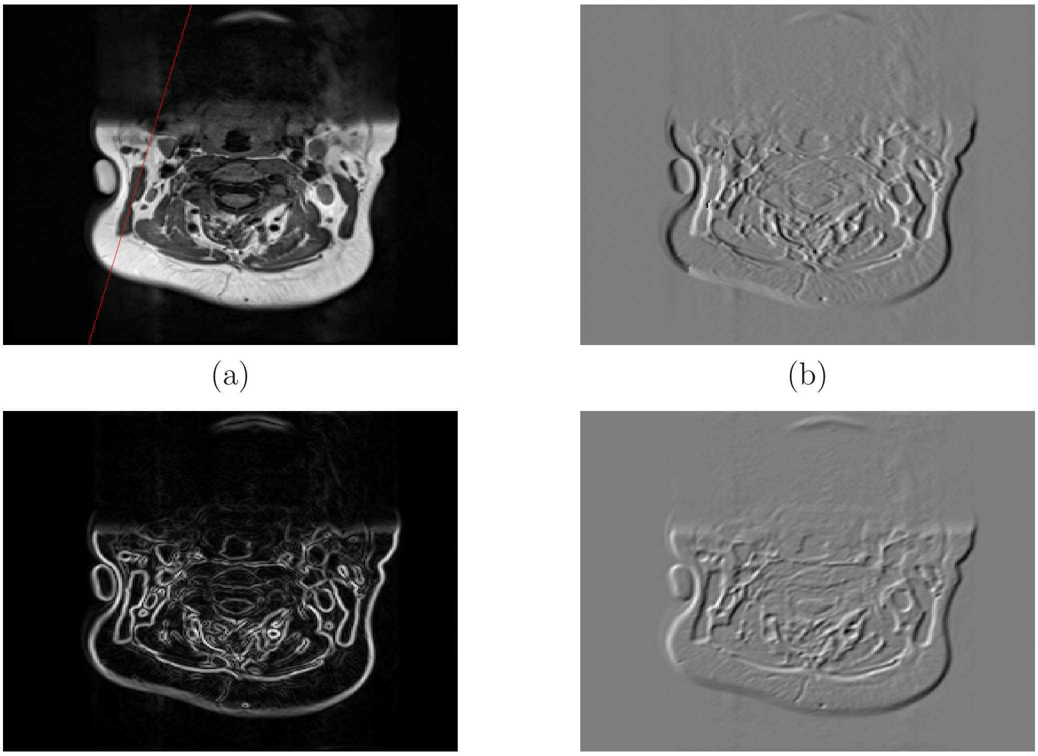

(a) (b)

(b) (b)

Figure 4.3: Comparison of energy distributions: (a) original image with major axis; (b) CGPED; (c) gradient magnitude; and (d) gradient only.

two cases, the boundary gradient values are heterogeneous. Another two similar cases are selected to obtain a uniform distribution of the gradient values around the boundary of the object.

A comparison of the energy distributions of the CGPED, gradient magnitude and gradient only are shown in Fig 4.3. It can be seen that CGPED provides an almost uniform distribution of the gradient values and a good distribution for multiple-object segmentation because the gradient values of the surrounding objects are opposite to those of the desired one.

However, the CGPED model has two limitations which will be removed in future work. Firstly, it cannot provide uniform values at the two end regions due to the use of only one gradient field; this can be overcome by using both the gradient field and major axis. Secondly, if the centroid of an object resides outside the object, this method cannot provide uniform values for some parts of this object.

The CGPED process is applied separately for each muscle to obtain separate energy distributions which are then inverted to generate energy valleys at the object's boundaries because the deformation process pulls the vertices into local minima, and is used to calculate both the Gaussian potential and dynamic distance forces.

The force field can be derived from the energy distribution (CP) as

$$\mathbf{f_p} = -\nabla CP \tag{4.12}$$

The force $\mathbf{f_{p,V_i}}$ acting on vertex V_i is calculated from the force field using 2D interpolation. Although it has two components, only its radial one is used for vertex deformation because its tangential one causes a clustering problem in the model which is undesirable. The radial component can be written as

$$\mathbf{f_{p,r_i}} = (\mathbf{f_{p,V_i}}.\mathbf{\hat{r}_i})\mathbf{\hat{r}_i} \tag{4.13}$$

4.2.1.3 Dynamic Distance Forces

The model can be attracted from a fairly long distance using the force that depends on the signed distance between a vertex and an object's boundary point along the model's normal direction, with the CGPED also used to calculate the dynamic distance forces for selecting the desired boundary point. The normal direction is chosen as that of either the local curvature or reverse local curvature; in particular, the boundary point is searched along the local curvature direction first and then the reverse local curvature direction, with the distance re-calculated in each deformation iteration. If a vertex is at the boundary of the object, this force is zero, a condition that is checked before starting the distance calculation. It is also zero when the searching index exceeds the image's boundary and crosses the boundary of the nearest object, with a threshold for finding the boundary point from the CGPED selected.

The dynamic distance force for vertex V_i is [76]

$$\mathbf{f_{d,i}}(V_i) = \frac{D(V_i)}{D_{max}}\mathbf{N}(V_i) \tag{4.14}$$

where V_i is the vertex, $D(V_i)$ the computed signed distance, D_{max} the specified distance threshold and $\mathbf{N}(V_i)$ the unit normal.

4.2.2 Deformation

The deformation of a vertex depends on the lengths and directions of the three aforementioned forces which act together for deformation while the coupling effect is maintained among the models which deform simultaneously and stay close to each other. This simultaneous deformation is performed by maintaining seriality among the models in the same deformation iteration, in particular, by considering model-1 first, model-2 second, model-3 third and then model-1 again. When the deformation of one model is complete, it is ensured that its vertices cannot penetrate the neighbouring ones by using the special overlap removal technique described in 4.2.2.1.

The total force acting on a vertex (V_i) is

$$\mathbf{f_i} = w_{in}\mathbf{f_{in,i}} + w_p\mathbf{f_{p,i}} + w_d\mathbf{f_{d,i}} \tag{4.15}$$

where w_{in} w_p and w_d are the internal, potential and distance force weighting factors respectively. The values of these factors depend on the modality of the image considered and the application, which is modifiable by users and set as different for each model since each model's surrounding conditions are exclusive. The schedule for changing the internal and potential force weights in a multi-scale technique is

$$w' = w/10000 \tag{4.16}$$

where w' denotes new weights. The schedule for changing the distance force weight is

$$w'_d = w_d/3 \tag{4.17}$$

The deformation of a vertex may oscillate between two local minima which can be stopped by adding a damping force to the total force as

$$\mathbf{f_{damp,i}} = w_{damp}\mathbf{v_i} \tag{4.18}$$

where $\mathbf{v_i}$ is the velocity of the vertex and w_{damp} a negative value.

As the resultant force causes acceleration and velocity, the vertex moves in the specified direction and its dynamic situation can be described by

$$\mathbf{a_i}(t + \Delta t) = \frac{1}{m_i}\mathbf{f_i}(t + \Delta t) \tag{4.19}$$

$$\mathbf{v_i}(t + \Delta t) = \mathbf{v_i}(t) + \mathbf{a_i}(t + \Delta t)\Delta t \tag{4.20}$$

$$\mathbf{p_i}(t + \Delta t) = \mathbf{p_i}(t) + \mathbf{v_i}(t + \Delta t)\Delta t \tag{4.21}$$

where m_i in (4.19) represents the mass of a vertex, t the time index and Δt the incremental time, with the values of the masses of all the vertices considered equal in order to give them the same priority in the deformation process. $\mathbf{f_i}(t+\Delta t)$ in (4.19) is derived from equations (4.15) and (4.18).

In this work, a new stopping criterion is employed for the vertices in the deformation process, an intelligent one for smooth deformation whereby the discrepancy between a deformable contour and object boundary is very small. In this situation, as the distance force cannot work properly because the threshold criterion is not satisfied, the threshold is selected by considering all sides of the object as well as its intensity leaking with another object or background. Therefore, a compromise is made regarding the threshold value of an object, that is, it is lower than the boundary one in some positions and higher in others. This situation usually occurs when a deformable vertex gradually moves closer to the boundary from a long distance where only the internal and potential forces are engaged in the deformation process because they do not depend on the threshold. In addition, the threshold selection procedure faces difficulty due to the low standard deviation (SD) of the Gaussian filter, which is required to capture smooth details of an image, that leads to a very large difference between the gradient values of two very close distances even in the next pixels. The situation can be observed in Fig. 4.4 in which the object has four leaking boundaries with its other sides wide edges. The deformation process ceases when the velocity and acceleration of all the vertices become zero.

4.2.2.1 Overlap Removal Technique

The complete parcellation of objects in medical image segmentation is an important activity due to the difficulty encountered when organs are very close to each other and even manual delineation is confusing. In addition, medical images suffer from the partial volume effect due to the low resolution of a medical imaging system. Therefore, the vertices are attracted by the boundaries of the nearest

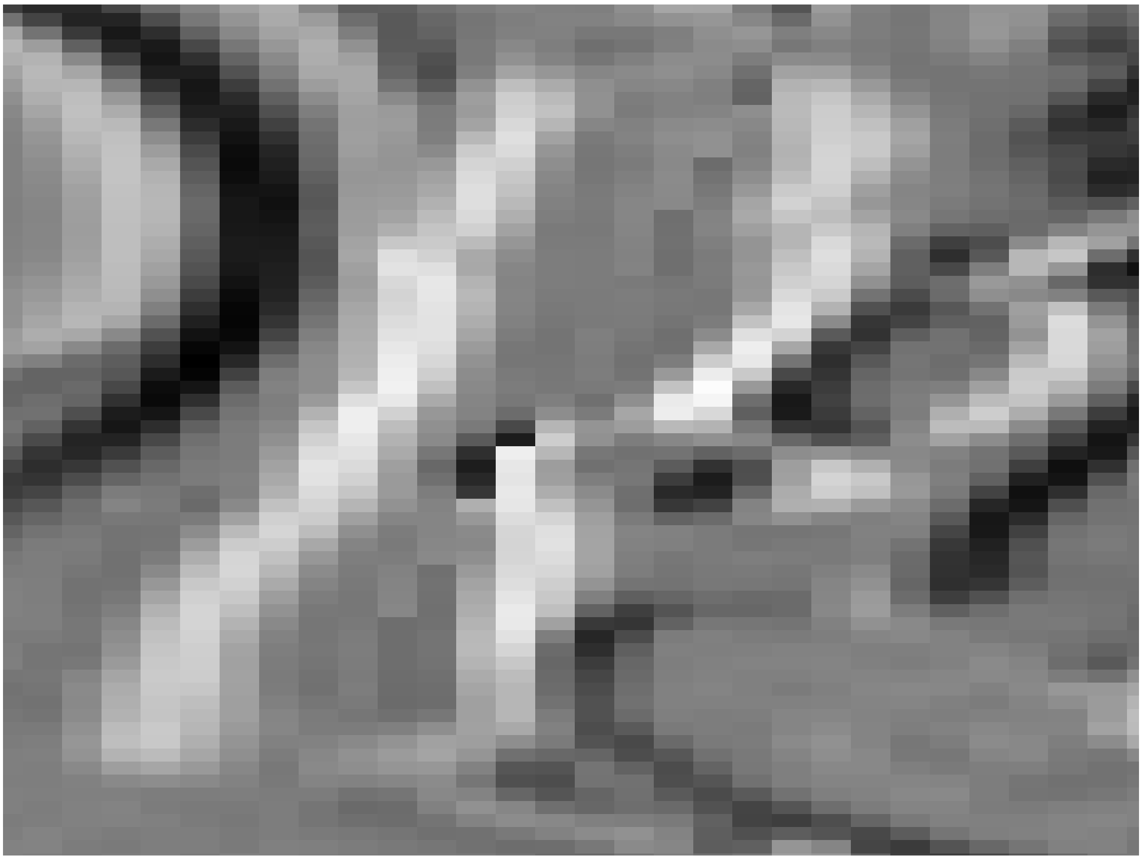

Figure 4.4: Selection of Threshold.

objects, which develop overlaps among the objects. Furthermore, as the deformation of a vertex is independent of its position because the forces are generated and applied each time irrespective of that position, the vertices may cross other objects boundaries.

Therefore, the most substantial issue in a segmentation process is to have a technique for avoiding overlaps or removing them if they occur. In this segmentation algorithm, this is incorporated through calculating the distance force, but not considering the internal and potential forces, which avoids the regions of the nearest objects models during boundary-point searching while the removal technique eradicates already existing overlaps.

Initially, the overlap removal technique checks whether the vertices of an object are situated inside the regions of any surrounding objects' models. If one is, it is moved along the centroid direction of the object, which is considered to be segmented, until it exits from that models region to remove the overlap.

4.2.2.2 Resampling

The resolution of a model's vertices plays an important role in model deformation. If it is low, a deformation yields undesirable results in terms of the model's shape; that is, it cannot represent an object's boundary smoothly which is important for objects with small, non-regular and rough boundaries, such as neck muscles and other human organs. On the other hand, if the resolution is high, the computational complexity of the segmentation algorithm increases significantly. Moreover, the potential force passes through the large edge without having any impact on changing the model's shape. Therefore, a suitable vertex resolution is an important factor in segmentation.

In this resampling implementation, the vertices of a model are initially resampled using 1D interpolation to reduce the user effort required to create the model. The main resampling technique uses one checking process for the whole contour to determine whether each edge segment is greater than the user-defined maximum length (L_{max}) or less than the minimum one (L_{min}). If an edge segment is greater than L_{max}, a new vertex is inserted between the two vertices of that edge with a zero velocity. In contrast, if the edge is less than L_{min}, the second vertex of the edge is removed from the contour. The values of L_{max} and L_{min} are selected by maintaining the condition $L_{max} > 2L_{min}$ so that a resampling oscillation does not occur in the resampling process. In the deformation process, firstly, resampling is performed, then the overlap removal technique is implemented and, finally, calculations of the forces and movements of the vertices are committed to obtain the contour's evolution.

4.3 Experimental Results and Analysis

4.3.1 Experimental Setup

4.3.1.1 Data Set

In the experiments, MOPD was used in registration and mid-scan-based methods for neck muscle segmentation using a data set containing clinical MR images, which is described in 3.3.1.4 and 3.3.1.2.

4.3.1.2 Selection of Parameters

The kernel size of the Gaussian filter was 20 for the generation of Gaussian potential energy, with the sigmas in the two scales of 0.06 and 0.03 chosen to be very low to capture the fine details of the energy distribution. The weights of the three forces and their thresholds and the distance thresholds of the distance force were selected separately in order to implement object-specific parameters for considering different ambient conditions. In this work, the bilateral sternocleidomastoid, semispinalis capitis and splenius capitis neck muscles was segmented with their initial parameters ($w_{in} = 1000, w_p = 20, w_d = 5, D_{max} = 3$, and $threshold = 790$), ($w_{in} = 100, w_p = 0.05, w_d = 2, D_{max} = 3$, and $threshold = 80$), and ($w_{in} = 100, w_p = 0.05, w_d = 2, D_{max} = 3$, and $threshold = 80$) respectively. The reasons for these selections were that the sternocleidomastoid muscles have good contrast, texture and less background clutter than the semispinalis capitis and splenius capitis ones which also reside very close to each other. The output

Table 4.1: Parameters Table

Muscle Name	w_{in}	w_p	w_d	D_{max}	Threshold
Sternocleidomastoid	1000	20	5	3	790
semispinalis capitis	100	0.05	2	3	80
splenius capitis	100	0.05	2	3	80

sensitivity of this method mainly depends on distance force which is predominantly controlled by threshold whereas a certain value of threshold yields good segmentation results and beyond the value gives also good results and less than the value results the model moving slowly toward the actual boundary. The damping weight was -0.5 in model deformation while all the vertices were considered to have masses of 1. In this experiment, only 15 deformation iterations were used which gave good segmentation results and, in order to avoid oscillations in the resampling process, 2.8 and 1 were used as the maximum and minimum lengths respectively. The parameters of this method are presented in Table 4.1.

4.3.2 Performance Analysis

The MOPD method was implemented on real clinical MR images to segment neck muscles in order to understand their shapes and sizes as required to determine the reasons for WAD. The method used only 15 iterations to obtain a final deformation and could segment any number of objects in an image without increasing its complexity.

The deformation of 6 neck muscles from one patient's MR volume is presented in Figure 4.5. It can be seen that there is no overlap between the semispinalis capitis and splenius capitis muscles even though they are very close to each other, they are similar in terms of contrast, intensity and texture, and there is no fissure

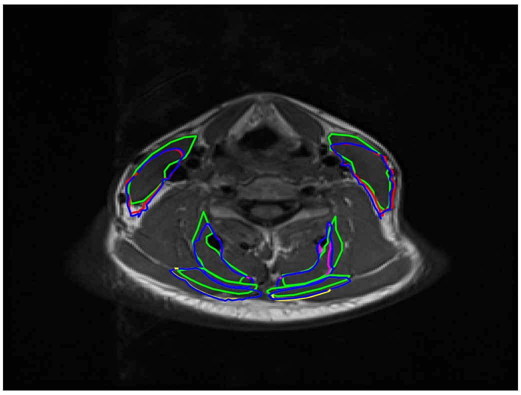

(a)

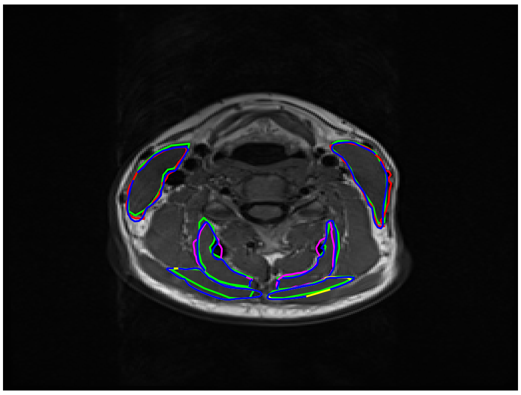

(b)

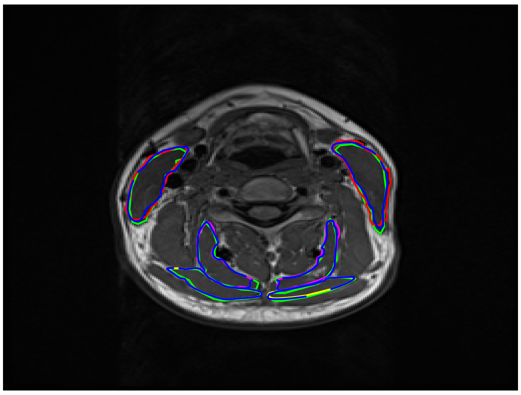

(b)

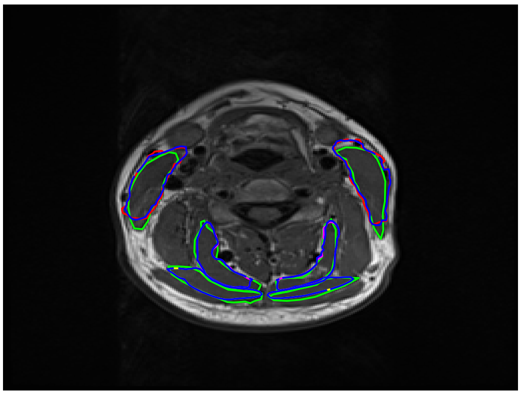

(b)

Figure 4.5: Deformation results for neck muscles using MOPD method (green curves represent ground truths of muscles, blue curves initial models, and red, magenta and yellow final deformed curves for sternocleidomastoid, semispinalis capitis and splenius capitis muscles respectively).

in any interface between them. The deformed contour edges fairly well match the ground truths of the muscles, except those nearest to the two ends of each muscle. The reason for this mismatch is that the potential energy distribution of a muscle provided low gradient values at its two ends. In this situation, level-set based geometric deformable models would produce false connected components since the muscles almost touch each other and there would be other background clutter with a similar intensity to those of the muscles. Moreover, gaps exist inside a geometric deformable model during deformation, which are not present in a parametric one. Bogovic *et al.* ([5]) achieved excellent results for the segmentation of multiple objects in a cerebellum application using a geometric deformable model with a fixed level-set function. They applied their method on sub-regions, in particular, segmenting cerebellum lobules as a group rather than individually whereas MOPD segmented neck muscles individually without any overlap. Zimmer and Olivo-Marin ([225]) obtained good results for the segmentation of biological cells from video-microscopy using a coupled parametric model. However, their method could not trace the interface between touching objects, which this method clearly can.

4.4 Discussion

The most substantial issue in segmenting multiple objects from medical images is completely parcellating the organs without any gaps inside. However, most multiple-object segmentation methods suffer from the problem of overlapping among the objects. Also, some level-set-based ones suffer the problem of gaps inside objects, which some methods remedy through using 'gap-filling' terms. In this parametric model, a novel overlap removal technique was used which removes existing overlaps as well as tries to prevent others occurring without using any 'gap-filling' terms. The segmentation output did not contain any gaps or overlap as the contour boundary was directly evolved. However, an overlapped vertex is moved in the approximately centroid direction which may have created criss-crosses among the vertices of a single contour for some objects with particular shapes. In addition, the unique energy distribution in the CGPED method assisted in overlap prevention.

Preserving the topological relationship is another vital concern when segmenting multiple objects from medical images. Using our MOPD method, this requirement was accomplished for the majority of an object's edges through the CGPED but not for a very few because the CGPED could not provide uniform values in the vicinity of the ends of an object. The MOPD method does not require any re-parameterization in cases of topological changes or large differences between an initial contour and an object because the CGPED provides such a distribution that the vertices are attracted from long distances using the potential and distance forces. These two cases, which would normally be considered abridgments of parametric deformable models, were resolved using this MOPD method.

Although level-set based geometric deformable models work well for non-touching objects with clear and non-noisy images, they cannot work on noisy, images with touching objects or objects in compact spaces. For such scenarios, these methods produce adulterated segmentation while proposed approach does not and, furthermore, they take comparatively more time than parametric deformable methods.

As the initial models obtained from atlases use a registration scheme and mid-scan based segmentation techniques, the MOPD method is a totally automatic segmentation in which the CGPED ensures its sensitivity and, in particular, drags the model's vertices from different initial models towards the original object's boundaries.

4.5 Conclusion

A multiple-object segmentation method was presented for neck muscles from real clinical MR images using a parametric deformable model, and introduced novel potential energy distribution (CGPED) and overlap removal techniques. The results demonstrated that overlaps or gaps were absent from the automatic segmentation results and, in addition, the topological relationship among the neck muscles was preserved. The CGPED overcame the traditional limitations of parametric deformable models through its unique energy distribution and, as the overlap removal technique prevented overlaps, a completely parcellated segmentation of neck muscles was provided. In this context, a stopping criterion was also incorporated, which could correct a small amount of distinction between the contour model and the original object's boundaries, and a resampling technique for vertices which confirmed the smoothness of the deformable model.

In future, the end-vicinity energy distribution problem will be eradicated by combining more techniques with the current ones.

Chapter 5

Template Contour Propagation-based Neck Muscles Segmentation

This chapter presents a contour propagation (CP)-based segmentation method using a novel multiple-object parametric deformable model (PDM) for neck muscles which uses prior anatomical spatial map information in the process to combat the inherent challenges of medical images. It requires human interaction on only the middle slice of an MR image while the rest of the process is automatic. It is more flexible than registration-based methods as it handles anatomical variabilities with low computational complexity and the experimental results show that it is capable of segmenting faster with good accuracy. The remainder of this chapter is organized as follows: Section 5.1 presents a relevant literature review of CP-based segmentation methods and the motives for designing a template CP-based neck muscles approach; 5.2 the proposed methodology; 5.3 the numerical results obtained; 5.4 a general discussion; and 5.5 conclusion.

5.1 Introduction

Medical image segmentation is typically more difficult than for non-medical images in which prior anatomical information plays an important role in combating imaging artefacts and anatomical complexities. A good segmentation algorithm should be able to achieve anatomical variability, that is, segment any individual's data. During the last few decades, registration- and deformable model-based methods have been widely used for medical image segmentation due to their incorporation of prior knowledge.

However, due to the inability of a registration process to obtain 100 percent anatomical correspondences between atlas and target images and its inherently high computational complexity, atlas-based segmentation methods have not yet been adopted in professional clinical practice. Although they use a full anatomical spatial map, they cannot completely handle anatomical variabilities. Also, deformable model-based segmentation approaches used in the clinical research domain need an initial model that can be obtained from an atlas using registration and label transformation. However, in some cases, this model could be far away from an object's boundary due to the limitations of registration and those models movement towards an object's boundary is not possible by deformable models. On the other hand, thresholding and clustering methods are not suitable for overcoming the common challenges of medical images, such as their sensitivities to noise, the initial conditions, compactness and low resolution.

In recent years, CP-based methods for segmenting the spinal cord and canal [6, 40], intervertebral disks and trachea [6], quadriceps with femur and bone marrows [8], ventricles [82, 85], heads [227] and blood vessels [228], in which deformable model-based and thresholding segmentation methods work as a principal part of the whole process, have been proposed. These methods are more reliable in terms of handling anatomical variabilities and obtaining accuracy in trade-offs with minimal user interaction than a deformable model with a registration-based technique because they do not depend on the data of other individuals. Compared with aforementioned human organs that have good contrast and low compactness in images, neck muscles contain objects with the same intensities in a compact space, as can be seen in Figure 5.1. As a result, deformable models and thresholding algorithms that can work easily for those organs cannot do so for neck muscles due to their low contrast in a compact space and background clutter. Also, the slice thickness and gap between slices are important considerations in CP-based methods; in particular, if they are small, the computational complexity of CP increases with increasing accuracy and vice versa. Seifert *et al.* [6] proposed a CP segmentation for an intervertebral disk, trachea and spinal cord from sagittal MRI using a principal component analysis (PCA) and active shape model (ASM)-based initial contour localization for deformable segmentation with a 0.11mm gap and 1.16mm slice thickness. Although they achieved good segmentation accuracy, their method may not work properly with large slice thicknesses and gaps, and also their selection of the master slice was manual. Ahmad *et al.* [8] employed a CP method for quadriceps with femur and bone marrows from axial MRI by exploiting the snake active contour in which all organs were segmented together rather than individually. Nyúl *et al.* [40] proposed a CP using seeded region-growing and an active contour for a spinal cord and canal from 3D CT images. Cohen *et al.* [82, 85] proposed a CP segmentation for a heart ventricle that employed multiple manual initial slices with active contours and balloon forces while assuming small slice-to-slice variations.

As the aforementioned algorithms only work for organs with good contrast, in this chapter, a CP-based neck muscles segmentation method with minimal user

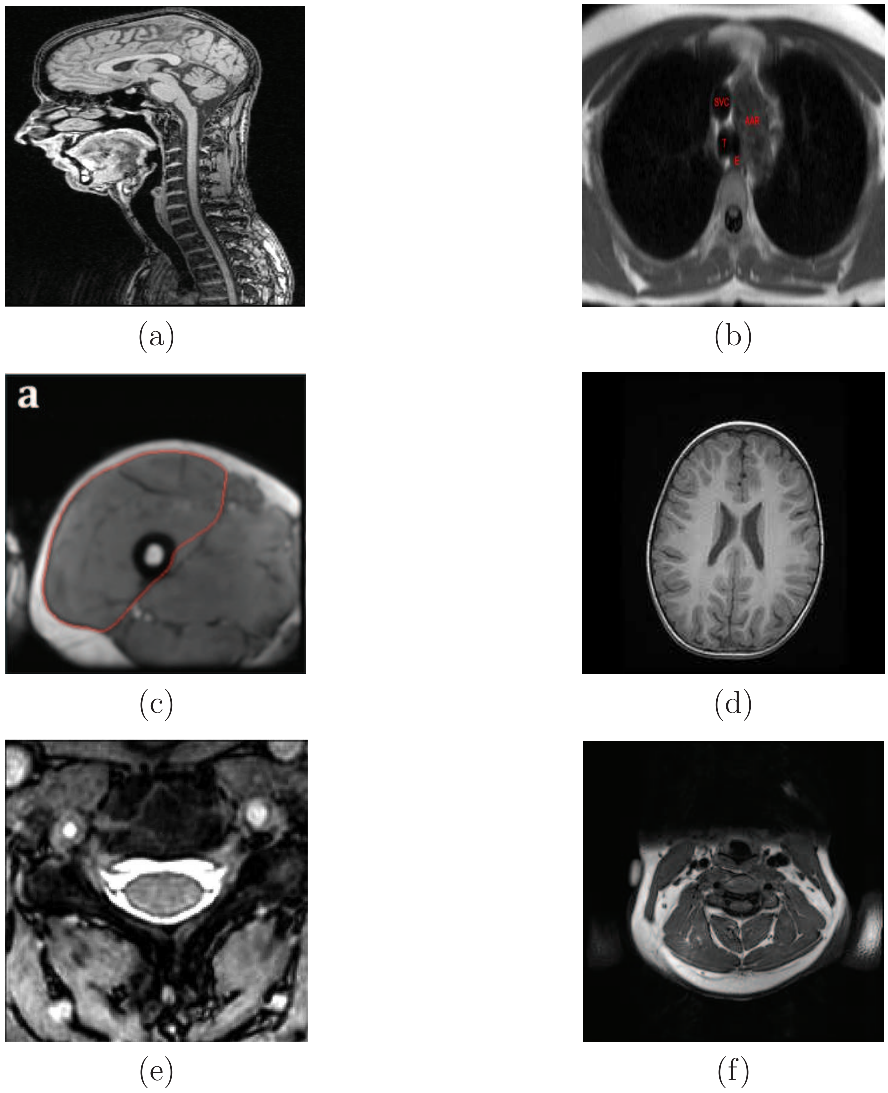

Figure 5.1: Comparison of contrasts between: (a) trachea, spinal cord and intervertebral disks [6]; (b) ventricle [7]; (c) quadriceps, femur and bone marrows [8]; (d) head [9]; (e) spinal cord and canal [10]; and (e) neck muscles.

interactions is proposed. It uses a novel PDM for multiple close neck muscles with a 4mm inter-slice gap and thickness in MR images which provides segmentations with no overlaps and gaps inside a muscle.

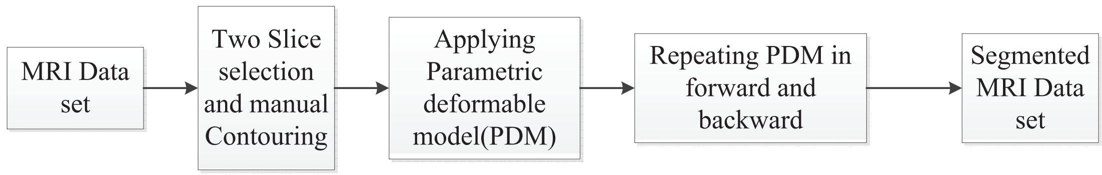

Figure 5.2: Operational flow of proposed CP method.

5.2 Methodology

The proposed CP method is not limited to only neck regions but can be applied on any volume image. In it, two initial slices are selected from a MRI data set, the first the middle slice of the first half of the data set and the second a slice from the second half in which manual contouring is implemented. The operator can draw the contours with minimal effort because the deformable process drags them towards muscle boundaries. There are three reasons for selecting two initial slices: firstly, the shapes of neck muscles change rapidly in a MR image sequence; secondly, the thickness of each MRI slice is 4 mm with a gap of 4 mm between two consecutive slices; and, finally, the contrasts between neck muscles are almost the same as each other and the muscles are very compact. The most important part of a CP method is its deformable model-based segmentation which controls mainly the segmentation accuracy. In this method, a novel PDM is used, the motivations and full process for which are discussed in Chapter 4. It actually overcomes the difficulties faced by CP methods due to the contrast, compactness and shape variations among objects' slices. Segmentation of the neighbouring slices of the initial ones is implemented by considering the final contour of the initial slices refined by the PDM as initial contour. This process is repeated in forward and backward directions from the initial slices until all the slices are covered, as illustrated in Figure 5.2.

5.3 Numerical Results

In the experimental analysis, fifteen clinical MRI data sets captured by the Canberra Imaging Group at Calvary John James Hospital, Deakin, Canberra, Australia, were used. The patients' statistics and imaging parameters of the data sets are discussed in detail in 3.3.1.4 and 3.3.1.2 respectively in Chapter 3.

In this method, the sigmas of the Gaussian filter in the PDM are very low due to objects' model staying close to the objects' boundaries and capturing fine details of the energy distribution, with only two scales used for the multi-scale Gaussian potential force.

The 2D automatic segmentation results for six neck muscles in a MRI data set are shown in Figure 5.3. Figure 5.4 shows the corresponding 3D depiction of the segmented dataset. The automatic contours are almost exactly the same as those of the gold standard generated by three anatomical experts who also validated the automatic results. It can be seen from the 2D results that, although the muscles are very compact and have similar intensities, the automatic segmented contours match the ground truths fairly well, in particular, those of the semispinalis capitis and splenius capitis muscles are very close to those of both each other and other muscles. Table 5.1 shows the mean DSC values for each muscle in each patient for the region of interest. The average DSC values with standard deviations of the six muscles of 15 subjects are presented in Table 5.2 which shows that the overall average DSC is 0.8835 ± 0.0117, a really good indication of muscle segmentation as a DSC value equal to or greater than 0.7 is regarded as good agreement [156]. On the other hand, the registration-based method in chapter-3 achieved 0.85 ± 0.022 average DSC with high computational complexity but it is totally automatic whereas the CP-based method requires a little manual

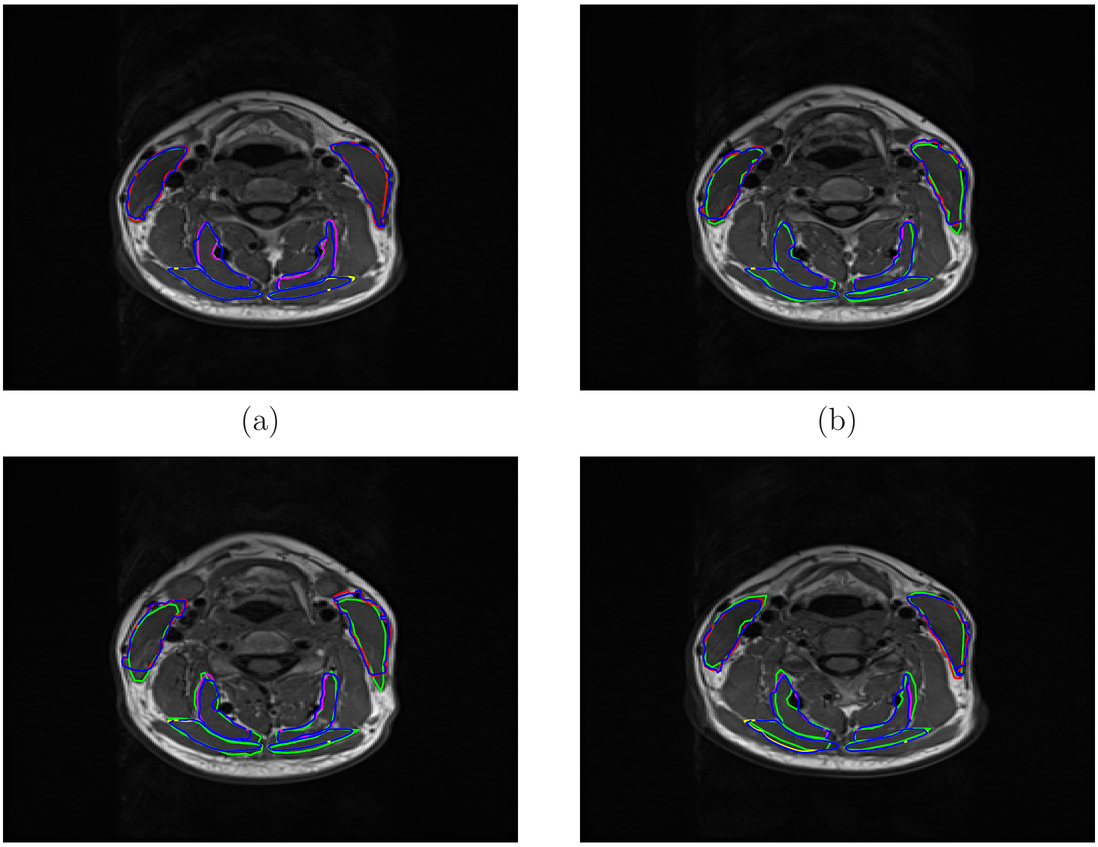

(a) (b)

(b) (b)

Figure 5.3: Auto-segmentation results for neck muscles using proposed CP method on one data set (green curves represent ground truths of muscles, blue curves initial models, and red, magenta and yellow final deformed curves for sternocleidomastoid, semispinalis capitis and splenius capitis muscles respectively).

interaction. Although Baudin *et al.* [4] obtained a good DSC of 0.86 ± 0.07 for thigh muscles, the highest DSC value reported for muscle segmentation, they exploited a 3-point Dixon MRI sequence with the motivation of clarifying inter-muscular boundaries.

5.4 Discussion

Although the proposed method has good accuracy and its computational complexity is far less than those of registration-based techniques, taking only 11 seconds

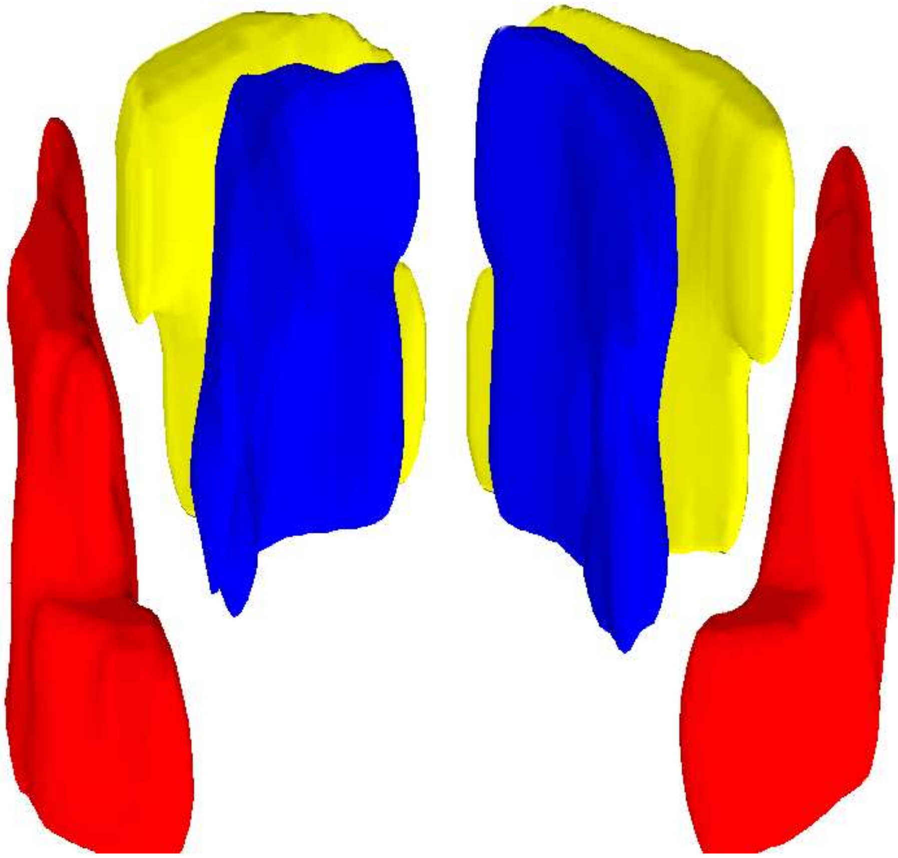

Figure 5.4: Depictions of volumetric auto-segmentations of data sets bilateral sternocleidomastoid (red), semispinalis capitis (blue) and splenius capitis (yellow) muscle volumes from C1 to C7 intervertebral levels.

per image for six muscles using a HP z230 tower workstation with an Intel(R) Core(TM) i7-4770 CPU, 3.40 GHz processor and 4 GB of RAM running on the Windows 7 SP1 operating system and un-optimized Matlab code, it requires manual interactions on the two initial slices around 5 minutes 20 seconds. Also, the time could be further reduced by implementing a C-programming-based Matlab execution which will be implemented in future. Therefore, CP-based methods have brighter prospects in terms of the future segmentation paradigm than registration-based ones if they can be implemented totally automatically. Also, it is still wise to use them instead of registration ones due to their good accuracy, low execution times and little need for manual interaction.

Table 5.1: Mean DSC values over C1 to C7 intervertebral levels of different individuals for left sternocleidomastoid (Left Stern.), right sternocleidomastoid (Right Stern.), Left semispinalis capitis (Left Semi. Capi.), Right semispinalis capitis (Right Semi. Capi.), Left splenius capitis (Left Sple. Capi.), Right splenius capitis (Right Sple. Capi.).

Patient index	Left Stern.	Right Stern.	Left Semi. Capi.	Right Semi. Capi.	Left Sple. Capi.	Right Sple. Capi.
Patient-1	0.85	0.89	0.9	0.87	0.84	0.93
Patient-2	0.9	0.88	0.88	0.88	0.93	0.89
Patient-3	0.91	0.92	0.85	0.87	0.92	0.92
Patient-4	0.89	0.85	0.86	0.85	0.85	0.86
Patient-5	0.86	0.9	0.92	0.91	0.84	0.94
Patient-6	0.84	0.85	0.89	0.86	0.83	0.89
Patient-7	0.87	0.86	0.89	0.91	0.92	0.9
Patient-8	0.86	0.82	0.84	0.87	0.94	0.94
Patient-9	0.91	0.92	0.86	0.85	0.92	0.91
Patient-10	0.86	0.84	0.87	0.84	0.83	0.87
Patient-11	0.87	0.83	0.85	0.92	0.84	0.89
Patient-12	0.88	0.91	0.83	0.86	0.93	0.9
Patient-13	0.84	0.84	0.91	0.88	0.89	0.92
Patient-14	0.86	0.93	0.84	0.89	0.9	0.84
Patient-15	0.93	0.89	0.85	0.9	0.93	0.93

Table 5.2: Mean DSC values for six neck muscles of 15 subjects for C1 to C7 intervertebral levels.

Muscle Name	DSC
Left sternocleidomastoid	0.8751 ± 0.0587
Right sternocleidomastoid	0.8803 ± 0.0564
Left semispinalis capitis	0.8737 ± 0.0575
Right semispinalis capitis	0.8763 ± 0.0643
Left splenius capitis	0.8927 ± 0.0603
Right splenius capitis	0.9028 ± 0.0743
Overall mean	0.8835 ± 0.0117

The requirement for manual interactions could be reduced to one initial slice if the proposed CP method used the organs mentioned in section 5.1 which have good contrast and no compactness as well as high-resolution MRI sequences, for example, no gap and a $1mm$ slice thickness. A user requires minimal interactions which are insensitive to segmentation accuracy because the PDM uses strong external forces which drag the vertices of the initial contours towards muscle boundaries. The automatic segmentation results produced by the proposed CP method were verified by 3 different cervical anatomical experts on different days, which is strong confirmation of the systems robustness. The initial contours delineated by different experts were dragged to same boundary positions due to strong external forces.

5.5 Conclusion

In this chapter, a combination of CP and PDM segmentation frameworks for neck muscles segmentation and reconstruction is introduced. The experimental results indicate its high accuracy, execution times and reproducibility performances for real clinical data, as verified by radiologists. This system definitely reduces the manual contouring time and labor and is time compatible in terms of practical clinical use for surgical planning.

In future, a fully automatic CP-based method which does not depend on initial manual interactions will be developed by incorporating a statistical model in the middle slice. Also, it will be implemented using a C-programming-based Matlab execution to increase its speed.

Chapter 6

Conclusions and Suggestions for Further Study

The main goal of this research was to automatically segment neck muscles in medical images with good accuracy which is currently a challenge for researchers. The significant findings, facts and contributions of this study are discussed in section 6.1 and suggestions for further study provided in section 6.2

6.1 Conclusions

This study presented two different approaches for automatically segmenting neck muscles with high accuracy which are not only applicable for neck muscles but can also be applied for any medical image segmentation. Segmentations were undertaken for both healthy and unhealthy control groups of actual patients, with the results obtained tested by medical experts who also research and analyze whiplash. They examined the results separately on different days and agreed with the automatic contours obtained by the proposed methods. Therefore, this research will clearly be able to assist physicians to understand the shapes and sizes of neck muscles for diagnosing WADs which is not possible using existing segmentation methods due to the complexity of the neck's anatomy. The first approach, which is based on a registration framework and deformable model, achieved good accuracy for neck muscles segmentation fully automatically and could handle anatomical variabilities using its unique registration framework. The automatic contours of this method matched with the ground truths of neck muscles fairly well and, compared with current registration-based methods that use optimal atlases for brain image segmentation because there is no such method available for muscles segmentation, its average DSC value indicated that it performed best. Although this approachs accuracy could be increased using a multi-atlas technique, its complexity would also increase.

Registration-based methods normally experience high computational complexity and face difficulties in handling anatomical variabilities. Also, the proposed method requires an atlas database which is often not available for all cases and, furthermore, if a biomarker exists in the input volume image, it cannot segment it. Therefore, a contour propagation-based method designed based on a PDM was developed. While it involves a semi-automatic process, it has very low computational complexity and can easily handle anatomical variabilities and also segment any biomarker, with its average DSC value showing significant improvement in terms of segmentation accuracy.

Another part of this research was the development of a multiple-object PDM which was used in both approaches. It incorporates a new conditional energy distribution using the major axis of an object which reduces the shortcomings of a traditional PDM. It is able to handle topology changes and does not provide overlaps because it includes a new overlap removal technique.

6.2 Future Works

Although the approaches proposed in this research automatically achieved good segmentation accuracy, there is still potential to increase accuracy using a graphics processing unit in a multi-atlas technique and decrease computational complexity by reducing the registration step in the framework introduced in Chapter 3.

In future work, the proposed registration-based method will be implemented in a graphics processing unit (GPU) environment using the C++ programming language and code parallelization to speed up system execution. Although segmentation was performed for only eight neck muscles in this study, as it can segment others without any trade-off in terms of segmentation accuracy, in future, segmentation will be performed for the longus capitis, longus colli, multifidus, semispinalis cervicus, rectus capitis posterior minor and rectus capitis posterior major. Also, as a multi-atlas-based method can enhance segmentation accuracy which requires high computational cost, it will be applied in a future registration and deformation framework.

The performance of the conditional energy distribution discussed in Chapter 4 could be enhanced by resolving the problem of the energy distribution in the end vicinity of the major axis.

Finally, the semi-automatic process presented in Chapter 5 could be converted into a fully automatic one by incorporating shape information.

Bibliography

[1] "Child with leg pain," [Online]. Available: http://radiologypics.com/2013/03/31/unknown.case.36.child.with.leg.pain/.

[2] "Planes and directions of the body," [Online]. Available: http://medicineatlas.com/2016/01/planes-and-directions-of-the-body/.

[3] "Extremities," [Online]. Available: http://www.rad.msu.edu/Course/RAD 553/image_lib/extremities/LL15_e.htm.

[4] P.-Y. Baudin, N. Azzabou, P. G. Carlier, and N. Paragios, "Prior knowledge, random walks and human skeletal muscle segmentation," in *Medical Image Computing and Computer-Assisted Intervention–MICCAI 2012*. Springer, 2012, pp. 569–576.

[5] J. A. Bogovic, J. L. Prince, and P.-L. Bazin, "A multiple object geometric deformable model for image segmentation," *Computer Vision and Image Understanding*, vol. 117, no. 2, pp. 145–157, 2013.

[6] S. Seifert, I. Wächter, G. Schmelzle, and R. Dillmann, "A knowledge-based approach to soft tissue reconstruction of the cervical spine," *Medical Imaging, IEEE Transactions on*, vol. 28, no. 4, pp. 494–507, 2009.

[7] "Normal anatomy," [Online]. Available: https://www.med-ed.virginia.edu/courses/rad/cardiacmr/Anatomy/Normal.html.

[8] E. Ahmad, M. H. Yap, H. Degens, and J. McPhee, "Enhancement of MRI human thigh muscle segmentation by template-based framework," in *Control System, Computing and Engineering (ICCSCE), 2014 IEEE International Conference on*. IEEE, 2014, pp. 405–410.

[9] "Axial mri atlas: Clinical neuroanatomy atlas," [Online]. Available: http://users.umassmed.edu/charlene.baron/pdfs/axialmriatlas08oe.pdf.

[10] "Magnetic resonance imaging (MRI)," [Online]. Available: http://www.infocusdiagnostics.com/3tmri.php.

[11] "Warning over whiplash 'epidemic'," [Online]. Available: http://news.bbc.co.uk/2/hi/health/7729336.stm.

[12] "Acute whiplash," [Online]. Available: http://www.maa.nsw.gov.au/for-professionals/for-health-professionals/acute-whiplash.

[13] J. M. Elliott, A. R. Pedler, G. A. Jull, L. Van Wyk, G. G. Galloway, and S. P. O'Leary, "Differential changes in muscle composition exist in traumatic and nontraumatic neck pain," *Spine*, vol. 39, no. 1, pp. 39–47, 2014.

[14] J. Elliott, G. Jull, J. T. Noteboom, and G. Galloway, "MRI study of the cross-sectional area for the cervical extensor musculature in patients with persistent whiplash associated disorders (WAD)," *Manual therapy*, vol. 13, no. 3, pp. 258–265, 2008.

[15] "The whiplash injury," [Online]. Available: http://www.montazem.de/english/html/whiplash-injury.html.

[16] Y. Hagström and J. Carlsson, "Prolonged functional impairments after whiplash injury." *Scandinavian journal of rehabilitation medicine*, vol. 28, no. 3, pp. 139–146, 1996.

[17] L. Barnsley, S. Lord, and N. Bogduk, "Whiplash injury," *Pain*, vol. 58, no. 3, pp. 283–307, 1994.

[18] M. D. Freeman, A. C. Croft, A. M. Rossignol, D. S. Weaver, and M. Reiser, "A review and methodologic critique of the literature refuting whiplash syndrome," *Spine*, vol. 24, no. 1, pp. 86–96, 1999.

[19] S. M. Foreman and A. C. Croft, *Whiplash injuries: the cervical acceleration/deceleration syndrome.* Lippincott Williams & Wilkins, 2001.

[20] P.-O. Bylund and U. Björnstig, "Sick leave and disability pension among passenger car occupants injured in urban traffic," *Spine*, vol. 23, no. 9, pp. 1023–1028, 1998.

[21] Q. Bismil and M. Bismil, "Myofascial-entheseal dysfunction in chronic whiplash injury: an observational study," *JRSM short reports*, vol. 3, no. 8, p. 57, 2012.

[22] S. Andrews and G. Hamarneh, "The generalized log-ratio transformation: Learning shape and adjacency priors for simultaneous thigh muscle segmentation," *IEEE Transactions on Medical Imaging*, vol. 34, no. 9, pp. 1773–1787, Sept 2015.

[23] P. Mesejo, A. Valsecchi, L. Marrakchi-Kacem, S. Cagnoni, and S. Damas, "Biomedical image segmentation using geometric deformable models and metaheuristics," *Computerized Medical Imaging and Graphics*, vol. 43, pp. 167–178, 2015.

[24] P.-Y. Baudin, N. Azzabou, P. G. Carlier, and N. Paragios, "Automatic skeletal muscle segmentation through random walks and graph-based seed placement," in *9th IEEE International Symposium on Biomedical Imaging*, 2012, pp. 1036–1039.

[25] P. K. Sahoo, S. Soltani, and A. K. Wong, "A survey of thresholding techniques," *Computer vision, graphics, and image processing*, vol. 41, no. 2, pp. 233–260, 1988.

[26] A. Rusu, "Segmentation of bone structures in magnetic resonance images (MRI) for human hand skeletal kinematics modelling," Ph.D. dissertation, Erasmus Mundus in Vision and Robotics (VIBOT), 2012.

[27] Z. Ma, J. M. R. Tavares, R. N. Jorge, and T. Mascarenhas, "A review of algorithms for medical image segmentation and their applications to the female pelvic cavity," *Computer Methods in Biomechanics and Biomedical Engineering*, vol. 13, no. 2, pp. 235–246, 2010.

[28] N. Otsu, "A threshold selection method from gray-level histograms," *Automatica*, vol. 11, no. 285-296, pp. 23–27, 1975.

[29] J. Kittler, J. Illingworth, and J. Föglein, "Threshold selection based on a simple image statistic," *Computer vision, graphics, and image processing*, vol. 30, no. 2, pp. 125–147, 1985.

[30] G. Kom, A. Tiedeu, and M. Kom, "Automated detection of masses in mammograms by local adaptive thresholding," *Computers in Biology and Medicine*, vol. 37, no. 1, pp. 37–48, 2007.

[31] N. Sang, H. Li, W. Peng, and T. Zhang, "Knowledge-based adaptive thresholding segmentation of digital subtraction angiography images," *Image and Vision Computing*, vol. 25, no. 8, pp. 1263–1270, 2007.

[32] H. Tian, T. Srikanthan, and K. V. Asari, "Automatic segmentation algorithm for the extraction of lumen region and boundary from endoscopic images," *Medical and Biological Engineering and Computing*, vol. 39, no. 1, pp. 8–14, 2001.

[33] J. Zhang, C.-H. Yan, C.-K. Chui, and S.-H. Ong, "Fast segmentation of bone in CT images using 3D adaptive thresholding," *Computers in biology and medicine*, vol. 40, no. 2, pp. 231–236, 2010.

[34] A. J. Burghardt, G. J. Kazakia, and S. Majumdar, "A local adaptive threshold strategy for high resolution peripheral quantitative computed tomography of trabecular bone," *Annals of biomedical engineering*, vol. 35, no. 10, pp. 1678–1686, 2007.

[35] R. Adams and L. Bischof, "Seeded region growing," *IEEE Transactions on pattern analysis and machine intelligence*, vol. 16, no. 6, pp. 641–647, 1994.

[36] R. Pohle and K. D. Toennies, "Segmentation of medical images using adaptive region growing," in *Medical Imaging 2001.* International Society for Optics and Photonics, 2001, pp. 1337–1346.

[37] J. Yi and J. B. Ra, "Vascular segmentation algorithm using locally adaptive region growing based on centerline estimation," in *Medical Imaging 2001.* International Society for Optics and Photonics, 2001, pp. 1329–1336.

[38] Z. Pan and J. Lu, "A bayes-based region-growing algorithm for medical image segmentation," *Computing in Science & Engineering*, vol. 9, no. 4, pp. 32–38, 2007.

[39] J. Dehmeshki, X. Ye, and J. Costello, "Shape based region growing using derivatives of 3D medical images: application to semiautomated detection of pulmonary nodules," in *Image Processing, 2003. ICIP 2003. Proceedings. 2003 International Conference on*, vol. 1. IEEE, 2003, pp. I–1085.

[40] L. G. Nyúl, J. Kanyó, E. Máté, G. Makay, E. Balogh, M. Fidrich, and A. Kuba, "Method for automatically segmenting the spinal cord and canal

from 3D CT images," in *Computer Analysis of Images and Patterns*. Springer, 2005, pp. 456–463.

[41] G. Rai and T. Nair, "Gradient based seeded region grow method for CT angiographic image segmentation," *arXiv preprint arXiv:1001.3735*, 2010.

[42] J.-F. Mangin, V. Frouin, I. Bloch, J. Régis, and J. López-Krahe, "From 3D magnetic resonance images to structural representations of the cortex topography using topology preserving deformations," *Journal of Mathematical Imaging and Vision*, vol. 5, no. 4, pp. 297–318, 1995.

[43] J. K. Udupa and S. Samarasekera, "Fuzzy connectedness and object definition: theory, algorithms, and applications in image segmentation," *Graphical models and image processing*, vol. 58, no. 3, pp. 246–261, 1996.

[44] I. Manousakas, P. Undrill, G. Cameron, and T. Redpath, "Split-and-merge segmentation of magnetic resonance medical images: performance evaluation and extension to three dimensions," *Computers and Biomedical Research*, vol. 31, no. 6, pp. 393–412, 1998.

[45] V. Grau, A. Mewes, M. Alcaniz, R. Kikinis, and S. K. Warfield, "Improved watershed transform for medical image segmentation using prior information," *IEEE transactions on medical imaging*, vol. 23, no. 4, pp. 447–458, 2004.

[46] H. Ng, S. Ong, K. Foong, P. Goh, and W. Nowinski, "Medical image segmentation using k-means clustering and improved watershed algorithm," in *2006 IEEE Southwest Symposium on Image Analysis and Interpretation*. IEEE, 2006, pp. 61–65.

[47] G. Hamarneh and X. Li, "Watershed segmentation using prior shape and appearance knowledge," *Image and Vision Computing*, vol. 27, no. 1, pp. 59–68, 2009.

[48] L. Najman and M. Schmitt, "Geodesic saliency of watershed contours and hierarchical segmentation," *IEEE Transactions on Pattern Analysis and Machine Intelligence*, vol. 18, no. 12, pp. 1163–1173, 1996.

[49] M. Straka, A. La Cruz, A. Kochl, M. Srámek, E. Groller, and D. Fleischmann, "3D watershed transform combined with a probabilistic atlas for medical image segmentation," *Journal of Medical Informatics & Technologies*, vol. 6, pp. IT69–78, 2003.

[50] H. A. Vrooman, C. A. Cocosco, R. Stokking, M. A. Ikram, M. W. Vernooij, M. M. Breteler, and W. J. Niessen, "kNN-based multi-spectral MRI brain tissue classification: manual training versus automated atlas-based training," in *Medical Imaging.* International Society for Optics and Photonics, 2006, pp. 61 443L–61 443L.

[51] A. Sarti, C. Corsi, E. Mazzini, and C. Lamberti, "Maximum likelihood segmentation of ultrasound images with rayleigh distribution," *IEEE transactions on ultrasonics, ferroelectrics, and frequency control*, vol. 52, no. 6, pp. 947–960, 2005.

[52] J. Alirezaie, M. Jernigan, and C. Nahmias, "Neural network-based segmentation of magnetic resonance images of the brain," *IEEE Transactions on Nuclear Science*, vol. 44, no. 2, pp. 194–198, 1997.

[53] N. Benamrane, A. Aribi, and L. Kraoula, "Fuzzy neural networks and genetic algorithms for medical images interpretation," in *Geometric Modeling and Imaging–New Trends (GMAI'06).* IEEE, 1993, pp. 259–264.

[54] S. Wang, W. Zhu, and Z.-P. Liang, "Shape deformation: SVM regression and application to medical image segmentation," in *Computer Vision, 2001. ICCV 2001. Proceedings. Eighth IEEE International Conference on*, vol. 2. IEEE, 2001, pp. 209–216.

[55] S. C. Mitchell, J. G. Bosch, B. P. Lelieveldt, R. J. Van der Geest, J. H. Reiber, and M. Sonka, "3-D active appearance models: segmentation of cardiac MR and ultrasound images," *IEEE transactions on medical imaging*, vol. 21, no. 9, pp. 1167–1178, 2002.

[56] S. C. Mitchell, B. P. F. Lelieveldt, R. J. van der Geest, J. Schaap, J. H. C. Reiber, and M. Sonka, "Segmentation of cardiac MR images: an active appearance model approach," pp. 224–234.

[57] R. Beichel, H. Bischof, F. Leberl, and M. Sonka, "Robust active appearance models and their application to medical image analysis," *IEEE transactions on medical imaging*, vol. 24, no. 9, pp. 1151–1169, 2005.

[58] B. Van Ginneken, A. F. Frangi, J. J. Staal, B. M. ter Haar Romeny, and M. A. Viergever, "Active shape model segmentation with optimal features," *IEEE transactions on medical imaging*, vol. 21, no. 8, pp. 924–933, 2002.

[59] T. Heimann and H.-P. Meinzer, "Statistical shape models for 3D medical image segmentation: A review," *Medical image analysis*, vol. 13, no. 4, pp. 543–563, 2009.

[60] M. C. Clark, L. O. Hall, D. B. Goldgof, L. P. Clarke, R. P. Velthuizen, and M. S. Silbiger, "MRI segmentation using fuzzy clustering techniques," *IEEE Engineering in Medicine and Biology Magazine*, vol. 13, no. 5, pp. 730–742, 1994.

[61] N. A. Mohamed, M. N. Ahmed, and A. Farag, "Modified fuzzy c-mean in medical image segmentation," in *Acoustics, Speech, and Signal Processing, 1999. Proceedings., 1999 IEEE International Conference on*, vol. 6. IEEE, 1999, pp. 3429–3432.

[62] M. N. Ahmed, S. M. Yamany, N. Mohamed, A. A. Farag, and T. Moriarty, "A modified fuzzy c-means algorithm for bias field estimation and segmentation of MRI data," *IEEE transactions on medical imaging*, vol. 21, no. 3, pp. 193–199, 2002.

[63] D.-Q. Zhang and S.-C. Chen, "A novel kernelized fuzzy c-means algorithm with application in medical image segmentation," *artificial intelligence in medicine*, vol. 32, no. 1, pp. 37–50, 2004.

[64] D. L. Pham and J. L. Prince, "An adaptive fuzzy c-means algorithm for image segmentation in the presence of intensity inhomogeneities," *Pattern recognition letters*, vol. 20, no. 1, pp. 57–68, 1999.

[65] W. Cai, S. Chen, and D. Zhang, "Fast and robust fuzzy c-means clustering algorithms incorporating local information for image segmentation," *Pattern Recognition*, vol. 40, no. 3, pp. 825–838, 2007.

[66] J. Wang, J. Kong, Y. Lu, M. Qi, and B. Zhang, "A modified FCM algorithm for mri brain image segmentation using both local and non-local spatial constraints," *Computerized Medical Imaging and Graphics*, vol. 32, no. 8, pp. 685–698, 2008.

[67] H. Zhou, G. Schaefer, A. Sadka, and M. E. Celebi, "Anisotropic mean shift based fuzzy c-means segmentation of skin lesions," in *Proceedings of the 5th international conference on Soft computing as transdisciplinary science and technology.* ACM, 2008, pp. 438–443.

[68] S. Chen and D. Zhang, "Robust image segmentation using FCM with spatial constraints based on new kernel-induced distance measure," *IEEE Transactions on Systems, Man, and Cybernetics, Part B (Cybernetics)*, vol. 34, no. 4, pp. 1907–1916, 2004.

[69] L. Liao, T. Lin, and B. Li, "MRI brain image segmentation and bias field correction based on fast spatially constrained kernel clustering approach," *Pattern Recognition Letters*, vol. 29, no. 10, pp. 1580–1588, 2008.

[70] M. A. Jacobs, R. A. Knight, H. Soltanian-Zadeh, Z. G. Zheng, A. V. Goussev, D. J. Peck, J. P. Windham, and M. Chopp, "Unsupervised segmentation of multiparameter MRI in experimental cerebral ischemia with comparison to T2, diffusion, and ADC MRI parameters and histopathological validation," *Journal of Magnetic Resonance Imaging*, vol. 11, no. 4, pp. 425–437, 2000.

[71] B. Biswal, N. Shah, N. Shah, M. Trivedi, S. Nayak, and H. Dave, "Automatic segmentation of pancreatic images using ISODATA alorithm," in *ASCO Annual Meeting Proceedings*, vol. 24, no. 18_suppl, 2006, p. 14149.

[72] X. Tai and W. Song, "An improved approach based on FCM using feature fusion for medical image retrieval," in *Fuzzy Systems and Knowledge Discovery, 2007. FSKD 2007. Fourth International Conference on*, vol. 2. IEEE, 2007, pp. 336–342.

[73] J.-S. Lin, K.-S. Cheng, and C.-W. Mao, "A fuzzy hopfield neural network for medical image segmentation," *IEEE Transactions on Nuclear Science*, vol. 43, no. 4, pp. 2389–2398, 1996.

[74] K.-S. Cheng, J.-S. Lin, and C.-W. Mao, "The application of competitive hopfield neural network to medical image segmentation," *IEEE Transactions on Medical Imaging*, vol. 15, no. 4, pp. 560–567, 1996.

[75] S. Becker and M. Plumbley, "Unsupervised neural network learning procedures for feature extraction and classification," *Applied Intelligence*, vol. 6, no. 3, pp. 185–203, 1996.

[76] C. Xu, D. L. Pham, and J. L. Prince, "Image segmentation using deformable models," *Handbook of medical imaging*, vol. 2, pp. 129–174, 2000.

[77] T. McInerney and D. Terzopoulos, "Deformable models in medical image analysis: a survey," *Medical image analysis*, vol. 1, no. 2, pp. 91–108, 1996.

[78] D. Terzopoulos, "On matching deformable models to images," in *Topical Meeting on Machine Vision Tech. Digest Series*, vol. 12, 1987, pp. 160–167.

[79] M. Kass, A. Witkin, and D. Terzopoulos, "Snakes: Active contour models," *International journal of computer vision*, vol. 1, no. 4, pp. 321–331, 1988.

[80] D. Terzopoulos, A. Witkin, and M. Kass, "Constraints on deformable models: Recovering 3D shape and nonrigid motion," *Artificial intelligence*, vol. 36, no. 1, pp. 91–123, 1988.

[81] M.-O. Berger, "Snake growing," in *European Conference on Computer Vision*. Springer, 1990, pp. 570–572.

[82] L. D. Cohen, "On active contour models and balloons," *CVGIP: Image understanding*, vol. 53, no. 2, pp. 211–218, 1991.

[83] N. Ueda and K. Mase, "Tracking moving contours using energy-minimizing elastic contour models," in *European Conference on Computer Vision*. Springer, 1992, pp. 453–457.

[84] N. F. Rougon and F. J. Preteux, "Directional adaptive deformable models for segmentation with application to 2D and 3D medical images," in *Medical Imaging 1993*. International Society for Optics and Photonics, 1993, pp. 193–207.

[85] L. D. Cohen and I. Cohen, "Finite-element methods for active contour models and balloons for 2-D and 3-D images," *IEEE Transactions on Pattern Analysis and machine intelligence*, vol. 15, no. 11, pp. 1131–1147, 1993.

[86] F. Leitner and P. Cinquin, "From splines and snakes to snake splines," in *Geometric reasoning for perception and action*. Springer, 1993, pp. 264–281.

[87] C. A. Davatzikos and J. L. Prince, "An active contour model for mapping the cortex," *IEEE Transactions on Medical Imaging*, vol. 14, no. 1, pp. 65–80, 1995.

[88] T. McInerney and D. Terzopoulos, "A dynamic finite element surface model for segmentation and tracking in multidimensional medical images with application to cardiac 4D image analysis," *Computerized Medical Imaging and Graphics*, vol. 19, no. 1, pp. 69–83, 1995.

[89] C. Xu and J. L. Prince, "Snakes, shapes, and gradient vector flow," *IEEE Transactions on image processing*, vol. 7, no. 3, pp. 359–369, 1998.

[90] P. C. Gonçalves, J. Tavares, and R. N. Jorge, "Segmentation and simulation of objects represented in images using physical principles," *Computer Modeling in Engineering & Sciences*, vol. 32, no. 1, pp. 45–55, 2008.

[91] C. Xu and J. L. Prince, "Generalized gradient vector flow external forces for active contours," *Signal processing*, vol. 71, no. 2, pp. 131–139, 1998.

[92] H. Delingette, "Simplex meshes: A general representation for 3D shape reconstruction," in *Computer Vision and Pattern Recognition, 1994. Proceedings CVPR'94., 1994 IEEE Computer Society Conference on.* IEEE, 1994, pp. 856–859.

[93] D. MacDonald, D. Avis, and A. C. Evans, "Multiple surface identification and matching in magnetic resonance images," in *Visualization in Biomedical Computing 1994.* International Society for Optics and Photonics, 1994, pp. 160–169.

[94] T. F. Cootes, A. Hill, C. J. Taylor, and J. Haslam, "The use of active shape models for locating structures in medical images," in *Biennial International Conference on Information Processing in Medical Imaging.* Springer, 1993, pp. 33–47.

[95] T. F. Cootes, C. J. Taylor, D. H. Cooper, and J. Graham, "Active shape models-their training and application," *Computer vision and image understanding*, vol. 61, no. 1, pp. 38–59, 1995.

[96] T. F. Cootes, G. J. Edwards, C. J. Taylor *et al.*, "Active appearance models," *IEEE Transactions on pattern analysis and machine intelligence*, vol. 23, no. 6, pp. 681–685, 2001.

[97] M. J. M. Vasconcelos and J. M. R. Tavares, "Methods to automatically build point distribution models for objects like hand palms and faces represented in images," 2008.

[98] V. Caselles, R. Kimmel, and G. Sapiro, "Geodesic active contours," *International journal of computer vision*, vol. 22, no. 1, pp. 61–79, 1997.

[99] T. F. Chan and L. A. Vese, "Active contours without edges," *Image processing, IEEE transactions on*, vol. 10, no. 2, pp. 266–277, 2001.

[100] R. Malladi, J. A. Sethian, and B. C. Vemuri, “Shape modeling with front propagation: A level set approach,” *IEEE transactions on pattern analysis and machine intelligence*, vol. 17, no. 2, pp. 158–175, 1995.

[101] A. Yezzi, S. Kichenassamy, A. Kumar, P. Olver, and A. Tannenbaum, “A geometric snake model for segmentation of medical imagery,” *IEEE Transactions on medical imaging*, vol. 16, no. 2, pp. 199–209, 1997.

[102] Y. Bai, X. Han, and J. L. Prince, “Geometric deformable models,” in *Handbook of Biomedical Imaging.* Springer, 2015, pp. 83–104.

[103] V. Caselles, F. Catté, T. Coll, and F. Dibos, “A geometric model for active contours in image processing,” *Numerische mathematik*, vol. 66, no. 1, pp. 1–31, 1993.

[104] V. Caselles, R. Kimmel, G. Sapiro, and C. Sbert, “Minimal surfaces based object segmentation,” *IEEE Transactions on Pattern Analysis and Machine Intelligence*, vol. 19, no. 4, pp. 394–398, 1997.

[105] S. Kichenassamy, A. Kumar, P. Olver, A. Tannenbaum, and A. Yezzi, “Gradient flows and geometric active contour models,” in *Computer Vision, 1995. Proceedings., Fifth International Conference on.* IEEE, 1995, pp. 810–815.

[106] S. Kichenassamy, A. Kumar, P. Olver, A. Tannenbaum, and A. Yezzi Jr, “Conformal curvature flows: from phase transitions to active vision,” *Archive for Rational Mechanics and Analysis*, vol. 134, no. 3, pp. 275–301, 1996.

[107] K. Siddiqi, Y. B. Lauziere, A. Tannenbaum, and S. W. Zucker, “Area and length minimizing flows for shape segmentation,” *IEEE Transactions on Image Processing*, vol. 7, no. 3, pp. 433–443, 1998.

[108] S. C. Zhu and A. Yuille, “Region competition: Unifying snakes, region growing, and bayes/MDL for multiband image segmentation,” *IEEE transactions*

on pattern analysis and machine intelligence, vol. 18, no. 9, pp. 884–900, 1996.

[109] A. Yezzi, A. Tsai, and A. Willsky, "A statistical approach to snakes for bimodal and trimodal imagery," in *Computer Vision, 1999. The Proceedings of the Seventh IEEE International Conference on*, vol. 2. IEEE, 1999, pp. 898–903.

[110] X. Xie and M. Mirmehdi, "Rags: Region-aided geometric snake," *IEEE Transactions on Image Processing*, vol. 13, no. 5, pp. 640–652, 2004.

[111] R. Ronfard, "Region-based strategies for active contour models," *International journal of computer vision*, vol. 13, no. 2, pp. 229–251, 1994.

[112] N. Paragios and R. Deriche, "Geodesic active contours and level sets for the detection and tracking of moving objects," *IEEE Transactions on pattern analysis and machine intelligence*, vol. 22, no. 3, pp. 266–280, 2000.

[113] ——, "Unifying boundary and region-based information for geodesic active tracking," in *Computer Vision and Pattern Recognition, 1999. IEEE Computer Society Conference on.*, vol. 2. IEEE, 1999.

[114] L. D. Cohen, E. Bardinet, and N. Ayache, "Surface reconstruction using active contour models," Ph.D. dissertation, INRIA, 1993.

[115] J. Kim, J. W. Fisher, A. Yezzi, M. Çetin, and A. S. Willsky, "A nonparametric statistical method for image segmentation using information theory and curve evolution," *IEEE Transactions on Image processing*, vol. 14, no. 10, pp. 1486–1502, 2005.

[116] X. Han, C. Xu, and J. L. Prince, "A topology preserving level set method for geometric deformable models," *Pattern Analysis and Machine Intelligence, IEEE Transactions on*, vol. 25, no. 6, pp. 755–768, 2003.

[117] F. Ségonne, "Active contours under topology controlgenus preserving level sets," *International Journal of Computer Vision*, vol. 79, no. 2, pp. 107–117, 2008.

[118] F. Ségonne, J.-P. Pons, E. Grimson, and B. Fischl, "Active contours under topology control genus preserving level sets," in *International Workshop on Computer Vision for Biomedical Image Applications.* Springer, 2005, pp. 135–145.

[119] Y. Shi and W. C. Karl, "Differentiable minimin shape distance for incorporating topological priors in biomedical imaging," in *Biomedical Imaging: Nano to Macro, 2004. IEEE International Symposium on.* IEEE, 2004, pp. 1247–1250.

[120] O. Alexandrov and F. Santosa, "A topology-preserving level set method for shape optimization," *Journal of Computational Physics*, vol. 204, no. 1, pp. 121–130, 2005.

[121] G. Sundaramoorthi and A. Yezzi, "Global regularizing flows with topology preservation for active contours and polygons," *IEEE Transactions on Image Processing*, vol. 16, no. 3, pp. 803–812, 2007.

[122] M. E. Leventon, W. E. L. Grimson, and O. Faugeras, "Statistical shape influence in geodesic active contours," in *Computer Vision and Pattern Recognition, 2000. Proceedings. IEEE Conference on*, vol. 1. IEEE, 2000, pp. 316–323.

[123] D. Cremers, M. Rousson, and R. Deriche, "A review of statistical approaches to level set segmentation: integrating color, texture, motion and shape," *International journal of computer vision*, vol. 72, no. 2, pp. 195–215, 2007.

[124] Y. Chen, H. D. Tagare, S. Thiruvenkadam, F. Huang, D. Wilson, K. S. Gopinath, R. W. Briggs, and E. A. Geiser, "Using prior shapes in geometric active contours in a variational framework," *International Journal of Computer Vision*, vol. 50, no. 3, pp. 315–328, 2002.

[125] Y. Chen, S. Thiruvenkadam, H. D. Tagare, F. Huang, D. Wilson, and E. A. Geiser, "On the incorporation of shape priors into geometric active contours," in *Variational and Level Set Methods in Computer Vision, 2001. Proceedings. IEEE Workshop on.* IEEE, 2001, pp. 145–152.

[126] M. Rousson and N. Paragios, "Shape priors for level set representations," in *European Conference on Computer Vision.* Springer, 2002, pp. 78–92.

[127] M. Rousson, N. Paragios, and R. Deriche, "Implicit active shape models for 3D segmentation in MR imaging," in *International Conference on Medical Image Computing and Computer-Assisted Intervention.* Springer, 2004, pp. 209–216.

[128] A. Tsai, A. Yezzi, W. Wells, C. Tempany, D. Tucker, A. Fan, W. E. Grimson, and A. Willsky, "A shape-based approach to the segmentation of medical imagery using level sets," *IEEE transactions on medical imaging*, vol. 22, no. 2, pp. 137–154, 2003.

[129] ——, "Model-based curve evolution technique for image segmentation," in *Computer Vision and Pattern Recognition, 2001. CVPR 2001. Proceedings of the 2001 IEEE Computer Society Conference on*, vol. 1. IEEE, 2001, pp. I–463.

[130] D. Cremers, S. J. Osher, and S. Soatto, "Kernel density estimation and intrinsic alignment for shape priors in level set segmentation," *International Journal of Computer Vision*, vol. 69, no. 3, pp. 335–351, 2006.

[131] ——, "Kernel density estimation and intrinsic alignment for knowledge-driven segmentation: Teaching level sets to walk," in *Joint Pattern Recognition Symposium*. Springer, 2004, pp. 36–44.

[132] M. Rousson and D. Cremers, "Efficient kernel density estimation of shape and intensity priors for level set segmentation," in *International Conference on Medical Image Computing and Computer-Assisted Intervention*. Springer, 2005, pp. 757–764.

[133] D. Cremers and G. Funka-Lea, "Dynamical statistical shape priors for level set based sequence segmentation," in *Variational, Geometric, and Level Set Methods in Computer Vision*. Springer, 2005, pp. 210–221.

[134] T. Kohlberger, D. Cremers, M. Rousson, R. Ramaraj, and G. Funka-Lea, "4D shape priors for a level set segmentation of the left myocardium in SPECT sequences," in *International Conference on Medical Image Computing and Computer-Assisted Intervention*. Springer, 2006, pp. 92–100.

[135] D. Peng, B. Merriman, S. Osher, H. Zhao, and M. Kang, "A PDE-based fast local level set method," *Journal of computational physics*, vol. 155, no. 2, pp. 410–438, 1999.

[136] J. A. Sethian, *Level set methods and fast marching methods: evolving interfaces in computational geometry, fluid mechanics, computer vision, and materials science*. Cambridge university press, 1999, vol. 3.

[137] J. Weickert and G. Kühne, "Fast methods for implicit active contour models," in *Geometric level set methods in imaging, vision, and graphics*. Springer, 2003, pp. 43–57.

[138] A. Kenigsberg and .), *A Multigrid Approach for Fast Geodesic Active Contour*. Citeseer, 2002.

[139] G. Papandreou and P. Maragos, "Multigrid geometric active contour models," *IEEE transactions on image processing*, vol. 16, no. 1, pp. 229–240, 2007.

[140] Y. Shi and W. C. Karl, "A fast level set method without solving PDEs." in *ICASSP (2)*, 2005, pp. 97–100.

[141] K. Krissian and C.-F. Westin, "Fast sub-voxel re-initialization of the distance map for level set methods," *Pattern Recognition Letters*, vol. 26, no. 10, pp. 1532–1542, 2005.

[142] C. Li, C. Xu, C. Gui, and M. D. Fox, "Distance regularized level set evolution and its application to image segmentation," *IEEE transactions on image processing*, vol. 19, no. 12, pp. 3243–3254, 2010.

[143] ——, "Level set evolution without re-initialization: A new variational formulation," in *2005 IEEE Computer Society Conference on Computer Vision and Pattern Recognition (CVPR'05)*, vol. 1. IEEE, 2005, pp. 430–436.

[144] V. Estellers, D. Zosso, R. Lai, S. Osher, J.-P. Thiran, and X. Bresson, "Efficient algorithm for level set method preserving distance function," *IEEE Transactions on Image Processing*, vol. 21, no. 12, pp. 4722–4734, 2012.

[145] N. Paragios and R. Deriche, "Coupled geodesic active regions for image segmentation: A level set approach," in *Computer VisionECCV 2000*. Springer, 2000, pp. 224–240.

[146] C. Samson, L. Blanc-Féraud, G. Aubert, and J. Zerubia, "A level set model for image classification," *International Journal of Computer Vision*, vol. 40, no. 3, pp. 187–197, 2000.

[147] A. Yezzi, A. Tsai, and A. Willsky, "Medical image segmentation via coupled curve evolution equations with global constraints," in *Mathematical Methods in Biomedical Image Analysis, 2000. Proceedings. IEEE Workshop on.* IEEE, 2000, pp. 12–19.

[148] H.-K. Zhao, T. Chan, B. Merriman, and S. Osher, "A variational level set approach to multiphase motion," *Journal of computational physics*, vol. 127, no. 1, pp. 179–195, 1996.

[149] A. Tsai, W. Wells, C. Tempany, E. Grimson, and A. Willsky, "Mutual information in coupled multi-shape model for medical image segmentation," *Medical Image Analysis*, vol. 8, no. 4, pp. 429–445, 2004.

[150] L. A. Vese and T. F. Chan, "A multiphase level set framework for image segmentation using the mumford and shah model," *International journal of computer vision*, vol. 50, no. 3, pp. 271–293, 2002.

[151] A.-R. Mansouri, A. Mitiche, and C. Vázquez, "Multiregion competition: A level set extension of region competition to multiple region image partitioning," *Computer Vision and Image Understanding*, vol. 101, no. 3, pp. 137–150, 2006.

[152] T. Brox and J. Weickert, "Level set segmentation with multiple regions," *Image Processing, IEEE Transactions on*, vol. 15, no. 10, pp. 3213–3218, 2006.

[153] E. D. Angelini, T. Song, B. D. Mensh, and A. Laine, "Multi-phase three-dimensional level set segmentation of brain MRI," in *Medical Image Computing and Computer-Assisted Intervention–MICCAI 2004*. Springer, 2004, pp. 318–326.

[154] L. Bertelli, B. Sumengen, B. Manjunath, and F. Gibou, "A variational framework for multiregion pairwise-similarity-based image segmentation," *IEEE Transactions on Pattern Analysis and Machine Intelligence*, vol. 30, no. 8, pp. 1400–1414, 2008.

[155] B. Sumengen and B. Manjunath, "Graph partitioning active contours (GPAC) for image segmentation," *IEEE Transactions on Pattern Analysis and Machine Intelligence*, vol. 28, no. 4, pp. 509–521, 2006.

[156] M. Cabezas, A. Oliver, X. Lladó, J. Freixenet, and M. B. Cuadra, "A review of atlas-based segmentation for magnetic resonance brain images," *Computer methods and programs in biomedicine*, vol. 104, no. 3, pp. e158–e177, 2011.

[157] R. Bajcsy, R. Lieberson, and M. Reivich, "A computerized system for the elastic matching of deformed radiographic images to idealized atlas images." *Journal of computer assisted tomography*, vol. 7, no. 4, pp. 618–625, 1983.

[158] J. C. Gee, M. Reivich, and R. Bajcsy, "Elastically deforming 3D atlas to match anatomical brain images." *Journal of computer assisted tomography*, vol. 17, no. 2, pp. 225–236, 1993.

[159] D. L. Collins, C. J. Holmes, T. M. Peters, and A. C. Evans, "Automatic 3-D model-based neuroanatomical segmentation," *Human brain mapping*, vol. 3, no. 3, pp. 190–208, 1995.

[160] D. V. Iosifescu, M. E. Shenton, S. K. Warfield, R. Kikinis, J. Dengler, F. A. Jolesz, and R. W. McCarley, "An automated registration algorithm for measuring MRI subcortical brain structures," *Neuroimage*, vol. 6, no. 1, pp. 13–25, 1997.

[161] B. M. Dawant, S. L. Hartmann, J.-P. Thirion, F. Maes, D. Vandermeulen, and P. Demaerel, "Automatic 3-D segmentation of internal structures of

the head in MR images using a combination of similarity and free-form transformations. i. methodology and validation on normal subjects," *IEEE transactions on medical imaging*, vol. 18, no. 10, pp. 909–916, 1999.

[162] C. Baillard, P. Hellier, and C. Barillot, "Segmentation of brain 3D MR images using level sets and dense registration," *Medical image analysis*, vol. 5, no. 3, pp. 185–194, 2001.

[163] Y. Wu, S. K. Warfield, I. L. Tan, W. M. Wells, D. S. Meier, R. A. van Schijndel, F. Barkhof, and C. R. Guttmann, "Automated segmentation of multiple sclerosis lesion subtypes with multichannel MRI," *NeuroImage*, vol. 32, no. 3, pp. 1205–1215, 2006.

[164] C. Ciofolo and C. Barillot, "Atlas-based segmentation of 3D cerebral structures with competitive level sets and fuzzy control," *Medical image analysis*, vol. 13, no. 3, pp. 456–470, 2009.

[165] A. Klein and J. Hirsch, "Mindboggle: A scatterbrained approach to automate brain labeling," *NeuroImage*, vol. 24, no. 2, pp. 261–280, 2005.

[166] P. Hellier and C. Barillot, "A hierarchical parametric algorithm for deformable multimodal image registration," *Computer Methods and Programs in Biomedicine*, vol. 75, no. 2, pp. 107–115, 2004.

[167] A. Andronache, M. von Siebenthal, G. Székely, and P. Cattin, "Non-rigid registration of multi-modal images using both mutual information and cross-correlation," *Medical image analysis*, vol. 12, no. 1, pp. 3–15, 2008.

[168] X. Han, M. S. Hoogeman, P. C. Levendag, L. S. Hibbard, D. N. Teguh, P. Voet, A. C. Cowen, and T. K. Wolf, "Atlas-based auto-segmentation of head and neck CT images," in *Medical Image Computing and Computer-Assisted Intervention–MICCAI 2008*. Springer, 2008, pp. 434–441.

[169] Y. Luo, "Efficient magnetic resonance brain image registration and high performance registration-based brain image segmentation," Ph.D. dissertation, 2012.

[170] P.-L. Bazin and D. L. Pham, "Homeomorphic brain image segmentation with topological and statistical atlases," *Medical image analysis*, vol. 12, no. 5, pp. 616–625, 2008.

[171] X. Han and B. Fischl, "Atlas renormalization for improved brain MR image segmentation across scanner platforms," *Medical Imaging, IEEE Transactions on*, vol. 26, no. 4, pp. 479–486, 2007.

[172] K. Van Leemput, F. Maes, D. Vandermeulen, and P. Suetens, "Automated model-based tissue classification of MR images of the brain," *IEEE transactions on medical imaging*, vol. 18, no. 10, pp. 897–908, 1999.

[173] K. Van Leemput, F. Maes, D. Vandermeulen, A. Colchester, and P. Suetens, "Automated segmentation of multiple sclerosis lesions by model outlier detection," *IEEE transactions on medical imaging*, vol. 20, no. 8, pp. 677–688, 2001.

[174] B. Fischl, D. H. Salat, E. Busa, M. Albert, M. Dieterich, C. Haselgrove, A. Van Der Kouwe, R. Killiany, D. Kennedy, S. Klaveness *et al.*, "Whole brain segmentation: automated labeling of neuroanatomical structures in the human brain," *Neuron*, vol. 33, no. 3, pp. 341–355, 2002.

[175] S. P. Awate, T. Tasdizen, N. Foster, and R. T. Whitaker, "Adaptive markov modeling for mutual-information-based, unsupervised MRI brain-tissue classification," *Medical Image Analysis*, vol. 10, no. 5, pp. 726–739, 2006.

[176] F. van der Lijn, T. den Heijer, M. M. Breteler, and W. J. Niessen, "Hippocampus segmentation in MR images using atlas registration, voxel classification, and graph cuts," *Neuroimage*, vol. 43, no. 4, pp. 708–720, 2008.

[177] S. Bricq, C. Collet, and J.-P. Armspach, "Unifying framework for multimodal brain MRI segmentation based on hidden markov chains," *Medical image analysis*, vol. 12, no. 6, pp. 639–652, 2008.

[178] J.-C. Souplet, C. Lebrun, N. Ayache, G. Malandain *et al.*, "An automatic segmentation of t2-flair multiple sclerosis lesions," in *The MIDAS Journal-MS Lesion Segmentation (MICCAI 2008 Workshop)*. Citeseer, 2008.

[179] N. Shiee, P. Bazin, and D. L. Pham, "Multiple sclerosis lesion segmentation using statistical and topological atlases," *Grand Challenge Work.: Mult. Scler. Lesion Segm. Challenge*, pp. 1–10, 2008.

[180] D.-J. Kroon, E. Oort, and C. Slump, "Multiple sclerosis detection in multispectral magnetic resonance images with principal components analysis," 2008.

[181] A. Akselrod-Ballin, M. Galun, J. M. Gomori, M. Filippi, P. Valsasina, R. Basri, and A. Brandt, "Automatic segmentation and classification of multiple sclerosis in multichannel MRI," *IEEE transactions on biomedical engineering*, vol. 56, no. 10, pp. 2461–2469, 2009.

[182] P. Aljabar, R. A. Heckemann, A. Hammers, J. V. Hajnal, and D. Rueckert, "Multi-atlas based segmentation of brain images: atlas selection and its effect on accuracy," *Neuroimage*, vol. 46, no. 3, pp. 726–738, 2009.

[183] J. E. Iglesias and M. R. Sabuncu, "Multi-atlas segmentation of biomedical images: A survey," *Medical image analysis*, vol. 24, no. 1, pp. 205–219, 2015.

[184] X. Han, L. S. Hibbard, and V. Willcut, "GPU-accelerated, gradient-free MI deformable registration for atlas-based MR brain image segmentation," in *Computer Vision and Pattern Recognition Workshops, 2009. CVPR Workshops 2009. IEEE Computer Society Conference on.* IEEE, 2009, pp. 141–148.

[185] X. Han, L. S. Hibbard, N. P. O'Connell, and V. Willcut, "Automatic segmentation of parotids in head and neck CT images using multi-atlas fusion," *Medical Image Analysis for the Clinic: A Grand Challenge*, pp. 297–304, 2010.

[186] X. Artaechevarria, A. Munoz-Barrutia, and C. Ortiz-de Solórzano, "Combination strategies in multi-atlas image segmentation: application to brain MR data," *IEEE transactions on medical imaging*, vol. 28, no. 8, pp. 1266–1277, 2009.

[187] I. Isgum, M. Staring, A. Rutten, M. Prokop, M. A. Viergever, and B. van Ginneken, "Multi-atlas-based segmentation with local decision fusionapplication to cardiac and aortic segmentation in CT scans," *IEEE transactions on medical imaging*, vol. 28, no. 7, pp. 1000–1010, 2009.

[188] M. R. Sabuncu, B. T. Yeo, K. Van Leemput, B. Fischl, and P. Golland, "A generative model for image segmentation based on label fusion," *IEEE transactions on medical imaging*, vol. 29, no. 10, pp. 1714–1729, 2010.

[189] S. K. Warfield, K. H. Zou, and W. M. Wells, "Simultaneous truth and performance level estimation (STAPLE): an algorithm for the validation of image segmentation," *IEEE transactions on medical imaging*, vol. 23, no. 7, pp. 903–921, 2004.

[190] T. Rohlfing, D. B. Russakoff, and C. R. Maurer, "Performance-based classifier combination in atlas-based image segmentation using expectation-maximization parameter estimation," *IEEE transactions on medical imaging*, vol. 23, no. 8, pp. 983–994, 2004.

[191] S. Booth, D. Clausi *et al.*, "Image segmentation using MRI vertebral cross-sections," in *Electrical and Computer Engineering, 2001. Canadian Conference on*, vol. 2. IEEE, 2001, pp. 1303–1307.

[192] J. Carballido-Gamio, S. J. Belongie, and S. Majumdar, "Normalized cuts in 3-D for spinal MRI segmentation," *Medical Imaging, IEEE Transactions on*, vol. 23, no. 1, pp. 36–44, 2004.

[193] R. Valdes, O. Yáñez-Suarez, and V. Medina, "Trachea segmentation in CT images using active contours," in *Engineering in Medicine and Biology Society, 2000. Proceedings of the 22nd Annual International Conference of the IEEE*, vol. 4. IEEE, 2000, pp. 3184–3187.

[194] N. Archip, P.-J. Erard, M. Egmont-Petersen, J.-M. Haefliger, and J.-F. Germond, "A knowledge-based approach to automatic detection of the spinal cord in CT images," *Medical Imaging, IEEE Transactions on*, vol. 21, no. 12, pp. 1504–1516, 2002.

[195] M. Terao, S. Kobashi, Y. Hata, M. Tanaka, Y. Tokimoto, O. Ishikawa, and M. Ishikawa, "Automated extraction of the endorrhachis from MR lumbar images by fuzzy inference techniques," in *IFSA World Congress and 20th NAFIPS International Conference, 2001. Joint 9th*, vol. 3. IEEE, 2001, pp. 1620–1625.

[196] P.-Y. Baudin, N. Azzabou, P. G. Carlier, N. Paragios *et al.*, "Manifold-enhanced segmentation through random walks on linear subspace priors," in *Proceedings of the British Machine Vision Conference*, 2012.

[197] S. Essafi, G. Langs, J.-F. Deux, A. Rahmouni, G. Bassez, and N. Paragios, "Wavelet-driven knowledge-based MRI calf muscle segmentation," in *IEEE International Symposium on Biomedical Imaging,*, 2009, pp. 225–228.

[198] N. Ray, S. Mukherjee, K. K. Nakka, S. T. Acton, and S. S. Blanker, "3D-to-2D mapping for user interactive segmentation of human leg muscles from MRI data," in *Signal and Information Processing (GlobalSIP), 2014 IEEE Global Conference on.* IEEE, 2014, pp. 50–54.

[199] H. Wang, Y. Cao, and T. Syeda-Mahmood, "An experimental study on combining the auto-context model with corrective learning for canine leg muscle segmentation," in *IEEE 12th International Symposium on Biomedical Imaging*, 2015, pp. 1106–1109.

[200] B. Ibragimov, J. L. Prince, E. Z. Murano, J. Woo, M. Stone, B. Likar, F. Pernuš, and T. Vrtovec, "Segmentation of tongue muscles from super-resolution magnetic resonance images," *Medical image analysis*, vol. 20, no. 1, pp. 198–207, 2015.

[201] K. Ganesan, U. R. Acharya, K. C. Chua, L. C. Min, and K. T. Abraham, "Pectoral muscle segmentation: A review," *Computer methods and programs in biomedicine*, vol. 110, no. 1, pp. 48–57, 2013.

[202] M. Mustra and M. Grgic, "Robust automatic breast and pectoral muscle segmentation from scanned mammograms," *Signal processing*, vol. 93, no. 10, pp. 2817–2827, 2013.

[203] A. Gubern-Mérida, M. Kallenberg, R. Martí, and N. Karssemeijer, "Segmentation of the pectoral muscle in breast MRI using atlas-based approaches," in *MICCAI*. Springer, 2012, pp. 371–378.

[204] S. M. Kwok, R. Chandrasekhar, Y. Attikiouzel, and M. T. Rickard, "Automatic pectoral muscle segmentation on mediolateral oblique view mammograms," *IEEE Transactions on Medical Imaging*, vol. 23, no. 9, pp. 1129–1140, 2004.

[205] V. Jurcak, J. Fripp, C. Engstrom, D. Walker, O. Salvado, S. Ourselin, and S. Crozier, "Automated segmentation of the quadratus lumborum muscle from magnetic resonance images using a hybrid atlas based-geodesic active contour scheme," in *Engineering in Medicine and Biology Society, 2008. EMBS 2008. 30th Annual International Conference of the IEEE*. IEEE, 2008, pp. 867–870.

[206] D. Zikic, B. Glocker, and A. Criminisi, "Encoding atlases by randomized classification forests for efficient multi-atlas label propagation," *Medical image analysis*, vol. 18, no. 8, pp. 1262–1273, 2014.

[207] M. N. Aktar, M. Jahangir Alam, M. Pickering, A. Webb, and D. Perriman, "Non-rigid registration of cervical spine MRI volumes," in *Engineering in Medicine and Biology Society (EMBC), 2015 37th Annual International Conference of the IEEE*. IEEE, 2015, pp. 1997–2000.

[208] M. N. Aktar, M. J. Alam, and M. Pickering, "A non-rigid 3D multi-modal registration algorithm using partial volume interpolation and the sum of conditional variance," in *International Conference on Digital lmage Computing: Techniques and Applications*, 2014, pp. 1–7.

[209] M. N. Aktar, M. J. Alain, and M. Pickering, "Robust rigid registration of CT to MRI brain volumes using the SCV similarity measure," in *Visual Communications and Image Processing Conference, 2014 IEEE*. IEEE, 2014, pp. 153–156.

[210] M. R. Pickering, "A new similarity measure for multi-modal image registration," in *2011 18th IEEE International Conference on Image Processing (ICIP)*. IEEE, 2011, pp. 2273–2276.

[211] M. R. Pickering, A. A. Muhit, J. M. Scarvell, and P. N. Smith, "A new multi-modal similarity measure for fast gradient-based 2D-3D image registration," in *Engineering in Medicine and Biology Society, 2009. EMBC 2009. Annual International Conference of the IEEE*. IEEE, 2009, pp. 5821–5824.

[212] O. Commowick, V. Arsigny, A. Isambert, J. Costa, F. Dhermain, F. Bidault, P.-Y. Bondiau, N. Ayache, and G. Malandain, "An efficient locally affine framework for the smooth registration of anatomical structures," *Medical Image Analysis*, vol. 12, no. 4, pp. 427–441, 2008.

[213] X. Zhuang, K. S. Rhode, R. S. Razavi, D. J. Hawkes, and S. Ourselin, "A registration-based propagation framework for automatic whole heart segmentation of cardiac MRI," *Medical Imaging, IEEE Transactions on*, vol. 29, no. 9, pp. 1612–1625, 2010.

[214] A. A. Muhit, M. R. Pickering, M. R. Frater, and J. F. Arnold, "Video coding using elastic motion model and larger blocks," *IEEE Transactions on Circuits and Systems for Video Technology*, vol. 20, no. 5, pp. 661–672, 2010.

[215] J. Kybic and M. Unser, "Fast parametric elastic image registration," *Image Processing, IEEE Transactions on*, vol. 12, no. 11, pp. 1427–1442, 2003.

[216] S. Baker and I. Matthews, "Lucas-kanade 20 years on: A unifying framework," *International journal of computer vision*, vol. 56, no. 3, pp. 221–255, 2004.

[217] K. M. Pohl, R. Kikinis, and W. M. Wells, "Active mean fields: Solving the mean field approximation in the level set framework," in *Information Processing in Medical Imaging*. Springer, 2007, pp. 26–37.

[218] R. Malladi and J. A. Sethian, "A unified approach to noise removal, image enhancement, and shape recovery," *Image Processing, IEEE Transactions on*, vol. 5, no. 11, pp. 1554–1568, 1996.

[219] B. Zhang, C. Zimmer, and J.-C. Olivo-Marin, "Tracking fluorescent cells with coupled geometric active contours," in *Biomedical Imaging: Nano to Macro, 2004. IEEE International Symposium on*. IEEE, 2004, pp. 476–479.

[220] T. B. Sebastian, H. Tek, J. J. Crisco, and B. B. Kimia, "Segmentation of carpal bones from CT images using skeletally coupled deformable models," *Medical Image Analysis*, vol. 7, no. 1, pp. 21–45, 2003.

[221] A. Yezzi, A. Tsai, and A. Willsky, "A fully global approach to image segmentation via coupled curve evolution equations," *Journal of Visual Communication and Image Representation*, vol. 13, no. 1, pp. 195–216, 2002.

[222] D. Adalsteinsson and J. A. Sethian, "A fast level set method for propagating interfaces," *Journal of computational physics*, vol. 118, no. 2, pp. 269–277, 1995.

[223] J. A. Sethian, *Level set methods and fast marching methods: evolving interfaces in computational geometry, fluid mechanics, computer vision, and materials science*. Cambridge university press, 1999, vol. 3.

[224] J. Weickert and G. Kühne, *Fast methods for implicit active contour models*. Springer, 2003.

[225] C. Zimmer and J.-C. Olivo-Marin, "Coupled parametric active contours," *Pattern Analysis and Machine Intelligence, IEEE Transactions on*, vol. 27, no. 11, pp. 1838–1842, 2005.

[226] S. Lobregt and M. Viergever, "A discrete dynamic contour model," *IEEE Transactions on Medical Imaging*, vol. 14, no. 1, pp. 12–24, 1995.

[227] L.-W. Chang, H.-W. Chen, and J.-R. Ho, "Reconstruction of 3D medical images: A nonlinear interpolation technique for reconstruction of 3D medical images," *CVGIP: Graphical Models and Image Processing*, vol. 53, no. 4, pp. 382–391, 1991.

[228] W.-C. Lin, S.-Y. Chen, and C.-T. Chen, "A new surface interpolation technique for reconstructing 3D objects from serial cross-sections," *Computer Vision, Graphics, and Image Processing*, vol. 48, no. 1, pp. 124–143, 1989.